

The Vortex Lattice Panel Method for Three-dimensional, Multi- body, Unsteady Flow Problems

Paul Nathan

May 2011

FRC/TG/11.04

Fluids Research Centre
Faculty of Engineering and Physical Sciences
The University of Surrey
Guildford
Surrey, GU2 7XH
United Kingdom

Abstract

This report follows on from Nathan (2011) where a two-dimensional (2D) potential flow solver based on linearly varying vortex strength panels was derived from first principles, implemented in code and successfully validated. Here a three-dimensional (3D) potential flow solver is developed for multi-body (lifting and non-lifting), unsteady problems. The goal was to formulate the simplest and lowest order method that would be quick to implement in code and quick to execute while providing satisfactory solutions. The equations and solution procedure derived in this report were implemented in Visual Basic .NET with hardware accelerated graphics using Microsoft DirectX 9.0c allowing the user to fly around the geometry and any graphical solutions in full 3D. The code was validated using basic test cases where the analytical solution was known.

Contents

INTRODUCTION.....	3
THE BIOT-SAVART LAW FOR A VORTEX FILAMENT.....	5
NON-LIFTING BODY SOLUTION	6
LIFTING BODY SOLUTION USING THE INSTANTANEOUS KUTTA CONDITION – THE WAKE MODEL	8
UNSTEADY FORMULATION	12
MULTI-BODY, UNSTEADY FORMULATION.....	13
AN ALTERNATIVE FORMULATION	14
CALCULATION OF SURFACE FORCES.....	16
EVALUATING THE PANEL SURFACE TANGENTIAL VELOCITY	16
CONTROL-VOLUME APPROACH TO CALCULATING BODY FORCES	21
VALIDATION AND TESTING.....	24
TEST CASE 1: UNIFORM STEADY FLOW OVER A SPHERE	24
TEST CASE 2: UNIFORM STEADY FLOW OVER A FINITE WING	27
TEST CASE 3: UNIFORMLY TRANSLATING WING WITH SUPERIMPOSED OSCILLATIONS	42
<i>Heave Oscillations</i>	42
<i>Roll Oscillations</i>	44
<i>Surge Oscillations</i>	45
TEST CASE 4: SIMULATION OF A PROPELLER	47
CONCLUSION & FUTURE POSSIBILITIES	58
REFERENCES	59

Introduction

For a scalar potential field $\phi(\mathbf{r})$, the velocity vector field given by $\mathbf{U} = \nabla\phi$ automatically satisfies continuity and irrotationality when $\nabla^2\phi = 0$. This is the Laplace equation for the scalar potential. Thus all incompressible potential flows are solutions of the Laplace equation. Expressed as a boundary value problem, the solution of the Laplace equation at some point \mathbf{P} in space may be written as follows

$$\phi(\mathbf{P}) = \phi_\infty(\mathbf{P}) + \frac{1}{4\pi} \iint_{A_{body}} \left[\sigma\left(\frac{1}{r}\right) - \mu \hat{\mathbf{n}} \cdot \nabla\left(\frac{1}{r}\right) \right] dA + \frac{1}{4\pi} \iint_{A_{wake}} -\mu \hat{\mathbf{n}} \cdot \nabla\left(\frac{1}{r}\right) dA$$

The solution comprises a freestream potential, a surface distribution of sources and doublets over the body as well as a surface distribution of doublets over a force-free wake. Here $\hat{\mathbf{n}}$ is the local outwardly directed unit normal vector to the surface and \mathbf{r} is the vector pointing to the point \mathbf{P} from the point on the surface at which the source or doublet element is located (with its magnitude represented by the scalar r). Now, suppose for the sake of reduction of computational workload that a solution is sought where $\sigma = 0$ everywhere. It remains to find the unique distribution of doublets that provide the physically correct solution, which is taken to be the one where the boundaries are impenetrable surfaces with fluid flowing tangentially over them. For further simplification, suppose that the surface is represented by a set of piecewise-continuous flat facets and that the distribution of the doublet strength over a surface is constant for that particular surface. The above equation simplifies to

$$\begin{aligned} \phi(\mathbf{P}) &= \phi_\infty(\mathbf{P}) - \sum_i \frac{\mu_i}{4\pi} \iint_{A_i} \hat{\mathbf{n}}_i \cdot \nabla\left(\frac{1}{r_i}\right) dA_i \\ &= \phi_\infty(\mathbf{P}) + \sum_i \frac{\mu_i}{4\pi} \iint_{A_i} \frac{1}{r_i^3} (\hat{\mathbf{n}}_i \cdot \mathbf{r}_i) dA_i \end{aligned}$$

The boundary condition of zero normal flux (Neumann boundary condition, $\mathbf{U} \cdot \hat{\mathbf{n}} = 0$ at the surface) is used to formulate a set of equations that can be solved for the doublet strengths of each surface panel. Once the doublet strengths are known, the velocity field at any point can be evaluated as desired. The boundary condition at the surface of panel i (taken at a representative point known as the ‘control point’) is given by

$$\hat{\mathbf{n}}_i \cdot \nabla\phi_{\infty i} + \sum_i \frac{\mu_i}{4\pi} \iint_{A_i} \hat{\mathbf{n}}_i \cdot \nabla\left(\frac{1}{r_i^3} (\hat{\mathbf{n}}_i \cdot \mathbf{r}_i)\right) dA_i = 0$$

$$\hat{\mathbf{n}}_i \cdot \mathbf{U}_{\infty i} + \sum_i \frac{\mu_i}{4\pi} \iint_{A_i} \frac{1}{r_i^3} \left(1 - 3(\hat{\mathbf{n}}_i \cdot \hat{\mathbf{r}}_i)^2\right) dA_i = 0$$

Note that for a lifting body additional equations are required to satisfy the Kutta condition at the trailing edge. The nature of the integral depends on the panel shape and orientation in space and the general result expressed in global coordinates is somewhat cumbersome. This is where the final simplification is carried out. It can be shown (Katz & Plotkin (2001) §10.4) that a constant strength doublet panel is equivalent to a vortex filament loop with circulation equal to the negated strength of the doublet panel (where the vortex filament loop is wound clockwise looking into the outward normal vector, and the right hand rule is used for the circulation strength). Using vortex filament loops also permits panels to have twist,

although for a quadrilateral panel this introduces ambiguity into how to define the normal vector. For this reason triangular panels are chosen for the body since the triangle is the minimal planar polygon. The velocity induced by a polygonal vortex filament loop is obtained from multiple applications of the Biot-Savart law, whose evaluation is far simpler than that of the equivalent doublet panel and also computationally quicker in that there are no logarithm or inverse tangent function calls.

The Biot-Savart Law for a Vortex Filament

Using the analogy between electromagnetism and potential flow, the Biot-Savart law is used to model the velocity \mathbf{U}_{vf} induced by a vortex filament at some point \mathbf{P} in space. Since vortex filaments cannot start or end in the fluid (Helmholtz's second law) they must appear as closed loops. This is achieved by creating vortex ring panels out of the discretised geometry. The Biot-Savart law is

$$\mathbf{U}_{vf} = \frac{\Gamma}{4\pi} \int \frac{d\mathbf{l} \times \hat{\mathbf{r}}}{r^2} \quad (1)$$

where \mathbf{r} is the vector pointing from the filament element to \mathbf{P} . Applying the above to the special case of a straight infinitesimal segment gives

$$\mathbf{U}_{vf} = \frac{\Gamma}{4\pi d} (\cos \theta_a - \cos \theta_b) \hat{\mathbf{d}} \quad (2)$$

where d is the perpendicular distance to the segment from \mathbf{P} , the angles are those between the ends of the segment and the lines going to \mathbf{P} from the ends of the segments and $\hat{\mathbf{d}}$ is the direction of the induced velocity velocity. The filament strength is assigned according to the right hand rule

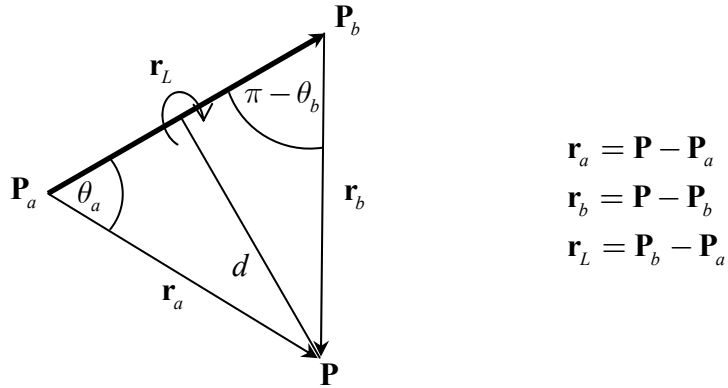


Figure 1: Nomenclature for the Biot-Savart law applied to a single finite vortex filament

The following relationships are extracted from the geometry

$$\begin{aligned} \cos \theta_a &= \frac{\mathbf{r}_L \cdot \mathbf{r}_a}{r_L r_a} \\ \cos \theta_b &= \frac{\mathbf{r}_L \cdot \mathbf{r}_b}{r_L r_b} \\ d &= \frac{\|\mathbf{r}_a \times \mathbf{r}_b\|}{r_L} \\ \hat{\mathbf{d}} &= \frac{\mathbf{r}_a \times \mathbf{r}_b}{\|\mathbf{r}_a \times \mathbf{r}_b\|} \end{aligned} \quad (3)$$

Substituting these back into (2) gives the Biot-Savart law for a straight line filament

$$\mathbf{U}_{vf} = \frac{\Gamma}{4\pi} \mathbf{r}_L \cdot (\hat{\mathbf{r}}_a - \hat{\mathbf{r}}_b) \frac{\mathbf{r}_a \times \mathbf{r}_b}{\|\mathbf{r}_a \times \mathbf{r}_b\|^2} \quad (4)$$

Non-lifting Body Solution

Consider a non-lifting body constructed out of triangular facets. The triangle edges make up the vortex filaments, with each triangle consisting of its own closed loop of filaments. Although it is possible to increase computational efficiency by dealing with overlapping edges, in the interests of simplicity this is not done here. All that needs to be done is to satisfy the zero normal flux boundary condition at the control point \mathbf{P}_c of every triangular element.

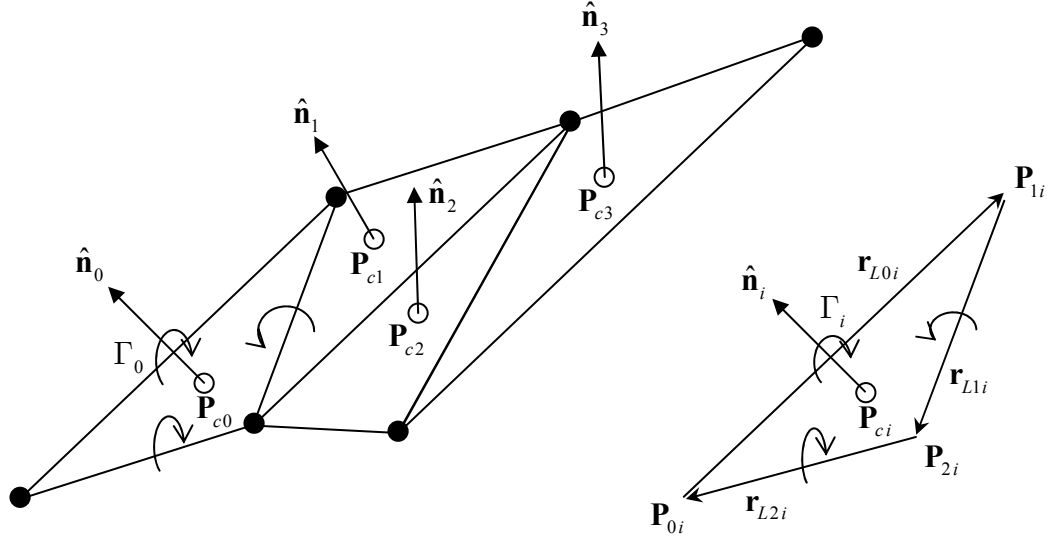


Figure 2: Illustration and nomenclature of multiple connected triangular body panels

The triangles must be wound in a clockwise positive manner when observed from “above” (i.e. looking onto the outer surface, or looking into the outward normal vector). The control point (taken to be at the centroid of the triangle), normal vector and area are obtained as follows

$$\begin{aligned}\mathbf{P}_{ci} &= \frac{1}{3}(\mathbf{P}_{0i} + \mathbf{P}_{1i} + \mathbf{P}_{2i}) \\ \hat{\mathbf{n}}_i &= \frac{(\mathbf{P}_{2i} - \mathbf{P}_{1i}) \times (\mathbf{P}_{0i} - \mathbf{P}_{2i})}{\|(\mathbf{P}_{2i} - \mathbf{P}_{1i}) \times (\mathbf{P}_{0i} - \mathbf{P}_{2i})\|} \\ A_i &= \frac{1}{2} \|(\mathbf{P}_{2i} - \mathbf{P}_{1i}) \times (\mathbf{P}_{0i} - \mathbf{P}_{2i})\|\end{aligned}\quad (5)$$

The Neumann boundary condition for triangle i is given by

$$\left(\mathbf{U}_\infty + \sum_{j=0}^{m-1} \mathbf{U}_{vloop i,j} \right) \cdot \hat{\mathbf{n}}_i = V_{ni} \quad (6)$$

where V_n represents any blowing normal to the surface at the control point and the velocity induced by the triangle vortex filament loop j on panel i $\mathbf{U}_{vloop i,j}$ is given by

$$\mathbf{U}_{vloop\,i,j} = \frac{\Gamma_j}{4\pi} \mathbf{F}_{i,j}$$

$$\begin{aligned} \mathbf{F}_{i,j} = & \mathbf{r}_{L0j} \cdot \left(\frac{(\mathbf{P}_{ci} - \mathbf{P}_{0j})}{\|\mathbf{P}_{ci} - \mathbf{P}_{0j}\|} - \frac{(\mathbf{P}_{ci} - \mathbf{P}_{1j})}{\|\mathbf{P}_{ci} - \mathbf{P}_{1j}\|} \right) \frac{(\mathbf{P}_{ci} - \mathbf{P}_{0j}) \times (\mathbf{P}_{ci} - \mathbf{P}_{1j})}{\|(\mathbf{P}_{ci} - \mathbf{P}_{0j}) \times (\mathbf{P}_{ci} - \mathbf{P}_{1j})\|^2} \\ & + \mathbf{r}_{L1j} \cdot \left(\frac{(\mathbf{P}_{ci} - \mathbf{P}_{1j})}{\|\mathbf{P}_{ci} - \mathbf{P}_{1j}\|} - \frac{(\mathbf{P}_{ci} - \mathbf{P}_{2j})}{\|\mathbf{P}_{ci} - \mathbf{P}_{2j}\|} \right) \frac{(\mathbf{P}_{ci} - \mathbf{P}_{1j}) \times (\mathbf{P}_{ci} - \mathbf{P}_{2j})}{\|(\mathbf{P}_{ci} - \mathbf{P}_{1j}) \times (\mathbf{P}_{ci} - \mathbf{P}_{2j})\|^2} \\ & + \mathbf{r}_{L2j} \cdot \left(\frac{(\mathbf{P}_{ci} - \mathbf{P}_{2j})}{\|\mathbf{P}_{ci} - \mathbf{P}_{2j}\|} - \frac{(\mathbf{P}_{ci} - \mathbf{P}_{0j})}{\|\mathbf{P}_{ci} - \mathbf{P}_{0j}\|} \right) \frac{(\mathbf{P}_{ci} - \mathbf{P}_{2j}) \times (\mathbf{P}_{ci} - \mathbf{P}_{0j})}{\|(\mathbf{P}_{ci} - \mathbf{P}_{2j}) \times (\mathbf{P}_{ci} - \mathbf{P}_{0j})\|^2} \end{aligned} \quad (7)$$

No special treatment is required for the case $i = j$. Equation (6) can now be written as

$$\sum_{j=0}^{m-1} \Gamma'_j \mathbf{F}_{i,j} \cdot \hat{\mathbf{n}}_i = V_{ni} - \mathbf{U}_\infty \cdot \hat{\mathbf{n}}_i \quad (8)$$

where $\Gamma'_j = \Gamma_j / 4\pi$. This is a linear system that can be written in matrix form and solved using the usual techniques.

$$\begin{bmatrix} \mathbf{F}_{0,0} \cdot \hat{\mathbf{n}}_0 & \mathbf{F}_{0,1} \cdot \hat{\mathbf{n}}_0 & \cdots & \mathbf{F}_{0,m-2} \cdot \hat{\mathbf{n}}_0 & \mathbf{F}_{0,m-1} \cdot \hat{\mathbf{n}}_0 \\ \mathbf{F}_{1,0} \cdot \hat{\mathbf{n}}_1 & \mathbf{F}_{1,1} \cdot \hat{\mathbf{n}}_1 & \cdots & \mathbf{F}_{1,m-2} \cdot \hat{\mathbf{n}}_1 & \mathbf{F}_{1,m-1} \cdot \hat{\mathbf{n}}_1 \\ \vdots & \vdots & \ddots & \vdots & \vdots \\ \mathbf{F}_{m-2,0} \cdot \hat{\mathbf{n}}_{m-2} & \mathbf{F}_{m-2,1} \cdot \hat{\mathbf{n}}_{m-2} & \cdots & \mathbf{F}_{m-2,m-2} \cdot \hat{\mathbf{n}}_{m-2} & \mathbf{F}_{m-2,m-1} \cdot \hat{\mathbf{n}}_{m-2} \\ \mathbf{F}_{m-1,0} \cdot \hat{\mathbf{n}}_{m-1} & \mathbf{F}_{m-1,1} \cdot \hat{\mathbf{n}}_{m-1} & \cdots & \mathbf{F}_{m-1,m-2} \cdot \hat{\mathbf{n}}_{m-1} & \mathbf{F}_{m-1,m-1} \cdot \hat{\mathbf{n}}_{m-1} \end{bmatrix} \begin{pmatrix} \Gamma'_0 \\ \Gamma'_1 \\ \vdots \\ \Gamma'_{m-2} \\ \Gamma'_{m-1} \end{pmatrix} = \begin{pmatrix} V_{n0} - \mathbf{U}_\infty \cdot \hat{\mathbf{n}}_0 \\ V_{n1} - \mathbf{U}_\infty \cdot \hat{\mathbf{n}}_1 \\ \vdots \\ V_{nm-2} - \mathbf{U}_\infty \cdot \hat{\mathbf{n}}_{m-2} \\ V_{nm-1} - \mathbf{U}_\infty \cdot \hat{\mathbf{n}}_{m-1} \end{pmatrix} \quad (9)$$

$$[\mathbf{A}_1]$$

$$\Gamma_{body} = \mathbf{B}$$

This matrix equation, for non-lifting bodies only, can be solved using either direct or iterative methods. For a system containing on the order of thousands of elements, it is actually faster to use iterative methods (such as Gauss-Seidel). There is an additional advantage to the iterative approach when dealing with closed bodies. A closed-body problem actually results in an indeterminate solution because the determinant of the matrix of influence coefficients turns out to be zero. This is due to the nature of the paneling such that when there are no free edges the induced velocity ultimately depends on the *difference* in the circulation strengths of the filaments making up the panels. Thus the solution is determined only to within some arbitrary constant. Another line of reasoning is that of continuity in combination with the Neumann boundary condition (Srivastava 1994). If all m panels making up a closed body have a zero normal flux boundary condition individually imposed on them then the condition on one of the panels becomes redundant. This is because if there is no normal flux on all $m-1$ panels, then by continuity there can be no flux through the final panel – the only remaining route for any flux into and out of the closed body. Thus the closed body system is over-specified. One way to resolve this issue is to assign an arbitrary strength to any one of the panels and then solve the system in the usual manner. This arbitrary value can be zero which would be analogous to actually having no panel. Thus deleting one of the equations (removing one of the panels) in the closed body will result in a unique, determinate solution. This issue is not present when solving the system using an iterative method since the influence matrix does not require inversion. After sufficient iteration, the same solution is obtained as with the direct method after removal of one panel.

Lifting Body Solution using the Instantaneous Kutta Condition – The Wake Model

For a body to generate lift in a potential flow, it must have a bound circulation. The strength of the bound circulation is fixed by enforcing the Kutta condition at the trailing edge of the lifting body. In line with the Kelvin condition, a shed wake is necessary in order to conserve net circulation for all time. In the absence of viscosity the shed wake panels do not alter in strength for all time and so can be treated as known quantities. This reduces the problem to specifying the strength of the wake panels attached to the trailing edge of the body before they are advected by the local flow field. In the 2D case the Kelvin condition was used to determine the strength of the single attached wake panel. However in 3D there are now multiple attached wake panels and so the Kelvin condition alone becomes indeterminate. In the present formulation using vortex ring panels, an attached wake panel is the only means by which the trailing edge circulation at a given station can be nullified, and so its strength is set simply according to the instantaneous Kutta condition at that location. Thus all the attached wake panels have their strength set by application of an instantaneous Kutta condition. The corner points of the wake panels are then advected by their local velocity field and the cycle continues – new wake panels are created at the trailing edge and joined up with the corner points of the previously shed wake panel from the same station. These previously shed wake panels influence the flow field and, since their strength is set for all time, their influence is taken into consideration as a summation in the right-hand-side vector of known quantities.

Rather than using triangular panels for the wake, it makes more sense (from a computational efficiency point of view) to use quadrilateral panels. The reason for this is that if triangular panels were used, only one of the triangles' edges would be shared with the body trailing edge panel, with the other triangle making up the other half of the wake panel having its strength explicitly set equal to its neighbour that is attached to the trailing edge. This results in the diagonal filament having its circulation effectively cancelled out, resulting in an equivalent quadrilateral, as illustrated below

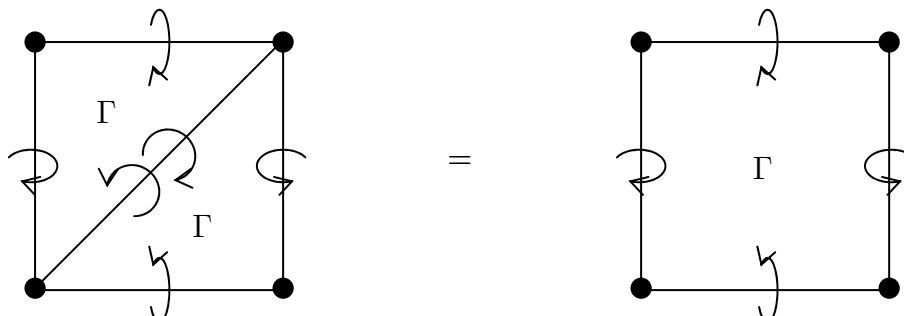


Figure 3: Equivalence of two triangular panels with identical strength to a quadrilateral panel

Suppose that there are N_{TE} shared trailing edge lines making up the trailing edge of the body, and N_w previously shed wake panels.

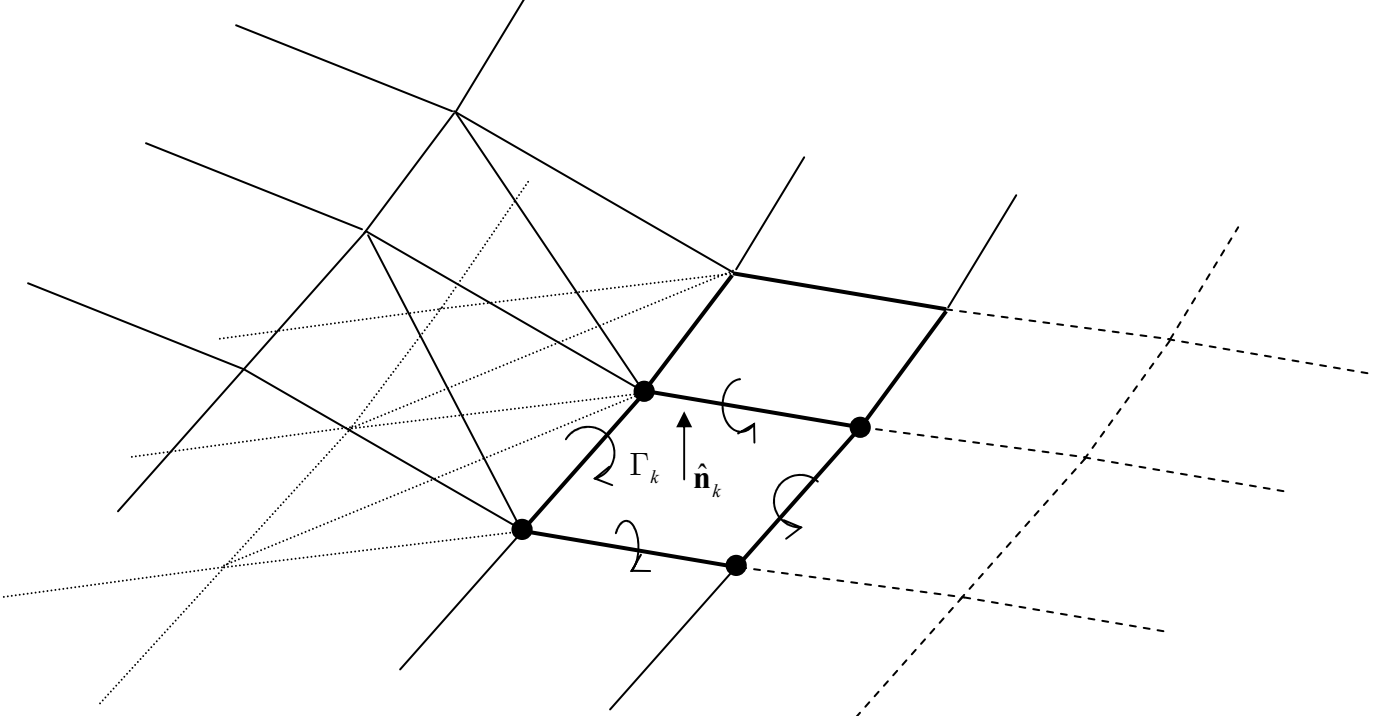


Figure 4: Illustration of attached wake panels

The above figure shows the example of two quadrilateral trailing edge panels. The bold lines indicate the new wake panel edges and the dashed lines previously shed wake panels of known strength. The circulation strength is determined using the Kutta condition, $\Gamma_{TE} = 0$. Supposing that indices p and q denote the lower and upper body panels containing the shared trailing edge line, then the strength of the k^{th} new wake panel is given by

$$\begin{aligned}\Gamma_k + \Gamma_p - \Gamma_q &= 0 \\ \therefore \Gamma_k &= -(\Gamma_p - \Gamma_q)\end{aligned}\tag{10}$$

The trailing edge panel itself is defined by the points that make up the body trailing edge and those of the previously shed wake panel associated with that particular trailing edge line. The very first set of attached wake panels may have their free end-points placed by extension of the local trailing edge bisector vector by an amount related to the body motion or freestream velocity, or simply by advecting the trailing edge points by the body motion or freestream velocity over a single time step (c.f. Nathan 2011).

During the wake panel corner point advection step, the panel edge lengths may change thereby altering the panel circulation. In order to ensure global conservation of circulation by application of an individual Kelvin condition to each wake panel it is necessary to rescale the panel circulation strength according to the ratio of current to original perimeter (not area).

$$\Gamma_k(t) = \Gamma_{k0} \frac{r_{L00k} + r_{L10k} + r_{L20k} + r_{L30k}}{r_{L0k}(t) + r_{L1k}(t) + r_{L2k}(t) + r_{L3k}(t)}\tag{11}$$

The velocity induced by the k^{th} wake panel on the i^{th} body panel control point is given by an expression similar to equation (7) but now with an extra filament

$$\mathbf{U}_{wakei,k} = \frac{\Gamma_k}{4\pi} \mathbf{H}_{i,k}$$

$$\begin{aligned}
\mathbf{H}_{i,k} = & \mathbf{r}_{L0k} \cdot \left(\frac{(\mathbf{P}_{ci} - \mathbf{P}_{0k})}{\|\mathbf{P}_{ci} - \mathbf{P}_{0k}\|} - \frac{(\mathbf{P}_{ci} - \mathbf{P}_{1k})}{\|\mathbf{P}_{ci} - \mathbf{P}_{1k}\|} \right) \frac{(\mathbf{P}_{ci} - \mathbf{P}_{0k}) \times (\mathbf{P}_{ci} - \mathbf{P}_{1k})}{\|(\mathbf{P}_{ci} - \mathbf{P}_{0k}) \times (\mathbf{P}_{ci} - \mathbf{P}_{1k})\|^2} \\
& + \mathbf{r}_{L1k} \cdot \left(\frac{(\mathbf{P}_{ci} - \mathbf{P}_{1k})}{\|\mathbf{P}_{ci} - \mathbf{P}_{1k}\|} - \frac{(\mathbf{P}_{ci} - \mathbf{P}_{2k})}{\|\mathbf{P}_{ci} - \mathbf{P}_{2k}\|} \right) \frac{(\mathbf{P}_{ci} - \mathbf{P}_{1k}) \times (\mathbf{P}_{ci} - \mathbf{P}_{2k})}{\|(\mathbf{P}_{ci} - \mathbf{P}_{1k}) \times (\mathbf{P}_{ci} - \mathbf{P}_{2k})\|^2} \\
& + \mathbf{r}_{L2k} \cdot \left(\frac{(\mathbf{P}_{ci} - \mathbf{P}_{2k})}{\|\mathbf{P}_{ci} - \mathbf{P}_{2k}\|} - \frac{(\mathbf{P}_{ci} - \mathbf{P}_{3k})}{\|\mathbf{P}_{ci} - \mathbf{P}_{3k}\|} \right) \frac{(\mathbf{P}_{ci} - \mathbf{P}_{2k}) \times (\mathbf{P}_{ci} - \mathbf{P}_{3k})}{\|(\mathbf{P}_{ci} - \mathbf{P}_{2k}) \times (\mathbf{P}_{ci} - \mathbf{P}_{3k})\|^2} \\
& + \mathbf{r}_{L3k} \cdot \left(\frac{(\mathbf{P}_{ci} - \mathbf{P}_{3k})}{\|\mathbf{P}_{ci} - \mathbf{P}_{3k}\|} - \frac{(\mathbf{P}_{ci} - \mathbf{P}_{0k})}{\|\mathbf{P}_{ci} - \mathbf{P}_{0k}\|} \right) \frac{(\mathbf{P}_{ci} - \mathbf{P}_{3k}) \times (\mathbf{P}_{ci} - \mathbf{P}_{0k})}{\|(\mathbf{P}_{ci} - \mathbf{P}_{3k}) \times (\mathbf{P}_{ci} - \mathbf{P}_{0k})\|^2}
\end{aligned} \tag{12}$$

With the wake panels, the Neumann boundary condition for the i^{th} body panel is now

$$\left(\mathbf{U}_\infty + \sum_{j=0}^{m-1} \mathbf{U}_{vloopi,j} + \sum_{k=0}^{N_w-1} \mathbf{U}_{wakei,k} \right) \bullet \hat{\mathbf{n}}_i = V_{ni}$$

Separating the known and unknown quantities over to the left and right hand sides respectively brings the equation into a form amenable to matrix formulation

$$\begin{aligned}
& \left(\sum_{j=0}^{m-1} \mathbf{U}_{vloopi,j} + \sum_{k=N_w-N_{TE}}^{N_w-1} \mathbf{U}_{wakei,k} \right) \bullet \hat{\mathbf{n}}_i = V_{ni} - \left(\mathbf{U}_\infty + \sum_{k=0}^{N_w-N_{TE}-1} \mathbf{U}_{wakei,k} \right) \bullet \hat{\mathbf{n}}_i \\
& \sum_{j=0}^{m-1} \Gamma_{body}{}'{}_j \mathbf{F}_{i,j} \bullet \hat{\mathbf{n}}_i + \sum_{k=N_w-N_{TE}}^{N_w-1} \Gamma_{wake}{}'{}_k \mathbf{H}_{i,k} \bullet \hat{\mathbf{n}}_i = V_{ni} - \left(\mathbf{U}_\infty + \sum_{k=0}^{N_w-N_{TE}-1} \Gamma_{wake}{}'{}_k \mathbf{H}_{i,k} \right) \bullet \hat{\mathbf{n}}_i
\end{aligned} \tag{13}$$

$$[\mathbf{A}_1] \Gamma_{body}{}' + [\mathbf{A}_2] \Gamma_{wake}{}' = \mathbf{B}$$

This formulation supposes the wake panels to be stored in a 1D dynamic array, with the new attached wake panels occupying the end of the array.

The matrix of influence coefficients now ultimately comprises four block matrices

- $[\mathbf{A}_1]$ the normal velocity components (per unit circulation strength) induced by the body panels on all other body panels, including self-influence. Equation (9)
- $[\mathbf{A}_2]$ the normal velocity components (per unit circulation strength) induced by the new attached wake panels on the body panels. Equation (12)
- $[\mathbf{A}_3]$ the instantaneous Kutta condition for each new attached wake panel. Equation (10)
- $[\mathbf{A}_4]$ an identity matrix for the new attached wake panel strengths (also a result of Equation (10))

The matrix equation thus takes the following form

$$\begin{bmatrix} [\mathbf{A}_1] & [\mathbf{A}_2] \\ [\mathbf{A}_3] & [\mathbf{A}_4] \end{bmatrix} \begin{pmatrix} \boldsymbol{\Gamma}_{body} \\ \boldsymbol{\Gamma}_{wake} \end{pmatrix} = \begin{pmatrix} \mathbf{B} \\ \mathbf{0} \end{pmatrix} \quad (14)$$

The dimensions of the block matrices and column vectors are as follows:

- $[\mathbf{A}_1] \ m \times m$
- $[\mathbf{A}_2] \ m \times N_{TE}$
- $[\mathbf{A}_3] \ N_{TE} \times m$
- $[\mathbf{A}_4] \ N_{TE} \times N_{TE}$
- $\boldsymbol{\Gamma}_{body} \ m$
- $\boldsymbol{\Gamma}_{wake} \ N_{TE}$
- $\mathbf{B} \ m$
- $\mathbf{0} \ N_{TE}$

The matrix of influence coefficients is a square matrix of dimension $m + N_{TE}$. The size does not change with time as the dimension is dependent only on the panel geometry and the number of trailing edge stations. Only the summation limit on the right-hand-side changes as more wake panels are shed.

Unsteady Formulation

Owing to the instantaneous nature of potential flows, the extension to unsteady flows and body motions involves only a minor modification to the right hand side vector. The formulation of the matrix of influence coefficients remains unchanged, but may require updating at each time step depending on the nature of the problem. Taking into account linear and rotational motions, the right-hand-side vector becomes, for panel i

$$B_i = V_{ni} - \left(\mathbf{U}_\infty + \sum_{k=0}^{N_w - N_{TE} - 1} \Gamma_{wake}^k \mathbf{H}_{i,k} - \mathbf{v}_{body} - \boldsymbol{\Omega} \times \mathbf{R}_i \right) \cdot \hat{\mathbf{n}}_i \quad (15)$$

where \mathbf{v}_{body} is the body velocity vector, $\boldsymbol{\Omega}$ is the body rotation vector and \mathbf{R}_i is the vector going from the centre of rotation to the i^{th} panel control point. All of these may be functions of time.

The solution procedure can be summarised step-by-step as follows

1. Initialise geometry and create panel edge and vertex link-lists
2. Kinematics (body motions / deformations)
3. Create new attached wake panels joining body trailing edge panels to previously shed wake panels
4. Build influence matrix and right-hand-side vector
5. Solve matrix equation and assign circulation strengths to their appropriate panels
6. Perform desired force and moment calculations and output of data
7. Increment time
8. Advect the wake
9. Conserve wake circulation
10. Return to step 2 until desired time has elapsed (or any other special condition)

The unsteady formulation can also be used to solve steady lifting problems, where the time stepping can be viewed as a solution relaxation process. The most involved steps in terms of coding are 1 and 8. It is very helpful to set up an efficient organisation of body and wake panel custom data types and associated arrays from the start. The specifics are left to the reader to decide as a matter of personal preference. The link lists mentioned in step 1 are necessary when computing the surface forces and also for implementing vertex-interpolated smooth shading of the surfaces based on surface pressure.

The wake advection step 8, which is carried out due to the force-free nature of the wake sheet, is conceptually simple but rather tedious in code. Supposing a first order explicit time stepping scheme, the procedure can be expressed as follows for a corner point \mathbf{P} of one of the wake panels

$$\mathbf{P}(t + \Delta t) = \mathbf{P}(t) + \mathbf{U} \Delta t \quad (16)$$

where \mathbf{U} is the sum of the induced velocities at the point \mathbf{P} by all the body and wake panels. The additional effort comes in ensuring that the singular case of a point lying on the end of a vortex filament is not computed. Thus when a point belongs to the panel being looped through, only the two filaments that are not connected to the point must be used to evaluate the induced velocity vector (recall that a vortex ring does advect itself). Furthermore, since each interior point in the wake sheet is shared by four panels, a simple loop through all points will result in a quadruple repetition of calculations for these interior points, incurring a noticeable speed penalty (especially when the number of wake panes becomes large). The code can be optimised to loop through the internal points (i.e. say point \mathbf{P}_1 from each internal wake panel) and then loop through the outer edge panel points separately afterwards. Owing to the structured grid link topology of the wake sheet, these points can then be used to re-construct the entire wake sheet at the next time step.

Multi-body, Unsteady Formulation

The extension to multi-body problems where there may be combinations of multiple lifting and non-lifting bodies proceeds in a similar manner to the two-dimensional case (see Nathan 2011). In the most general case the variables related to the kinematics must now be specified separately for each body, and each lifting body may have a different number of trailing edge panels (and therefore attached wake panels). Once again robust data structures and management is essential. The matrix of influence coefficients is built up of block matrices representing the influence of a body on itself (diagonal elements) and on the other bodies (off-diagonal elements). Only the block matrix elements on the diagonal contain the Kutta condition rows, with the equivalent rows on the off-diagonal elements being set to zero. The solution vector comprises successive pairs of panel strengths followed by attached wake panels strengths for each body. The right-hand-side vector comprises the \mathbf{B} column vectors for each body interleaved with appropriately sized $\mathbf{0}$ column vectors. Suppose a system of b bodies, where p and q are the counter variables used to loop through the bodies. The matrix equation has the following general form.

$$\begin{pmatrix} \begin{pmatrix} [\mathbf{A}_1] & [\mathbf{A}_2] \\ [\mathbf{A}_3] & [\mathbf{A}_4] \end{pmatrix}_{0,0} & \begin{pmatrix} [\mathbf{A}_1] & [\mathbf{A}_2] \\ [\mathbf{0}] & [\mathbf{0}] \end{pmatrix}_{0,1} & \dots & \begin{pmatrix} [\mathbf{A}_1] & [\mathbf{A}_2] \\ [\mathbf{0}] & [\mathbf{0}] \end{pmatrix}_{0,b-2} & \begin{pmatrix} [\mathbf{A}_1] & [\mathbf{A}_2] \\ [\mathbf{0}] & [\mathbf{0}] \end{pmatrix}_{0,b-1} \\ \begin{pmatrix} [\mathbf{A}_1] & [\mathbf{A}_2] \\ [\mathbf{0}] & [\mathbf{0}] \end{pmatrix}_{1,0} & \begin{pmatrix} [\mathbf{A}_1] & [\mathbf{A}_2] \\ [\mathbf{A}_3] & [\mathbf{A}_4] \end{pmatrix}_{1,1} & \dots & \begin{pmatrix} [\mathbf{A}_1] & [\mathbf{A}_2] \\ [\mathbf{0}] & [\mathbf{0}] \end{pmatrix}_{1,b-2} & \begin{pmatrix} [\mathbf{A}_1] & [\mathbf{A}_2] \\ [\mathbf{0}] & [\mathbf{0}] \end{pmatrix}_{1,b-1} \\ \vdots & \vdots & \ddots & \vdots & \vdots \\ \begin{pmatrix} [\mathbf{A}_1] & [\mathbf{A}_2] \\ [\mathbf{0}] & [\mathbf{0}] \end{pmatrix}_{b-2,0} & \begin{pmatrix} [\mathbf{A}_1] & [\mathbf{A}_2] \\ [\mathbf{0}] & [\mathbf{0}] \end{pmatrix}_{b-2,1} & \dots & \begin{pmatrix} [\mathbf{A}_1] & [\mathbf{A}_2] \\ [\mathbf{A}_3] & [\mathbf{A}_4] \end{pmatrix}_{b-2,b-2} & \begin{pmatrix} [\mathbf{A}_1] & [\mathbf{A}_2] \\ [\mathbf{0}] & [\mathbf{0}] \end{pmatrix}_{b-2,b-1} \\ \begin{pmatrix} [\mathbf{A}_1] & [\mathbf{A}_2] \\ [\mathbf{0}] & [\mathbf{0}] \end{pmatrix}_{b-1,0} & \begin{pmatrix} [\mathbf{A}_1] & [\mathbf{A}_2] \\ [\mathbf{0}] & [\mathbf{0}] \end{pmatrix}_{b-1,1} & \dots & \begin{pmatrix} [\mathbf{A}_1] & [\mathbf{A}_2] \\ [\mathbf{0}] & [\mathbf{0}] \end{pmatrix}_{b-1,b-2} & \begin{pmatrix} [\mathbf{A}_1] & [\mathbf{A}_2] \\ [\mathbf{A}_3] & [\mathbf{A}_4] \end{pmatrix}_{b-1,b-1} \end{pmatrix} \begin{pmatrix} [\Gamma_{body}']_0 \\ [\Gamma_{wake}']_0 \\ \vdots \\ [\Gamma_{body}']_{b-2} \\ [\Gamma_{wake}']_{b-2} \\ \vdots \\ [\Gamma_{body}']_{b-1} \\ [\Gamma_{wake}']_{b-1} \end{pmatrix} = \begin{pmatrix} [\mathbf{B}]_0 \\ [\mathbf{0}]_0 \\ \vdots \\ [\mathbf{B}]_{b-2} \\ [\mathbf{0}]_{b-2} \\ \vdots \\ [\mathbf{B}]_{b-1} \\ [\mathbf{0}]_{b-1} \end{pmatrix} \quad (17)$$

The influence coefficient matrix consists of two levels of block matrices. Extreme care must be taken when coding the population of this matrix, and careful checks with gradually more complex cases must be made. It is necessary at this point to expound the meaning of all the subscripts put together. Consider the following part of a block matrix

$$\begin{pmatrix} [\mathbf{A}_1] & [\mathbf{A}_2] \end{pmatrix}_{p,q}$$

This represents the influence of body q on body p . When $[\mathbf{A}_1]$ is expanded out fully into its $m_p \times m_q$ rows and columns, one of its elements $A_{1,i,j}$ would represent the normal velocity component (per unit circulation strength) induced by the j^{th} panel of body q on the i^{th} panel control point of body p . Similarly, when $[\mathbf{A}_2]$ is expanded out fully into its $m_p \times N_{TEq}$ rows and columns, one of its elements $A_{2,i,k}$ would represent the normal velocity component (per unit circulation strength) induced by the j^{th} attached wake panel of body q on the i^{th} panel control point of body p .

When appending the Kutta condition and identity matrices to the block matrices on the diagonal, there should only be three non-zero values in the entire block row. Two of these values should be +1 and one of them -1. There is the +1 from the identity matrix that should correspond to the wake panel circulation strength under consideration, and the remaining +1 and -1 elements should correspond respectively to the lower and upper side trailing edge panel strengths under consideration.

The zero matrices contained within the off-diagonal block elements have the same respective dimensions as the $[\mathbf{A}_3]$ and $[\mathbf{A}_4]$ matrices in their same row. Each block matrix on the diagonal is square, but the off-diagonal block matrices not necessarily so. The dimensions of these block matrices are such that the final coefficient matrix is square. For example consider a two-body system ($b = 2$). Body 0 consists of $m_0 + N_{TE0}$ panels and body 1 consists of $m_1 + N_{TE1}$ panels (body and wake included altogether in both cases). The block matrices therefore have the following dimensions

- $(\)_{0,0} (m_0 + N_{TE0}) \times (m_0 + N_{TE0})$
- $(\)_{0,1} (m_0 + N_{TE0}) \times (m_1 + N_{TE1})$
- $(\)_{1,0} (m_1 + N_{TE1}) \times (m_0 + N_{TE0})$
- $(\)_{1,1} (m_1 + N_{TE1}) \times (m_1 + N_{TE1})$

The resulting influence coefficient matrix is therefore square with $(m_0 + m_1 + N_{TE0} + N_{TE1})$ rows and columns.

A non-lifting body does not have a wake and so the $[\mathbf{A}_2]$, $[\mathbf{A}_3]$, $[\mathbf{A}_4]$ and $[\boldsymbol{\Gamma}'_{wake}]$ matrices for a non-lifting body are all zero (this applies to both diagonal and off-diagonal block matrices representing the influence of the non-lifting body in question on the other bodies. Thus a null row exists for a non-lifting body that is omitted during solution (or simply deleted beforehand, or even not created in the first place).

A triply-nested loop is required to populate the influence coefficient matrix. It is a matter of preference as to whether to construct each block matrix separately and then block copy it into the right place in the influence coefficient matrix, or to construct the influence matrix line by line using a system of row and column shifts as a function of body number.

An Alternative Formulation

It is possible to formulate the influence coefficient matrix in a different way that may be simpler in terms of code modification when upgrading an existing single-body unsteady code. Instead of looping through the bodies, the body number can be stored as an integer tag along with each panel in its data structure and retrieved when required.

Rather than grouping the panel and wake circulation strength vectors for each body in succession in the solution vector, all the panel circulation strengths are lumped together and are then followed by all the wake panel circulation strengths. This means that rather than storing the body panels in a 1D array (indexed by body number) of 1D dynamic arrays (indexed by panel number), all the panels can be stored together in a single 1D dynamic array indexed by panel number. The associated body number can be stored as an integer tag along with each panel in its data structure during the geometry creation stage and can be retrieved as and when required. As for the wake advection, if the optimisation involving the removal of the quadruple repetition is to be employed, then it is still necessary to group the wake panels by body number since the wakes from each body are topologically disconnected entities. The resulting matrix equation actually has identical form to that of the single body formulation as given by equation (14), however in order to illustrate how it is different to the formulation given above the organisation by body index shall be maintained. This also helps to gain understanding as to how the matrix equation is built with respect to each body

$$\begin{pmatrix}
[\mathbf{A}_1]_{0,0} & [\mathbf{A}_1]_{0,1} & \cdots & [\mathbf{A}_1]_{0,b-2} & [\mathbf{A}_1]_{0,b-1} \\
[\mathbf{A}_1]_{1,0} & [\mathbf{A}_1]_{1,1} & \cdots & [\mathbf{A}_1]_{1,b-2} & [\mathbf{A}_1]_{1,b-1} \\
\vdots & \vdots & \ddots & \vdots & \vdots \\
[\mathbf{A}_1]_{b-2,0} & [\mathbf{A}_1]_{b-2,1} & \cdots & [\mathbf{A}_1]_{b-2,b-2} & [\mathbf{A}_1]_{b-2,b-1} \\
[\mathbf{A}_1]_{b-1,0} & [\mathbf{A}_1]_{b-1,1} & \cdots & [\mathbf{A}_1]_{b-1,b-2} & [\mathbf{A}_1]_{b-1,b-1}
\end{pmatrix}
\begin{pmatrix}
[\mathbf{A}_2]_{0,0} & [\mathbf{A}_2]_{0,1} & \cdots & [\mathbf{A}_2]_{0,b-2} & [\mathbf{A}_2]_{0,b-1} \\
[\mathbf{A}_2]_{1,0} & [\mathbf{A}_2]_{1,1} & \cdots & [\mathbf{A}_2]_{1,b-2} & [\mathbf{A}_2]_{1,b-1} \\
\vdots & \vdots & \ddots & \vdots & \vdots \\
[\mathbf{A}_2]_{b-2,0} & [\mathbf{A}_2]_{b-2,1} & \cdots & [\mathbf{A}_2]_{b-2,b-2} & [\mathbf{A}_2]_{b-2,b-1} \\
[\mathbf{A}_2]_{b-1,0} & [\mathbf{A}_2]_{b-1,1} & \cdots & [\mathbf{A}_2]_{b-1,b-2} & [\mathbf{A}_2]_{b-1,b-1}
\end{pmatrix}
\begin{pmatrix}
\Gamma_{body}^0 & \Gamma_{body}^1 & \cdots & \Gamma_{body}^{b-2} & \Gamma_{body}^{b-1} \\
\Gamma_{body}^1 & \Gamma_{body}^2 & \cdots & \vdots & \vdots \\
\vdots & \vdots & \ddots & \vdots & \vdots \\
\Gamma_{body}^{b-2} & \Gamma_{body}^{b-1} & \cdots & \Gamma_{wake}^{b-2} & \Gamma_{wake}^{b-1} \\
\Gamma_{body}^{b-1} & \Gamma_{wake}^0 & \cdots & 0 & 0 \\
\Gamma_{wake}^0 & \Gamma_{wake}^1 & \cdots & 0 & 0 \\
\vdots & \vdots & \ddots & \vdots & \vdots \\
\Gamma_{wake}^{b-2} & \Gamma_{wake}^{b-1} & \cdots & 0 & 0
\end{pmatrix} = \begin{pmatrix}
\mathbf{B}_0 \\
\mathbf{B}_1 \\
\vdots \\
\mathbf{B}_{b-2} \\
\mathbf{B}_{b-1} \\
0 \\
0 \\
\vdots \\
0 \\
0
\end{pmatrix} \quad (18)$$

With this formulation it is necessary to store any non-lifting body panels *after* all the lifting body panels, otherwise null rows would need to be included which would unnecessarily complicate matters. Some care must be taken to ensure that the circulation strengths obtained from the solution vector are correctly assigned to their corresponding panels. This is simplified by keeping count of how many panels are associated with each body and the order of the bodies as entered in the matrix.

Calculation of Surface Forces

The surface force is obtained from the surface pressure coefficient which is obtained from the unsteady Bernoulli equation. At the control point of panel i the pressure coefficient is

$$C_{pi} = 1 - \frac{\mathbf{U}_i \cdot \mathbf{U}_i}{U_{ref_i}^2} - \frac{2}{U_{ref_i}^2} \frac{\partial}{\partial t} (\phi_i - \phi_\infty) \quad (19)$$

Using the result from the 2D vortex panel (Nathan 2011) or alternatively the doublet panel / vortex filament loop analogy, the unsteady term can be related to the time rate of change of panel circulation

$$\frac{\partial}{\partial t} (\phi_i - \phi_\infty) = -\frac{1}{2} \frac{\partial \Gamma_i}{\partial t} \approx -\frac{1}{2} \frac{\Gamma_i(t) - \Gamma_i(t - \Delta t)}{\Delta t} \quad (20)$$

In the general case each panel may have its own reference velocity (i.e. a spinning propeller blade) that is given by

$$U_{ref_i} = \|\mathbf{U}_\infty - \mathbf{v}_{body} - \boldsymbol{\Omega} \times \mathbf{R}_i\| \quad (21)$$

Each body can have its own velocity and rotation if required.

Evaluating the Panel Surface Tangential Velocity

The velocity vector used in (19) is the sum of all the velocities induced at the panel control point by all the other body and wake panels, as well as the panel itself. What is perhaps not immediately obvious is what is involved in the calculation of the panel's self-influence. The Biot-Savart law alone is insufficient to evaluate a panel's self-influence *at its surface* since it does not include the *principal velocity*. This term, which represents the tangential velocity at the surface, naturally arises when dealing with 2D doublet panels and also with 2D vortex panels. Both a square vortex ring panel and a constant strength doublet panel will have only a normal component self-induced at their control points. In the case of constant strength doublet panels, only if a gradient of strength exists from panel to panel will there be a tangential velocity induced at the surface. Since the vortex filament loop panel is analogous to a constant strength doublet panel, the principal velocity must be included (i.e. in addition to the panel's self-influence obtained from the Biot-Savart law). Consider the case of the outer surface of a 2D doublet panel aligned in the x -direction with strength distribution $\mu(x)$. The surface potential and surface velocity (which is entirely tangential to the surface) are given by (Katz & Plotkin (2001) p. 72)

$$\begin{aligned} \phi_{sfc}^+(x) &= -\frac{\mu(x)}{2} \\ U_{t,sfc}^+(x) &= \frac{\partial \phi_{sfc}^+}{\partial x} = -\frac{1}{2} \frac{\partial \mu}{\partial x} \end{aligned}$$

The equivalent result for a 2D vortex panel with vorticity distribution $\gamma(x)$ is

$$\phi_{sfc}^+(x) = \int_0^x \frac{\gamma(x)}{2} dx = \frac{\Gamma(x)}{2}$$

$$U_{t,sfc}^+ (x) = \frac{\partial \phi_{sfc}^+}{\partial x} = \frac{\gamma(x)}{2} = \frac{1}{2} \frac{\partial \Gamma}{\partial x}$$

This reveals the relationship of equivalence between vortex and doublet distributions where, in 2D

$$\Gamma = -\mu$$

An alternative view is that due to the way in which the edges are shared in the vortex lattice, it is ultimately the *difference* in circulation between adjacent panels that governs the magnitude and direction of the induced velocities. If a given panel has shared edges with panels of different circulation, then there is effectively a gradient of circulation set up over the panel in question. Thus the individual rings comprising a vortex lattice can be considered as surface panels with a circulation *distribution*. For this reason, the gradient of circulation must be considered in the evaluation of the surface velocity. One important consequence of this is that the induced velocities calculated very close to the surface will not be physically correct and will contain wiggles (rather like those the 2D constant strength doublet panel method or lumped vortex method suffer from). Thus the surface velocity and pressure are only strictly correct at the panel control point. This only matters when computing streaklines and particle paths where some of them that are very close to the surface may wiggle in and out of the surface. This is one penalty of using a low order method. Now, extending the 2D result to 3D gives

$$\mathbf{U}_{t,sfc}^+ = \frac{1}{2} \nabla_s \Gamma \quad (22)$$

where ∇_s is the surface gradient operator and is defined as follows

$$\nabla_s = (\nabla - \mathbf{n}(\mathbf{n} \cdot \nabla)) \quad (23)$$

i.e. the standard gradient operator with the component normal to the surface subtracted off.

There are several ways in which the surface gradient can be evaluated. Katz & Plotkin (2001) suggest a straightforward finite difference stencil, with the panel control points acting as the nodes for the stencil where the circulation strengths are stored. For unstructured or unevenly spaced panel layouts a more complex stencil must be used. Another method is that found in Appendix II of Srivastava (1991) where the difference in circulation on the panel shared edges is used directly. Though elegant, this method did not give the best results. The best results were obtained through application of the gradient theorem to convert the differentiation into a contour integration around the panel¹. Consider the divergence theorem applied to the scalar Γ

$$\iiint_V \nabla \Gamma dV = \oint_A \Gamma \hat{\mathbf{n}} dA$$

In the special case of two-dimensionality the above becomes

¹ The author would like to acknowledge Paolo Lampitella (Department of Energy, Politecnico di Milano) for making the author aware of this method, and for some useful discussions on the cfd-online forums at <http://www.cfd-online.com/Forums> (last accessed 08/04/11)

$$\iint_A \nabla_s \Gamma dA = \oint_C \Gamma \hat{\mathbf{n}} ds$$

where the normal vectors now point perpendicularly to the local contour tangent vector. In the limit of infinitesimal area, the above can be written as

$$\nabla_s \Gamma = \lim_{\Delta A \rightarrow 0} \frac{1}{\Delta A} \oint_C \Gamma \hat{\mathbf{n}} ds \quad (24)$$

Thus the surface gradient of circulation can be obtained via contour integration of the circulation around the surface in question. In practice the panels do not have infinitesimal area and so this method is a first order approximation (constant gradient over the panel). Thus accuracy is improved with smaller panels, especially in areas where the spatial gradients of circulation are likely to be large (i.e. regions of high curvature like leading edges which naturally require smaller panels for geometrical accuracy anyway). There are many ways to carry out the contour integration, with the primary option being the extent of the contour around the panel. One may chose to use higher order interpolants with larger number of surrounding panels, or try to maximise the locality of the stencil. The method of choice here is to maintain locality at the expense of smoothness. Maintaining first order accuracy, the trapezium rule is used to integrate over the linear segments that make up the closed contour, as shown in the example case below

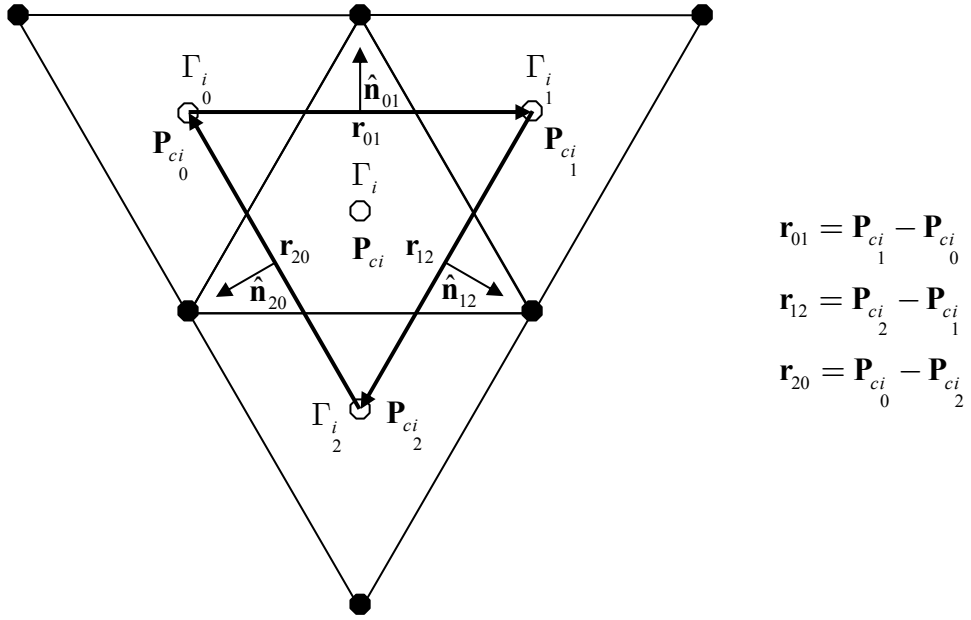


Figure 5: Contour integration path around panel i for computing the gradient of circulation

The double-subscript denotes the neighbour number of the panel that shares a common edge with the panel under consideration. This procedure requires some form of link-list associated with each triangle whereby the indices of the triangles that share its edges can be retrieved. The simplest kind of global link list would be a $M \times 3$ array of integers. The first index represents the triangle index in the array of triangles, the second index represents each of the triangles three edges. The integer value assigned to a particular set of array coordinates is the index of the triangle that shares the edge in question. The link list is created upon initialisation of the geometry. Simple proximity/overlap/intersection geometric tests can be employed to determine if an edge is shared by two triangles, and the link-list populated as appropriate.

The last problem is to obtain the contour normal vectors. There are again a variety of ways this can be done involving the normals from all the panels in the stencil (i.e. using some kind of average or weighted combination for each leg of the contour). However the method that yielded the best results was also the

one that guarantees the normal vectors to always lie parallel to the surface of the panel under consideration, thus giving the true surface gradient. For a given contour leg, the contour normal is found by taking the cross product of the contour leg direction vector and the central panel normal vector. Again, this method is most accurate where the local curvature is small, and errors can be mitigated by increasing the panel density in proportion to the local curvature. Finally, the surface gradient expression can be developed. For panel i

$$\begin{aligned}\nabla_s \Gamma_i &= \frac{1}{A_{012}} \left(\frac{1}{2} \left(\Gamma_{i_0} + \Gamma_{i_1} \right) \mathbf{r}_{01} \hat{\mathbf{n}}_{01} + \frac{1}{2} \left(\Gamma_{i_1} + \Gamma_{i_2} \right) \mathbf{r}_{12} \hat{\mathbf{n}}_{12} + \frac{1}{2} \left(\Gamma_{i_2} + \Gamma_{i_0} \right) \mathbf{r}_{20} \hat{\mathbf{n}}_{20} \right) \\ &= \frac{1}{\frac{1}{2}(\mathbf{r}_{01} \times \mathbf{r}_{20})} \left(\frac{1}{2} \left(\Gamma_{i_0} + \Gamma_{i_1} \right) \mathbf{r}_{01} (\hat{\mathbf{n}}_i \times \hat{\mathbf{r}}_{01}) + \frac{1}{2} \left(\Gamma_{i_1} + \Gamma_{i_2} \right) \mathbf{r}_{12} (\hat{\mathbf{n}}_i \times \hat{\mathbf{r}}_{12}) + \frac{1}{2} \left(\Gamma_{i_2} + \Gamma_{i_0} \right) \mathbf{r}_{20} (\hat{\mathbf{n}}_i \times \hat{\mathbf{r}}_{20}) \right) \quad (25) \\ &= \frac{\hat{\mathbf{n}}_i \times \left(\left(\Gamma_{i_0} + \Gamma_{i_1} \right) \mathbf{r}_{01} + \left(\Gamma_{i_1} + \Gamma_{i_2} \right) \mathbf{r}_{12} + \left(\Gamma_{i_2} + \Gamma_{i_0} \right) \mathbf{r}_{20} \right)}{\mathbf{r}_{01} \times \mathbf{r}_{20}\end{aligned}$$

It may be necessary to deal with the case where one of the triangle edges is an exterior edge and not shared with any other triangle. The free edge could have a “ghost” triangle attached to it with zero circulation strength and the computation carried out as normal, but this would mean additional work in defining the ghost geometry and also the location of the ghost panel free vertex is somewhat arbitrary. A better approach is to substitute the central panel for the missing panel. For example, suppose that edge 2 is free, the integration contour would appear as follows

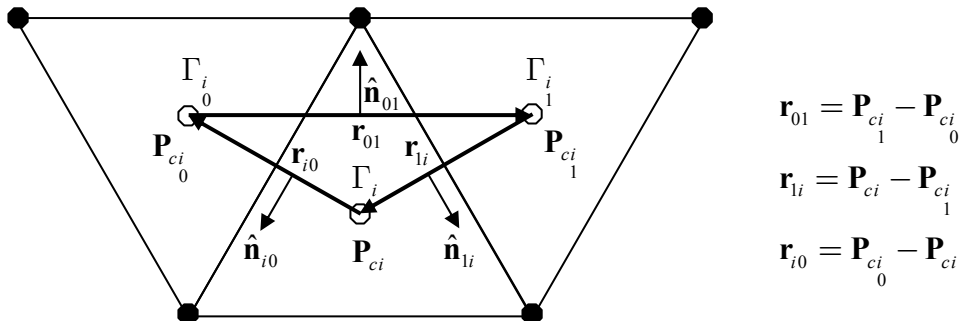


Figure 6: Contour integration path around panel i for computing the gradient of circulation in the particular case where edge 2 is free

The surface gradient of circulation for all the possible cases can now be written down

$$\nabla_s \Gamma_i = \begin{cases} \frac{\hat{\mathbf{n}}_i \times \left(\left(\Gamma_{i0} + \Gamma_{i1} \right) \mathbf{r}_{01} + \left(\Gamma_{i1} + \Gamma_{i2} \right) \mathbf{r}_{12} + \left(\Gamma_{i2} + \Gamma_{i0} \right) \mathbf{r}_{20} \right)}{\mathbf{r}_{01} \times \mathbf{r}_{20}} & \text{all edges shared} \\ \frac{\hat{\mathbf{n}}_i \times \left(\left(\Gamma_i + \Gamma_{i1} \right) \mathbf{r}_{i1} + \left(\Gamma_{i1} + \Gamma_{i2} \right) \mathbf{r}_{12} + \left(\Gamma_{i2} + \Gamma_i \right) \mathbf{r}_{2i} \right)}{\mathbf{r}_{i1} \times \mathbf{r}_{2i}} & \text{edge 0 free} \\ \frac{\hat{\mathbf{n}}_i \times \left(\left(\Gamma_{i0} + \Gamma_i \right) \mathbf{r}_{0i} + \left(\Gamma_i + \Gamma_{i2} \right) \mathbf{r}_{i2} + \left(\Gamma_{i2} + \Gamma_{i0} \right) \mathbf{r}_{20} \right)}{\mathbf{r}_{0i} \times \mathbf{r}_{20}} & \text{edge 1 free} \\ \frac{\hat{\mathbf{n}}_i \times \left(\left(\Gamma_{i0} + \Gamma_{i1} \right) \mathbf{r}_{01} + \left(\Gamma_{i1} + \Gamma_i \right) \mathbf{r}_{1i} + \left(\Gamma_i + \Gamma_{i0} \right) \mathbf{r}_{i0} \right)}{\mathbf{r}_{01} \times \mathbf{r}_{i0}} & \text{edge 2 free} \end{cases} \quad (26)$$

Such cases can be flagged by having a negative index in the link-list whenever an edge is free. A case-by-case test must be made in the loop such that all three free edge possibilities are dealt with appropriately. If two edges are unshared then the gradient term is omitted altogether.

Furthermore, the case of the trailing edge must be considered. Here the adjacent panel to the shared trailing edge is flipped over and this leads to spurious values of the circulation gradient at the trailing edge panels (usually leading to excessively negative values of C_p). Since the Kutta condition results in a stagnation point at the trailing edge, then, supposing a decent panel density at the trailing edge, the principal velocity can validly be omitted at the trailing edge panels since the tangential component of velocity is tending to zero towards the trailing edge anyway.

With the surface gradient of circulation at hand, the pressure coefficient can finally be computed. The velocity vector used in equation (19) can be written as the sum of the velocity vector induced by application of the Biot-Savart law and the surface tangential velocity as given by equations (22) and (26)

$$\begin{aligned} \mathbf{U}_i &= \mathbf{U}_{BSi} + \mathbf{U}_{t,sfc}^+ \\ &= \sum_{j=0}^{m-1} \mathbf{U}_{vloopi,j} + \sum_{k=0}^{N_w-1} \mathbf{U}_{wakei,k} + \mathbf{U}_{t,sfc}^+ \\ &= \sum_{j=0}^{m-1} \Gamma_{body}{}'{}_j \mathbf{F}_{i,j} + \sum_{k=0}^{N_w-1} \Gamma_{wake}{}'{}_k \mathbf{H}_{i,k} + \frac{1}{2} \nabla_s \Gamma_i \end{aligned} \quad (27)$$

where $\mathbf{F}_{i,j}$ and $\mathbf{H}_{i,k}$ are given in equations (7) and (12) respectively. This velocity vector is used in the surface pressure coefficient equation (19).

With the surface pressure coefficient at hand, the panel normal force can be obtained as well as the induced torque

$$\mathbf{f}_{ni} = -C_{pi} \frac{1}{2} \rho U_{refi}^2 A_i \hat{\mathbf{n}}_i$$

$$\boldsymbol{\tau}_i = \mathbf{r}_i \times \mathbf{f}_{ni}$$
(28)

where A_i is the panel area as given by equation (5) and \mathbf{r}_i is the vector pointing from the (specified) point at which the torque is being measured to the i^{th} panel control point. The resultant body force and torque is obtained by summation of each panel's contribution. Force and moment coefficients can now be calculated as desired.

Control-Volume Approach to Calculating Body Forces

The approach given thus far involves the direct evaluation of surface forces over the body. The accuracy is dependent upon the panel geometry and resolution and in some cases more robust results are possible through use of the integral form of the momentum theorem of fluid mechanics. Applied to some arbitrary fixed control volume V enclosed by surface A the force balance on the fluid in the enclosed region is given by (Kuethe & Chow (1998))

$$\frac{d}{dt} \iiint_V \rho \mathbf{U} dV + \iint_A \rho \mathbf{U} (\mathbf{U} \cdot \hat{\mathbf{n}}) dA = -\mathbf{f} - \iint_A p \hat{\mathbf{n}} dA + \iiint_V \rho \mathbf{g} dV \quad (29)$$

The time rate of change of momentum of the fluid within V , plus the rate at which momentum is carried out of V through its surface A , is equal to the total force acting on the fluid. This force comprises the negated force on any solid bodies within the fluid, \mathbf{f} (negated due to Newton's 3rd law), the surface pressure force and any other body forces (such as gravity). Note that $\hat{\mathbf{n}}$ represents the local outward directed unit normal to the control surface.

For a steady-state problem in the absence of body forces the first term on the left hand side and the last term on the right hand side vanish. The calculation procedure can be simplified by constructing an appropriately oriented cuboid control volume with boundaries located sufficiently far away from the immersed body such that only two of the surfaces need be considered. Furthermore, if one of these surfaces is located very far downstream of the body such that the local flow is entirely parallel to the freestream (and perpendicular to the surface), then the surface may be considered to be a Trefftz plane. If the body is undergoing uniform translation rather than being stationary in a uniform freestream, the control volume must also translate with the body while remaining fixed in size and enclosing the same region of fluid around the body. The two problems are analogous due to Galilean invariance.

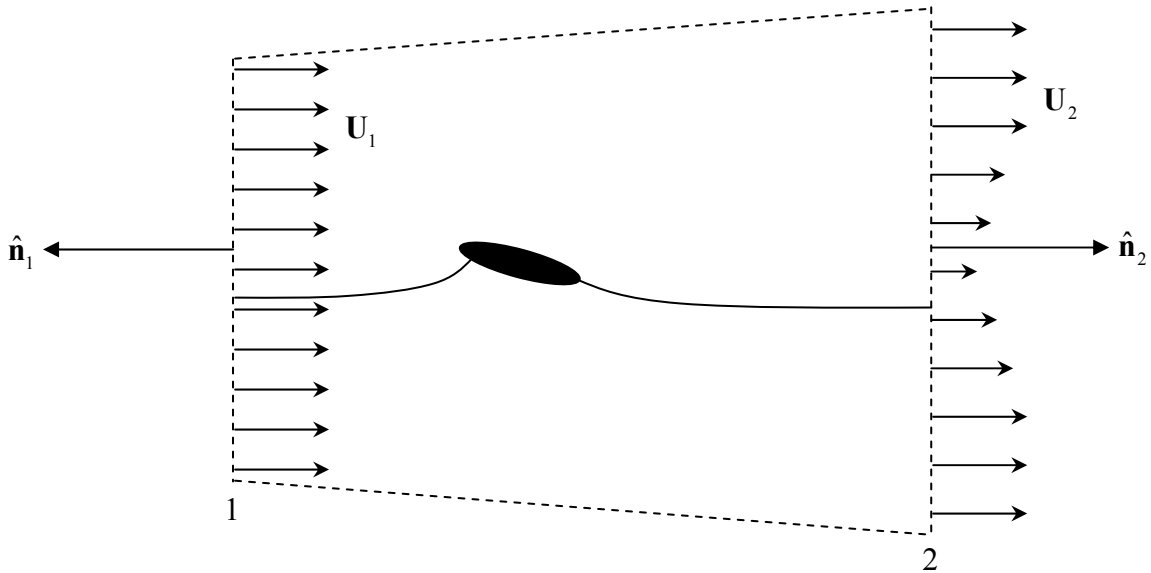


Figure 7: Example control volume around a body (viewed in cross-section)

The configuration illustrated above is typical for computing the drag on a body. Station 1 is sufficiently far upstream to be uninfluenced by the presence of the body such that $\mathbf{U}_1 = \mathbf{U}_\infty$ and $p_1 = p_\infty$. Likewise the other surfaces (apart from station 2) are positioned far away from the body and aligned parallel with the local streamlines such that their contribution is zero. Regarding the pressure field of the body, this is only strictly zero at infinity, however it should be noted that the perturbation velocity very far from a thick body falls off as $1/r^2$, allowing a finite distance to be acceptable in practice). In the steady-state and absence of any body forces and with constant fluid properties the force on the body is given by

$$\begin{aligned} \mathbf{f} &= - \left(\rho \iint_A \mathbf{U} (\mathbf{U} \cdot \hat{\mathbf{n}}) dA + \iint_A p \hat{\mathbf{n}} dA \right) \\ &= - \left(\rho \iint_{A_1} \mathbf{U}_\infty (\mathbf{U}_\infty \cdot \hat{\mathbf{n}}_1) dA_1 + \rho \iint_{A_2} \mathbf{U}_2 (\mathbf{U}_2 \cdot \hat{\mathbf{n}}_2) dA_2 + \iint_{A_1} p_\infty \hat{\mathbf{n}}_1 dA_1 + \iint_{A_2} p_2 \hat{\mathbf{n}}_2 dA_2 \right) \end{aligned} \quad (30)$$

Conservation of mass applied to an infinitesimal stream tube originating at some point on station 1 requires that

$$-(\mathbf{U}_\infty \cdot \hat{\mathbf{n}}_1) dA_1 = (\mathbf{U}_2 \cdot \hat{\mathbf{n}}_2) dA_2 \quad (31)$$

The force equation consequently becomes

$$\mathbf{f} = - \left(\iint_{A_2} \left(\rho (\mathbf{U}_2 - \mathbf{U}_\infty) (\mathbf{U}_2 \cdot \hat{\mathbf{n}}_2) + p_2 \hat{\mathbf{n}}_2 - p_\infty \hat{\mathbf{n}}_1 \left(\frac{\mathbf{U}_2 \cdot \hat{\mathbf{n}}_2}{\mathbf{U}_\infty \cdot \hat{\mathbf{n}}_1} \right) \right) dA_2 \right) \quad (32)$$

If the control surfaces are set up such that $\hat{\mathbf{n}}_1 = -\hat{\mathbf{n}}_2$ and that $\hat{\mathbf{n}}_2$ is parallel with the freestream direction with unit vector $\hat{\mathbf{e}}_\infty$, and fixing $p_\infty = 0$ (which is acceptable due to the relative nature of pressure (Patankar (1980) p. 130)) then the drag force is computed as follows

$$D = \mathbf{f} \cdot \hat{\mathbf{e}}_\infty = \iint_{A_2} (\rho(U_\infty - \mathbf{U}_2 \cdot \hat{\mathbf{e}}_\infty)(\mathbf{U}_2 \cdot \hat{\mathbf{e}}_\infty) - p_2) dA_2 \quad (33)$$

Only in the case of an irrotational, inviscid potential flow where the total pressure is constant everywhere (and there are no jumps in total pressure caused by, say, a propeller), the static pressure can be obtained from the pressure coefficient after multiplying through by the freestream (or reference) dynamic pressure (taken far upstream from the body). Using the definition of the pressure coefficient this gives, in the steady state with $p_\infty = 0$

$$p_2 = \frac{1}{2} \rho U_\infty^2 C_p = \frac{1}{2} \rho U_\infty^2 \left(1 - \frac{\mathbf{U}_2 \cdot \mathbf{U}_2}{U_\infty^2} \right) \quad (34)$$

Substituting the above result into the drag equation (33) and taking a factor of U_∞^2 out of the integral gives the final form

$$D = \rho U_\infty^2 \iint_{A_2} \left[\left(1 - \frac{\mathbf{U}_2 \cdot \hat{\mathbf{e}}_\infty}{U_\infty} \right) \left(\frac{\mathbf{U}_2 \cdot \hat{\mathbf{e}}_\infty}{U_\infty} \right) - \frac{1}{2} \left(1 - \frac{\mathbf{U}_2 \cdot \mathbf{U}_2}{U_\infty^2} \right) \right] dA_2 \quad (35)$$

Observe that the first term in the integral is in fact the integrand of the momentum thickness integral. Thus the drag is directly related to the momentum thickness of the wake and also to the pressure field in the wake (where, by inspection, it can be discerned that a negative gauge pressure in the wake will augment the drag on the body).

In the present context, the velocity vector at some point on the control surface is evaluated using equations (7) and (12) but replacing the panel control point with the point under consideration. In the usual manner, the contribution from each body panel and wake panel is summed. Supposing planar surfaces are used, these may be represented by a Cartesian grid of points of sufficiently small spacing and the integration can be carried out numerically using either simple block summation or higher order methods such as the double trapezium rule using iterated integrals (making use of Fubini's theorem). The order of iteration can be carried out in both ways and the final results averaged.

Validation and Testing

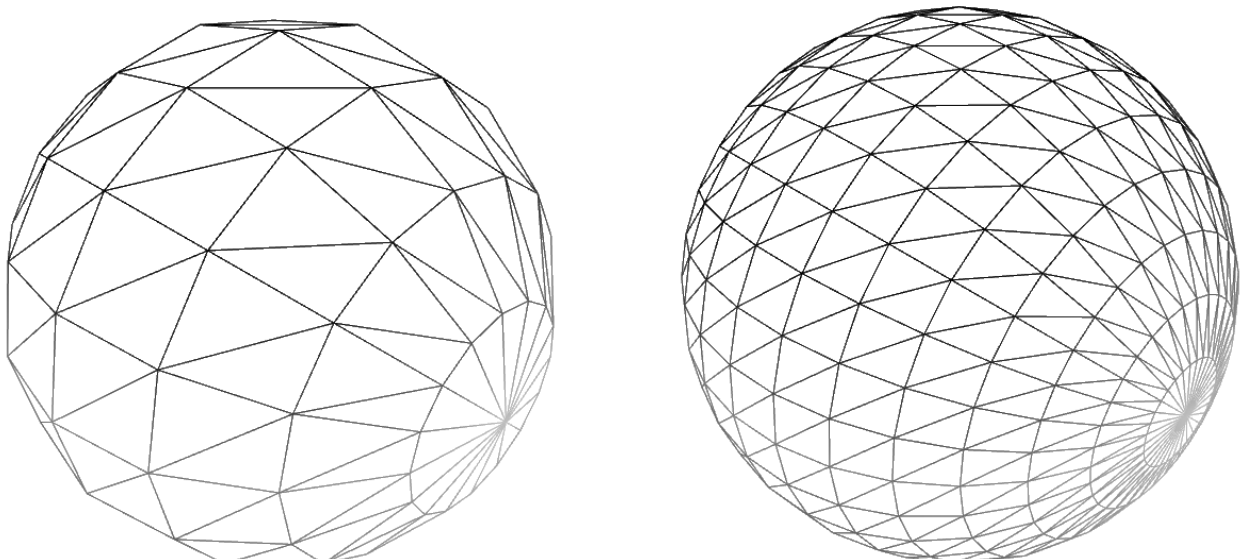
The vortex lattice method developed in this report was implemented in Visual Basic .NET code from scratch. Microsoft DirectX 9.0c was used to enable interactive, hardware-accelerated 3D graphical visualisation. The code was developed incrementally starting with the simplest non-lifting single-body, steady code (i.e. based around equation (9)). Once successfully validated using the test case of a sphere (where the analytical solution is known), the code was extended to lifting single-bodies with unsteady conditions. It should be noted that this was a rather involved task, in particular due to the extensive checking that must be done at each stage of the solution and post-processing, often involving manual examination of the matrices to check that all values are in the correct place. The alternative matrix formulation given by equation (18) was used since this was the simpler option when upgrading the existing code. This code was validated with various tests of a planar finite wing with cross section of a Van de Vooren 15% thickness ratio aerofoil with 20° trailing edge angle. Effects of angle of attack as well as aspect ratio were examined. Finally, the code was extended to allow multiple bodies (both lifting and non-lifting in combination). This final stage provides one with the in-house ability to model the dynamics of a full aircraft. The final stage of the code is showcased with a propeller and spinner combination.

Test Case 1: Uniform Steady Flow over a Sphere

A unit sphere was drawn using Unigraphics Solid Edge V20 and then output in the .STL (stereo lithography) format which provides a triangulated version of the solid body. The degree of tessellation can be controlled, which allowed testing of the effects of the number of panels on the solution accuracy. The analytical solution for the surface pressure distribution around any great-circle of the sphere is, in polar coordinates

$$C_p = 1 - \frac{9}{4} \sin^2 \theta \quad (36)$$

Four unit spheres comprising 224, 960, 4970 and 9800 panels were tested. Since the body is closed, the matrix equation was solved using Gauss-Seidel iteration to a tolerance of 1×10^{-6} . Wireframe renderings of their surfaces (with back-face culling) are shown below



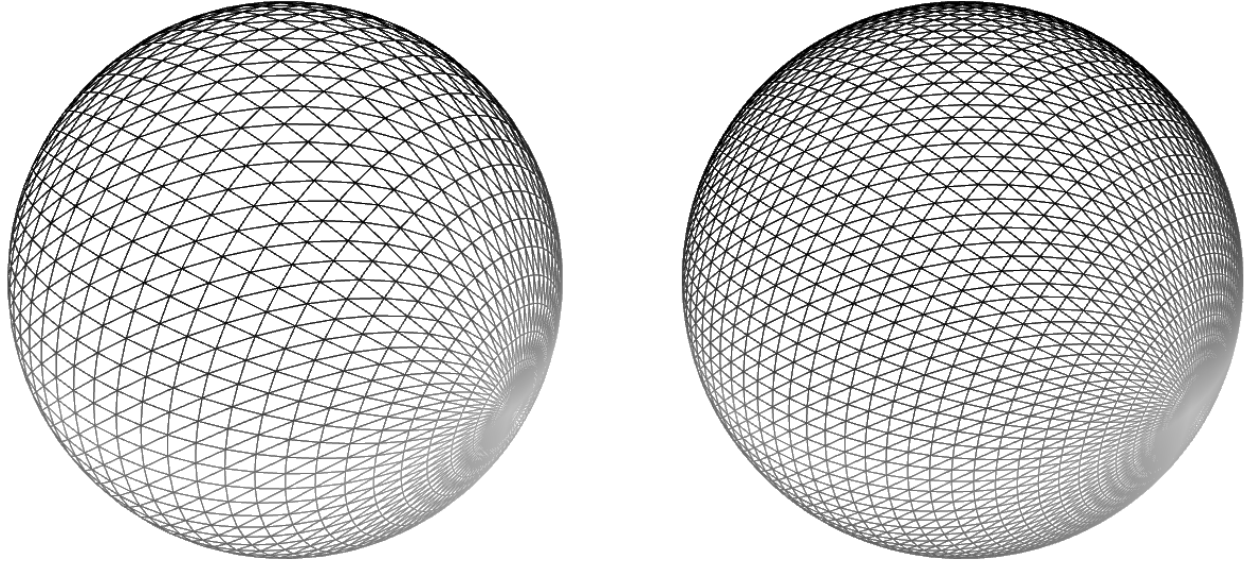


Figure 8: Surface triangulation of the sphere with increasing mesh density

Using vertex-averaged and interpolated shading it is possible to render images that make computational fluid dynamics live up to its alternative label of ‘colourful fluid dynamics’. The image below shows the surface coloured by pressure coefficient using modified Bernstein polynomials for the colouring. Red denotes $C_p = 1$ and, blue denotes $C_p = -1.25$. Also, a hundred passive tracer particles were positioned randomly in a plane upstream of the sphere and advected by the local flow using the same equation as for the wake advection (16) (although there is no wake in this case).

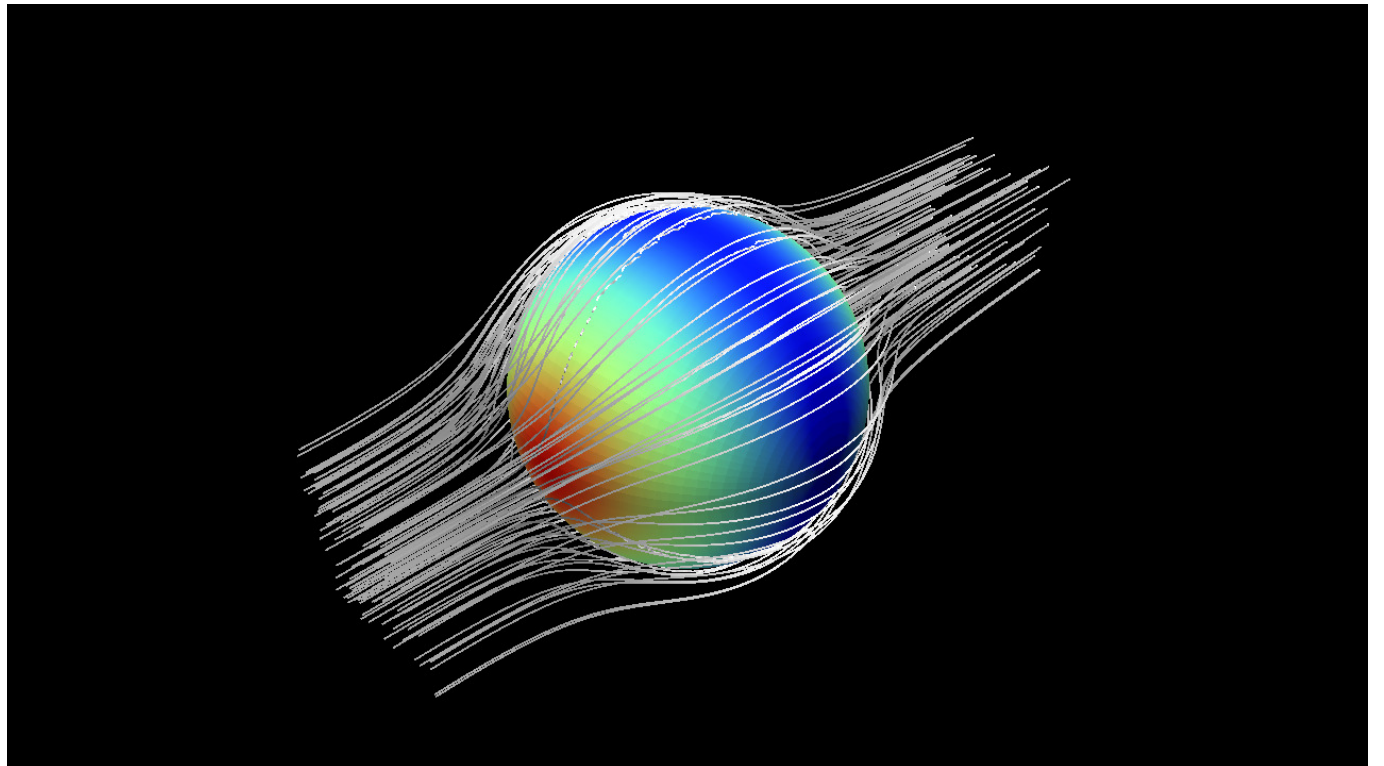


Figure 9: Flow over the highest resolution sphere coloured by surface pressure coefficient. 100 passive tracers also reveal the streaklines of the incident flow

The pressure maximum at the front of the sphere is clearly visible and the pressure minimum forms a band around the centre-station of the sphere. Observe how one of the streaklines near the top contains wiggles. This is a result of the aforementioned issue with the surface tangential velocity not being represented by the Biot-Savart law alone and the use of a low order method. The graph below shows how

the results compare with the analytical solution given above, as well as the effect of mesh density on the accuracy. The pressure coefficients were taken along the central diametric station of the sphere and are presented in polar coordinates to make a clear distinction between the front and rear regions.

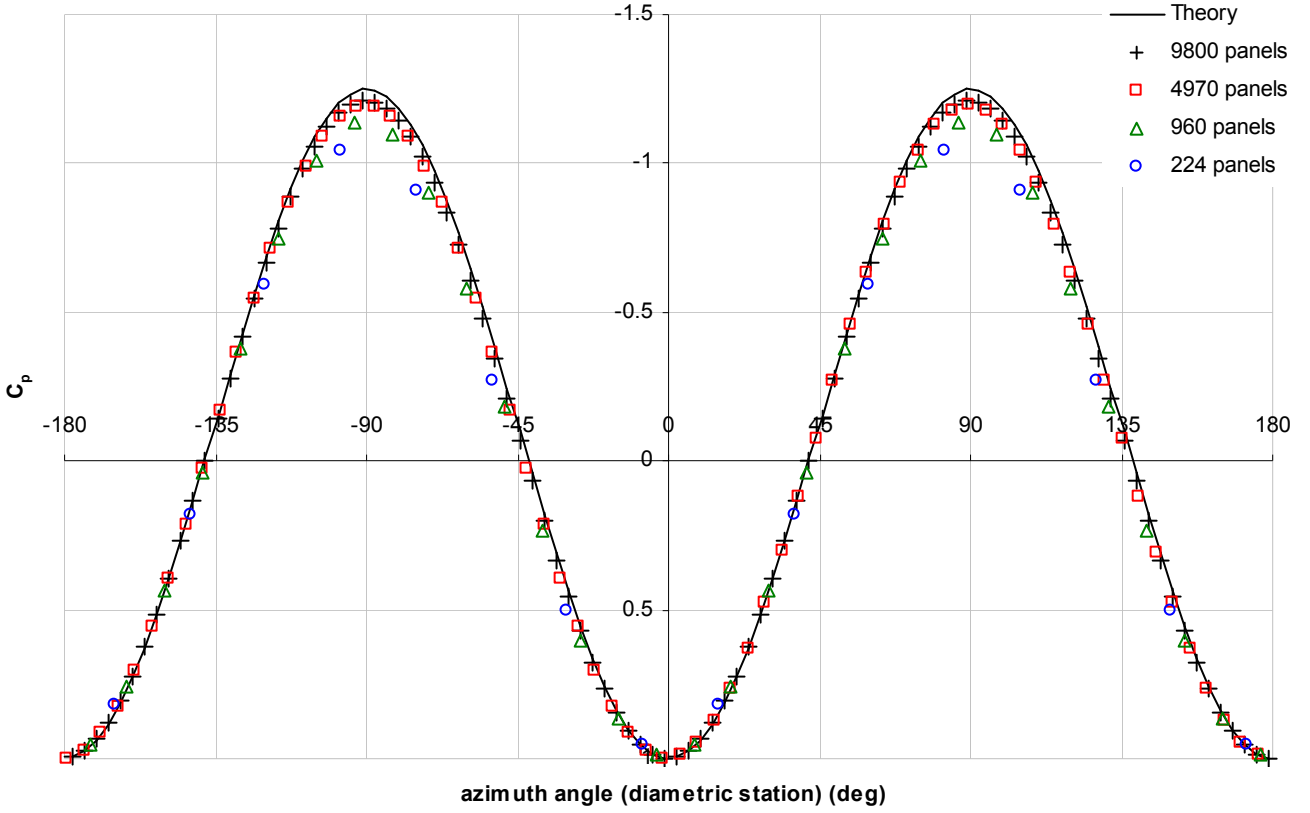


Figure 10: Pressure coefficient against azimuth angle for a sphere showing the effect of mesh density

The results are in very good agreement with the analytical solution except in the vicinity of the pressure minimum. Furthermore there is excellent symmetry between the hemispheres which means that the calculated drag is zero (within the precision of the numerics) as it should be for a potential flow. Visually it appears there is no real advantage in going from 4970 to 9800 panels but that at least 1000 panels are needed for a decent visual representation of the pressure distribution. However it is the numbers that ultimately matter – the peak relative error was, in order of decreasing mesh density: -3.07% , -4.3% , -8.56% , -13.95% . Graphical representation of the absolute relative errors reveals a $-2/5$ power law in error as a function of the number of panels

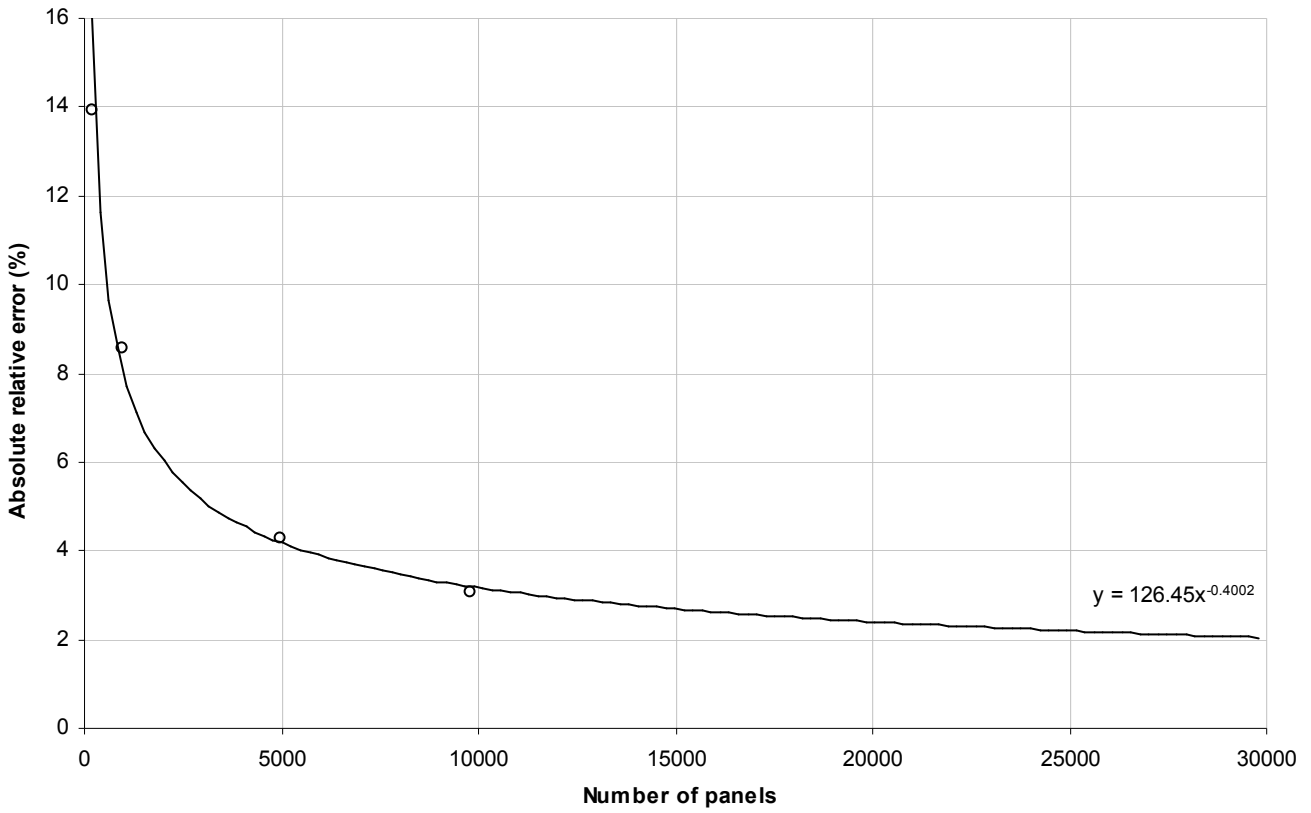


Figure 11: Absolute relative error of minimum pressure as a function of the number of panels

Evidently it is a case of diminishing returns in order to gain even an extra percent beyond the 3% error with 10k panels for the unit sphere.

The sensible results returned by this fundamental test case of the unit sphere do indeed validate this code for steady flows over non-lifting bodies. Since this code forms the kernel of the subsequent enhancements to include unsteadiness and lifting bodies, it is very important that it checks out correctly.

Test Case 2: Uniform Steady Flow over a Finite Wing

A prismatic, untwisted wing with unit chord and aspect ratio $AR = 2$ was used for this test case. The cross sections were Van de Vooren 15% thickness ratio aerofoils with 20° trailing edge angle discretised into 45 points (trailing edge to trailing edge inclusive) with a cosinal distribution to enhance resolution at the leading and trailing edges. Aspect ratios of 20 and 200 were tested simply by stretching the base mesh in the spanwise direction. The wing comprised 21 spanwise stations giving a spacing between stations of $0.1c$. The base mesh is shown below, note the open ends. Although the ends can be closed, the iterations per time step would increase dramatically since the solution vector must be reset before every new time step due to the indeterminate nature of the matrix. The effects of the open ends were shown to be negligible on the calculated forces and overall wake shape (the largest difference occurring at the wing tips at the trailing edge in the form of a slight change of panel angle)

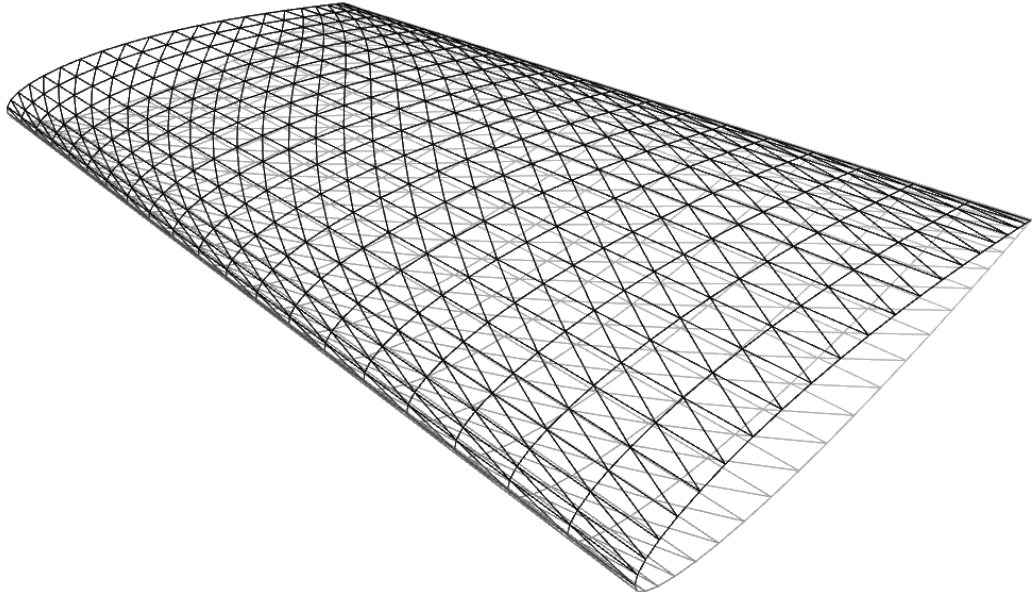


Figure 12: Surface triangle panels of the AR=2 test wing

The wing was kept stationary in a freestream of unit velocity magnitude directed in the direction of the aerofoil chord line when at zero degrees angle of attack, α . For $\alpha = 0, 5, 10, 15^\circ$ the wake was allowed to develop for four chord lengths behind the trailing edge as this was deemed sufficient for steady state conditions to be established to a satisfactory degree (with respect to the forces generated by the surface pressure distribution). For the higher aspect ratio cases, the proportion of the wake extent and wing span was maintained by scaling up the time step. This was done to keep the calculation time constant at the expense of spatial resolution. A single angle of attack for the $AR = 2$ case required three minutes to complete, running on a single core AMD Phenom X2 at 3.5GHz (overclocked by 0.4GHz from stock). The $AR = 200$ case required eight minutes due to the increased number of iterations of the matrix equation needed to keep within the tolerance.

Before examining the numerical outputs it is informative to view the graphical outputs revealing the structure of the vortex wake sheet as well as the distribution of surface forces. Furthermore passive tracer particles can be used to visualise the flow field in the vicinity of the wing tip vortices as well as the starting vortex. The following images show the wake sheet for each of the α 's tested on the $AR = 2$ wing. The non-dimensional time step (defined by $t' = tU_\infty/c$) used for all the sub-cases was 0.1 (such that the attached wake panels were square, which is not a requirement but helps to view the nature of the distortion of panels as the wake evolves). The surface of the wing was coloured by the surface pressure coefficient, with red representing $C_p = 1$ and blue representing $C_p \leq -1.25$

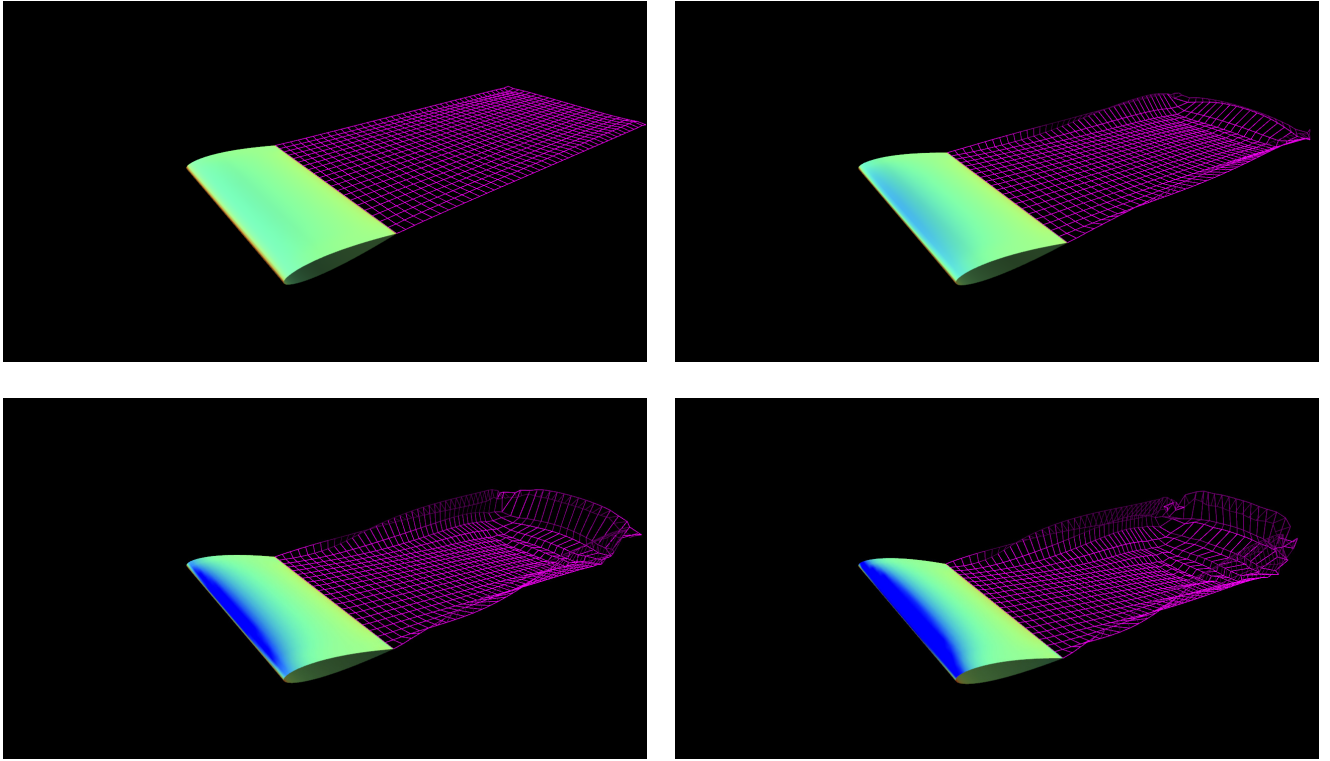


Figure 13: Evolution of the wake sheet to $4c$ downstream of the trailing edge for $\alpha = 0, 5, 10, 15^\circ$ respectively

At zero incidence there is no wake rollup since there is no bound circulation, which implies that the attached wake panels have zero strength for all time (Kutta condition is satisfied by the symmetry of the problem). The slight perturbation at the tips is correlated to the order in which the rows of the matrix equation are iterated, indicating that either a tighter tolerance and/or reduced initial time step were required or some form of pre-conditioning of the matrix before iteration. As α is increased, the wake sheet begins to rollup at the ends. The degree of rollup increases with α . It is important to note from observations of the evolution in time that it is not the edges of the wake sheet that are lifted upward but rather that the central region is advected *downwards* by the tip and starting vortices – the wake-induced downwash. Also observe how the negative pressure falls off towards the wing tips. This is caused by the intense tip vortices altering the incident flow angle near the tip stations by creating an outwash on the underside and an inwash on the upper side – i.e. the streamwise flow is given a spanwise component thereby decreasing the local pressure minimum due to the streamlines taking a path of lower curvature over the wing and therefore less acceleration. The tip vortices and spanwise flow are ultimately created by the potential difference between the upper and lower surfaces “leaking” over the wing tips inducing velocity with components lying in the plane perpendicular to the tip chord line (i.e. swirl).

The following images reveal the streaklines around the tip vortices for the $\alpha = 15^\circ$ case. A total of 150 passive particles were placed randomly in two planes $0.5c$ upstream of the wing tips, extending beyond the wing tips by $0.125c$ and into the wing by $0.35c$, positioned in such a way that all particles passed under the wing. This helped to reveal the spanwise flow near the trailing edge as well as the tip vortices themselves which are mostly composed of flow from the underside of the wing swirling over the tips. One of the special features of the code written for this report was the ability to pause the simulation and fly around the solution as though in a computer game. Thus it was possible to fly through the eye of the tip vortex as well as pretend to be a small bug sitting on the wing and watching the wake evolve – an experience indeed unique to the realm of computation!

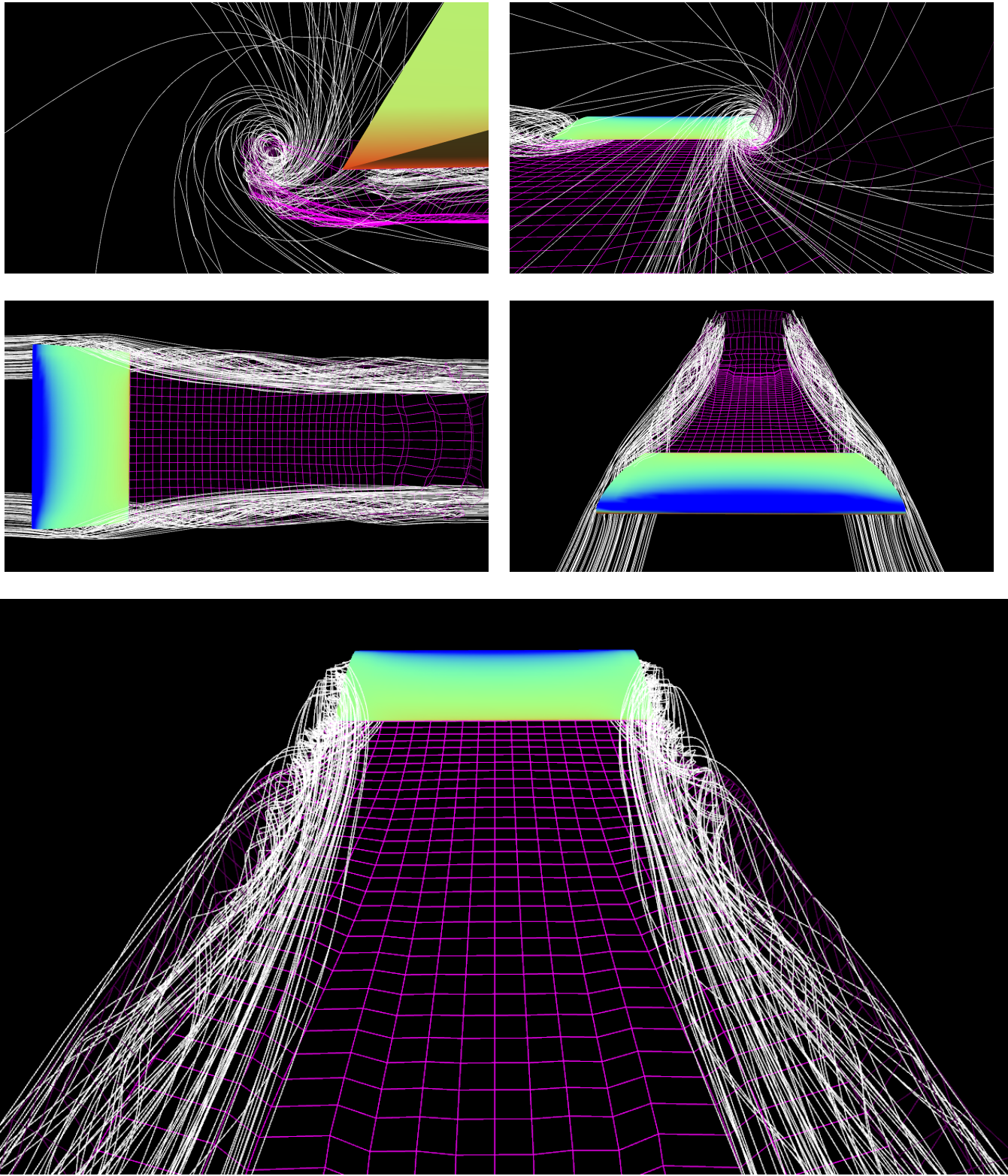


Figure 14: Passive tracer particle streaklines revealing flow around the wing tips into the wake

The first two images are looking into one of the tip vortices from upstream and downstream respectively. The final image shows the sets of streaklines originating from beneath the wing and from having leaked around the tips.

The starting vortex can be revealed by randomly scattering tracer particles in the vicinity of the trailing edge and then impulsively starting the aerofoil motion in the upstream direction (with zero freestream velocity). The two images below show the starting vortex for $\alpha = 15^\circ$ in general view as well as looking through the eye of the vortex

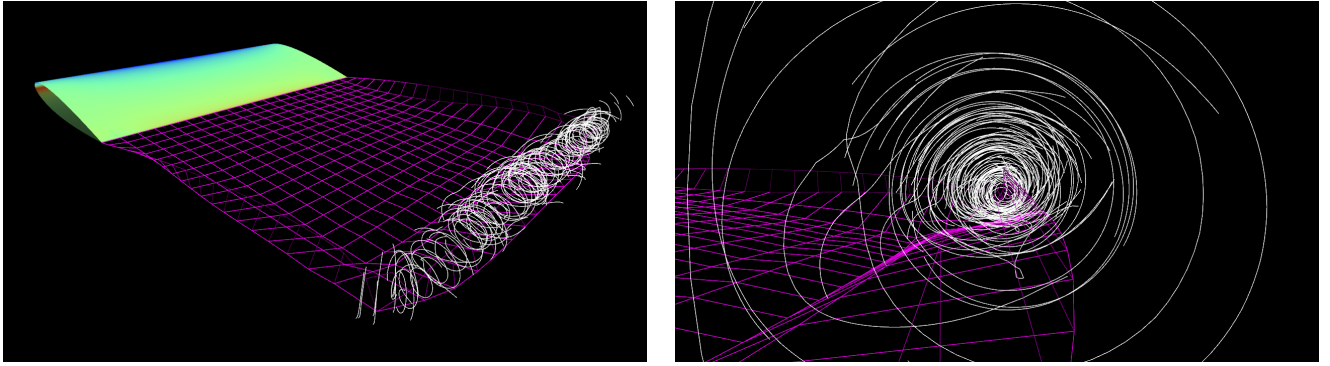


Figure 15: Passive tracer particle streaklines revealing the starting vortex

Lastly, the surface forces on the wing are visualised using equation (28). The force vectors were scaled up by some factor for the purpose of qualitative viewing. Blue denotes suction and red denotes overpressure.

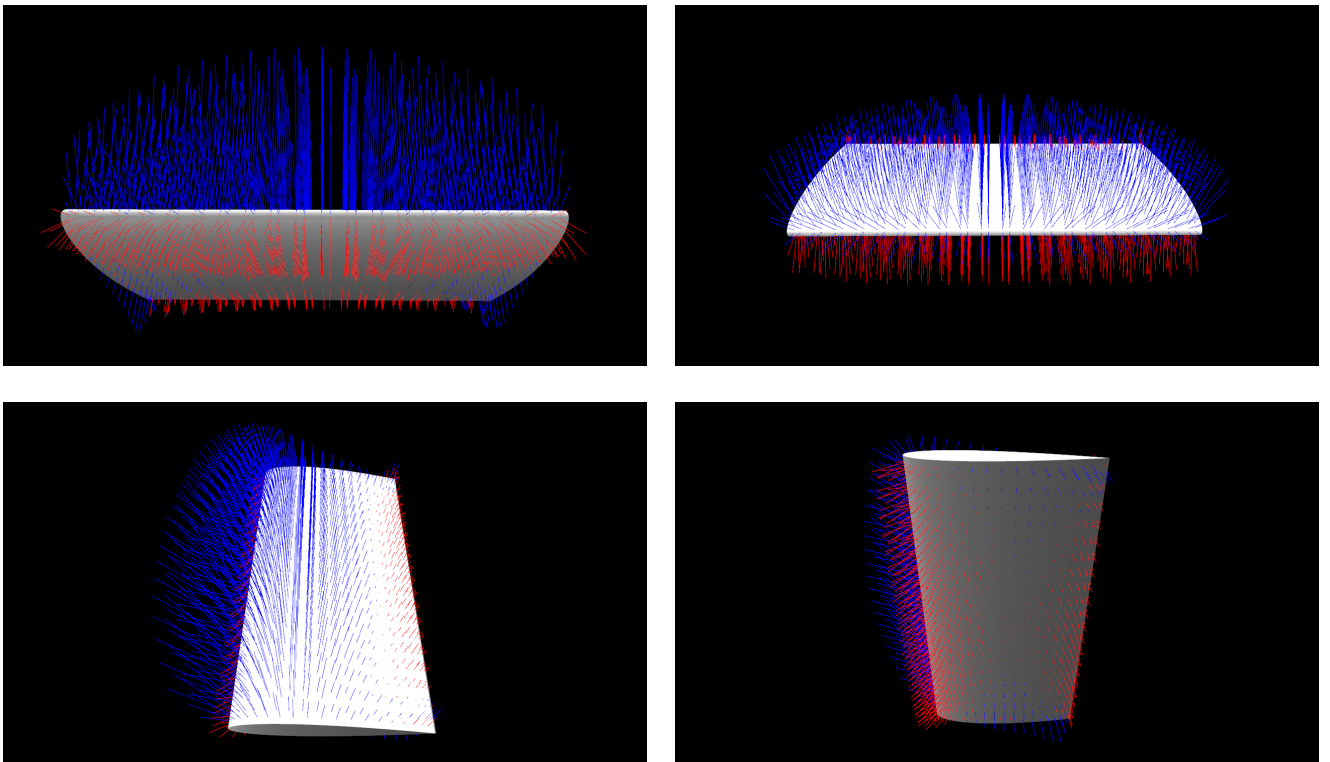


Figure 16: Surface force distribution on the wing

The images reveal two important physical features. Firstly that the suction forces taper off towards the wing tips, and secondly that there is actually a weak suction force at the wing tips towards the trailing edge on the top surface, and to a deeper extent toward the centre of the wing on the lower surface. This is caused by the flow accelerating around the tips creating a reduced pressure. The presence of an established tip vortex will also augment this effect by also altering the local incident flow.

After this sufficient dose of colourful fluid dynamics eye-candy, it is necessary to examine the numerical outputs. The lift, induced drag and moment coefficients were output at each time step along with the surface pressure coefficient distribution. Firstly, the surface pressure coefficient distribution taken over the central station is compared to the analytical solution for the aerofoil cross-section (effectively a wing with $AR = \infty$). This is done for the three aspect ratio cases, 2, 20 and 200 at $\alpha = 0$ and $\alpha = 10^\circ$. In order to keep x/c the same for all angles, the freestream was rotated rather than the wing.

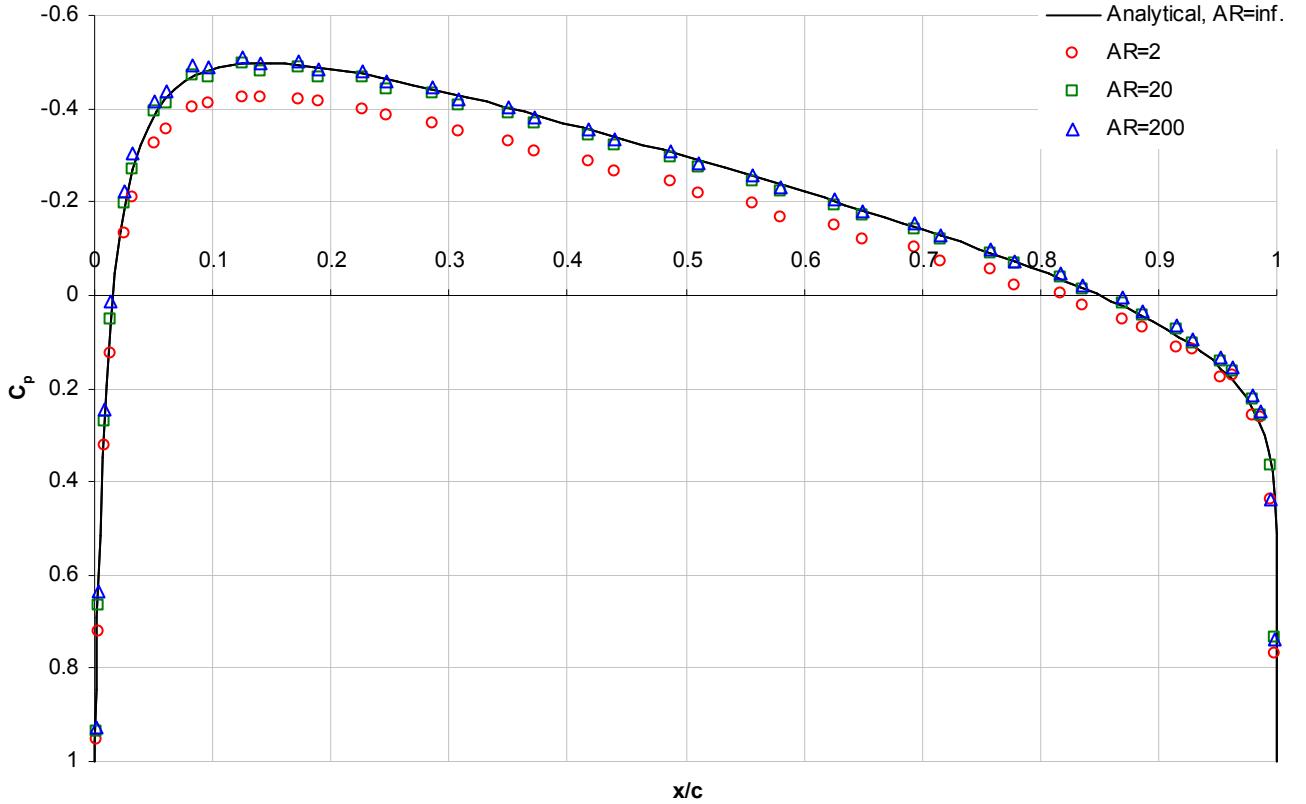


Figure 17: Pressure coefficient distribution at the wing central station, $\alpha = 0^\circ$

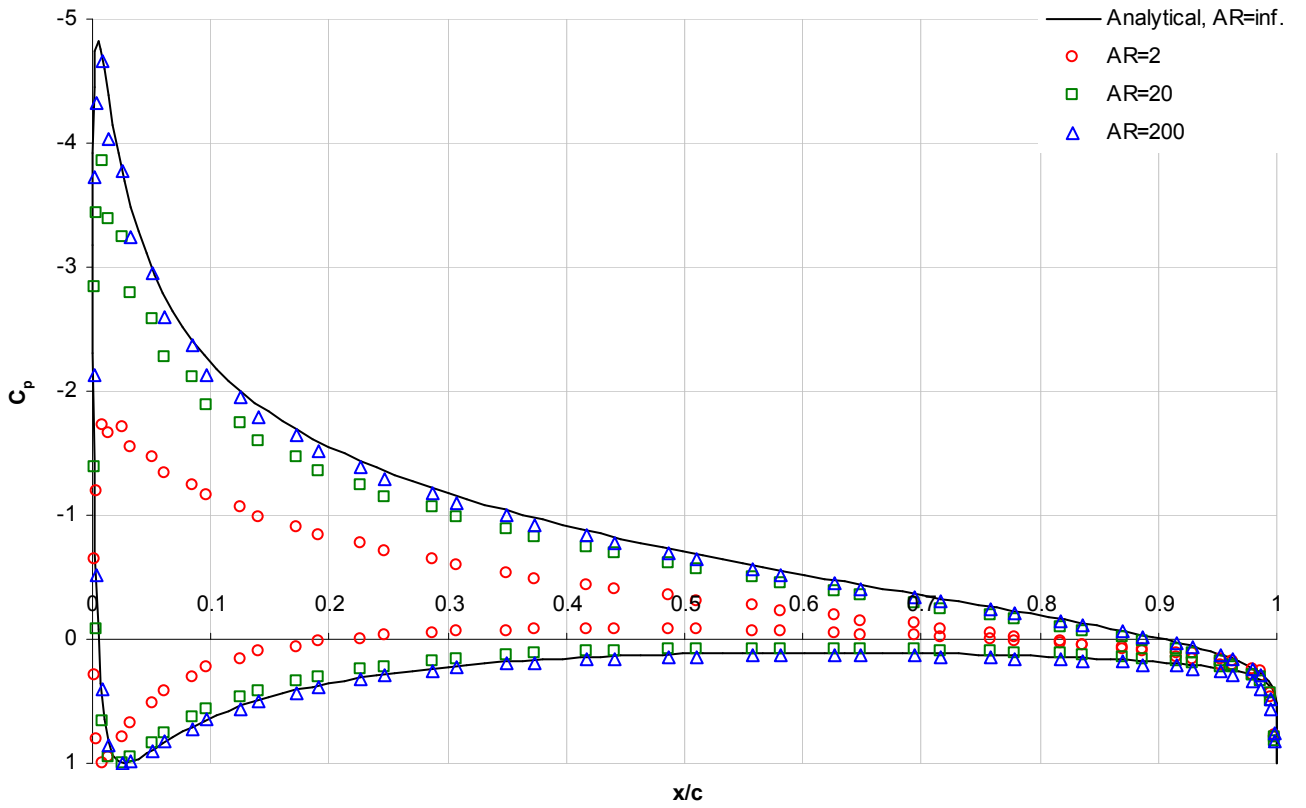


Figure 18: Pressure coefficient distribution at the wing central station, $\alpha = 10^\circ$

Even at zero incidence the aspect ratio affects the pressure distribution, although to a lesser extent than at incidence. There is no enclosed area within the C_p curves with $\alpha = 0^\circ$ and so there is no lift force (as should be the case for this symmetric profile). As the aspect ratio increases, the analytical solution is approached. The stagnation points at the leading and trailing edges are also well captured. With $\alpha = 10^\circ$ a

similar trend is observed, with the higher aspect ratio solutions approaching the analytical solution in an asymptotic manner. Regarding validation of the code for lifting bodies, it is also important to notice that the stagnation point at the trailing edge is well captured, without any loops in the pressure distribution upstream of the trailing edge (which, in the steady-state, would indicate an unfulfilled Kutta condition). The C_p value at the trailing edge is also very close to 1.0 (perfect stagnation), which is good considering the medium resolution of the aerofoil profile (in Nathan (2011) the same 2D aerofoil was analysed using 180 points, exactly quadruple the resolution used here). Thus the attached wake panels are indeed correctly enforcing the Kutta condition at the trailing edge, implying their strengths are being correctly calculated and assigned. It is informative to examine how the pressure distribution develops over time. The graph below shows the pressure coefficient distribution at early and late stages for the $AR = 2$ wing

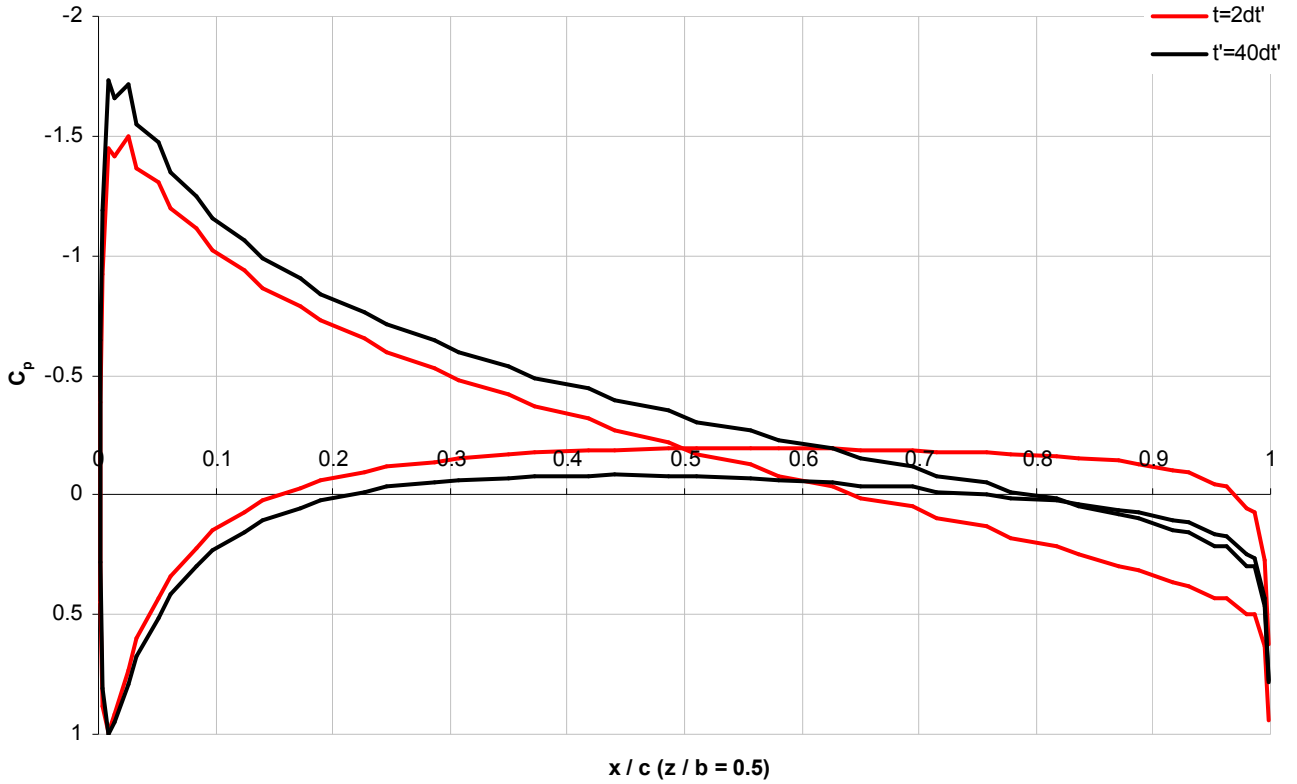


Figure 19: Development of the central station surface pressure coefficient distribution over time

The wiggles in the curves are symptomatic of the low resolution of points describing the station aerofoil contour. Despite the Kutta condition being instantaneously established (a specified feature of the unsteady potential flow model) the pressure distribution is not immediately established. A “node” is visible at the mid-chord location (the fact that it is mid-chord is mere coincidence for this particular geometry). This node disappears once the wake sheet is sufficiently established in space and changes in surface potential caused by the wake development diminishes such that the unsteady term in the pressure coefficient equation (19) becomes negligible – i.e. steady-state values are attained. Therefore it is not unusual to see such nodes in the pressure distribution for flapping wings or oscillating freestreams.

The matching of pressure coefficient values is itself sufficient validation of the code since it indicates that the fundamental equations dealing with the fluid dynamics are being correctly implemented. However equally important in terms of engineering application is the validation of the post-processing tools to compute the force on the body. Next the temporal evolution of the lift, induced drag, and moment coefficients is shown up to $t' = 40$ (the end-time of the $AR = 200$ case is $t' = 400$). Note that these are the coefficients for the whole body (not just the central section coefficient).

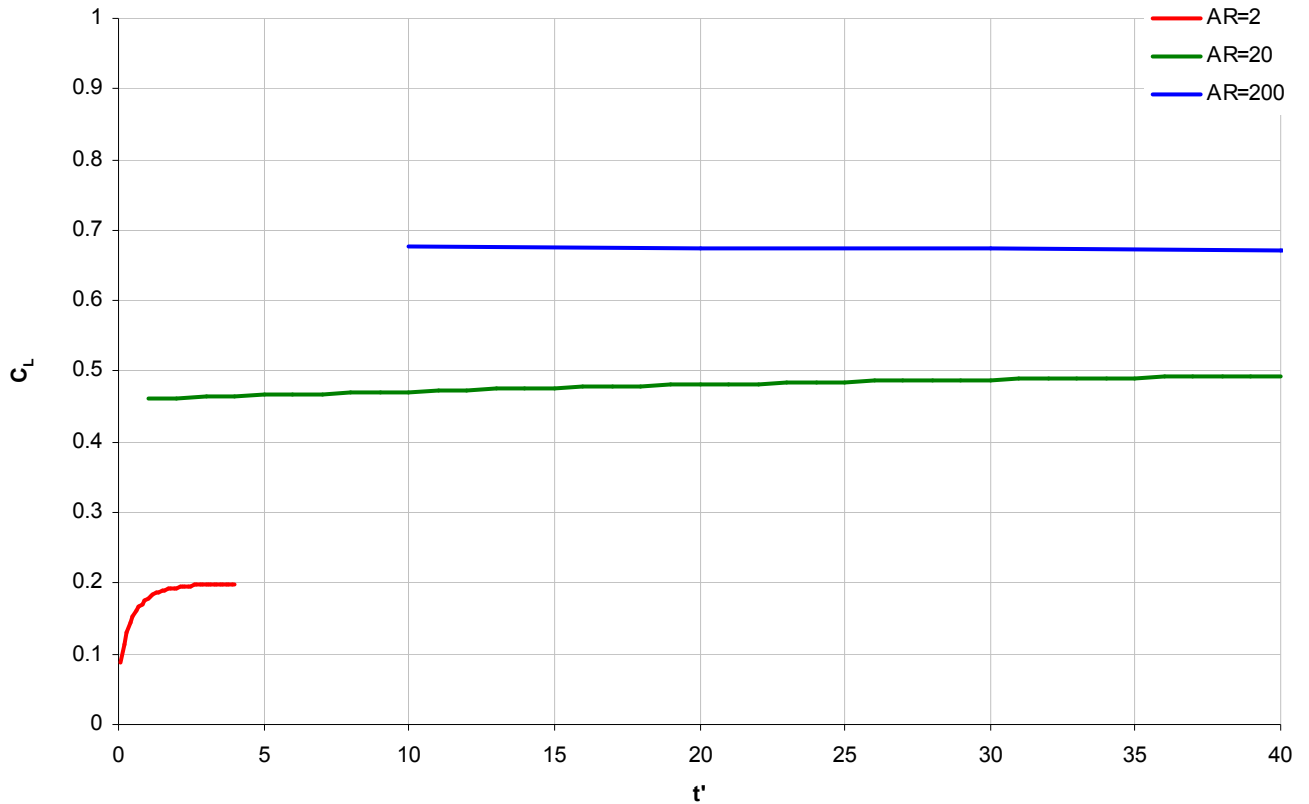


Figure 20: Temporal evolution of the wing lift coefficient

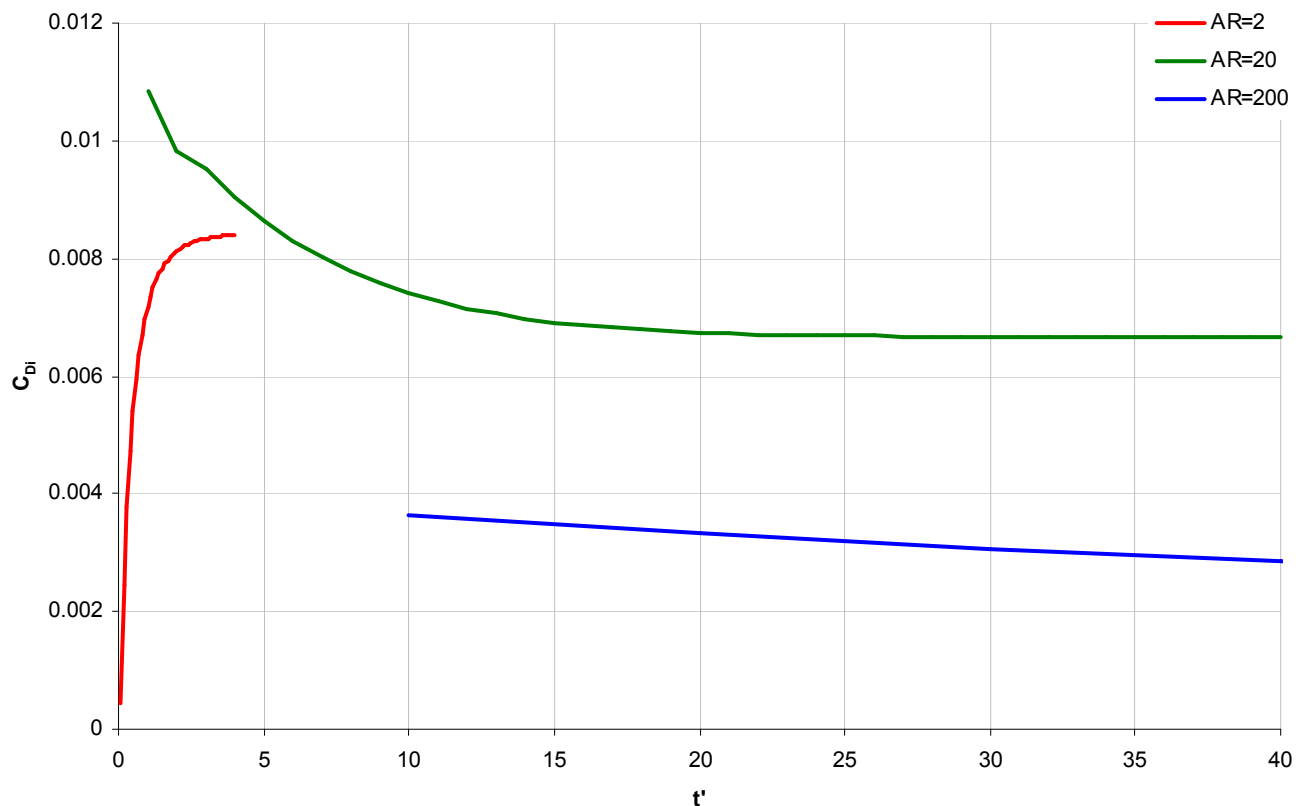


Figure 21: Temporal evolution of the wing induced drag coefficient

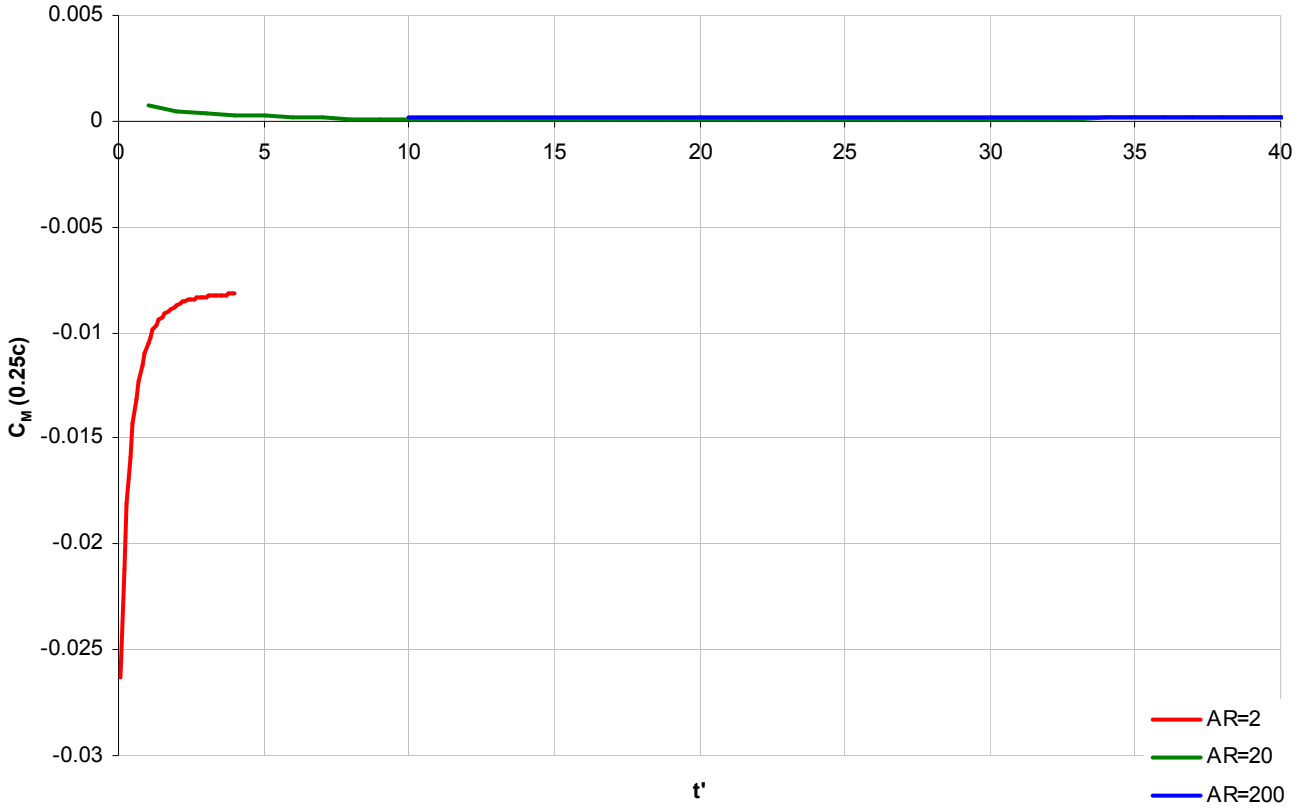


Figure 22: Temporal evolution of the wing spanwise moment coefficient (about the quarter-chord line)

Immediately observable is the fact that the wings of higher aspect ratio take longer to reach the steady-state (c.f. Katz & Plotkin (2001)). As the aspect ratio is increased, the following trends are observed: Final lift is increased, final induced drag is decreased, and final moment coefficient about the quarter-chord line tends to near-zero. For the $AR = 2$ wing although the steady-state lift coefficient is established by $t' = 4$ it appears that the drag and moment coefficients require some additional time to reach steady state. A similar behaviour was observed in the 2D case (c.f. Nathan (2011)).

Using the steady-state values, the lift, induced drag and moment coefficients can be plotted as functions of α and the lift-drag polar may be constructed. These can be compared to the theoretical values obtained from thin finite-wing theory supposing an ideal elliptical loading (Oswald efficiency factor $e = 1$). The equations are

$$C_L = \frac{m_0}{1 + \frac{m_0}{\pi A R e}} \quad (37)$$

$$C_{Di} = \frac{C_L^2}{\pi A R e}$$

In all the following graphs, dashed lines are the results from theory. The lift and moment coefficients have linear trend lines fitted through them and the drag coefficients have quadratic trend lines fitted through them (as the theoretical results predict). The lift curve slope is obtained from the 2D aerofoil result in Nathan (2011) and is $m_0 = 1.11092(2\pi)$.

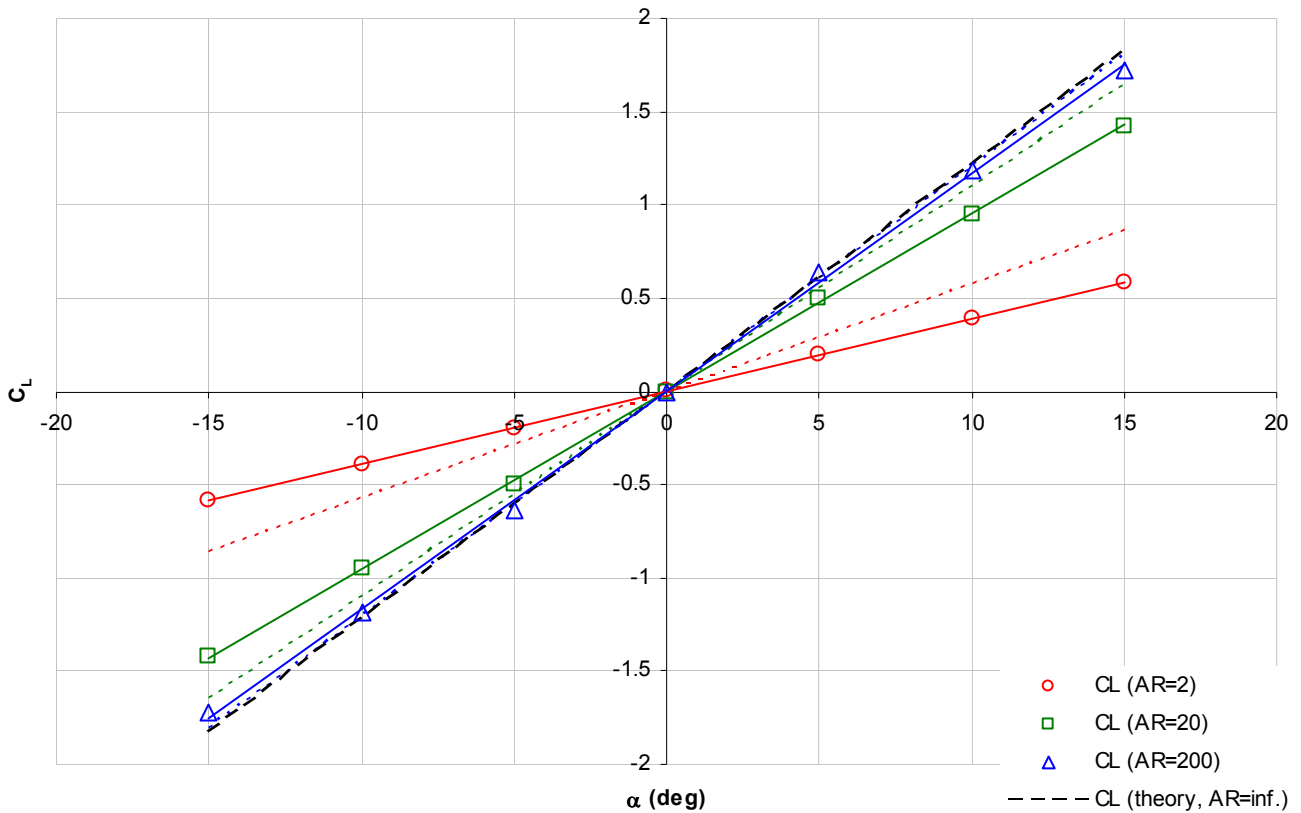


Figure 23: Steady-state lift coefficient as a function of angle of attack

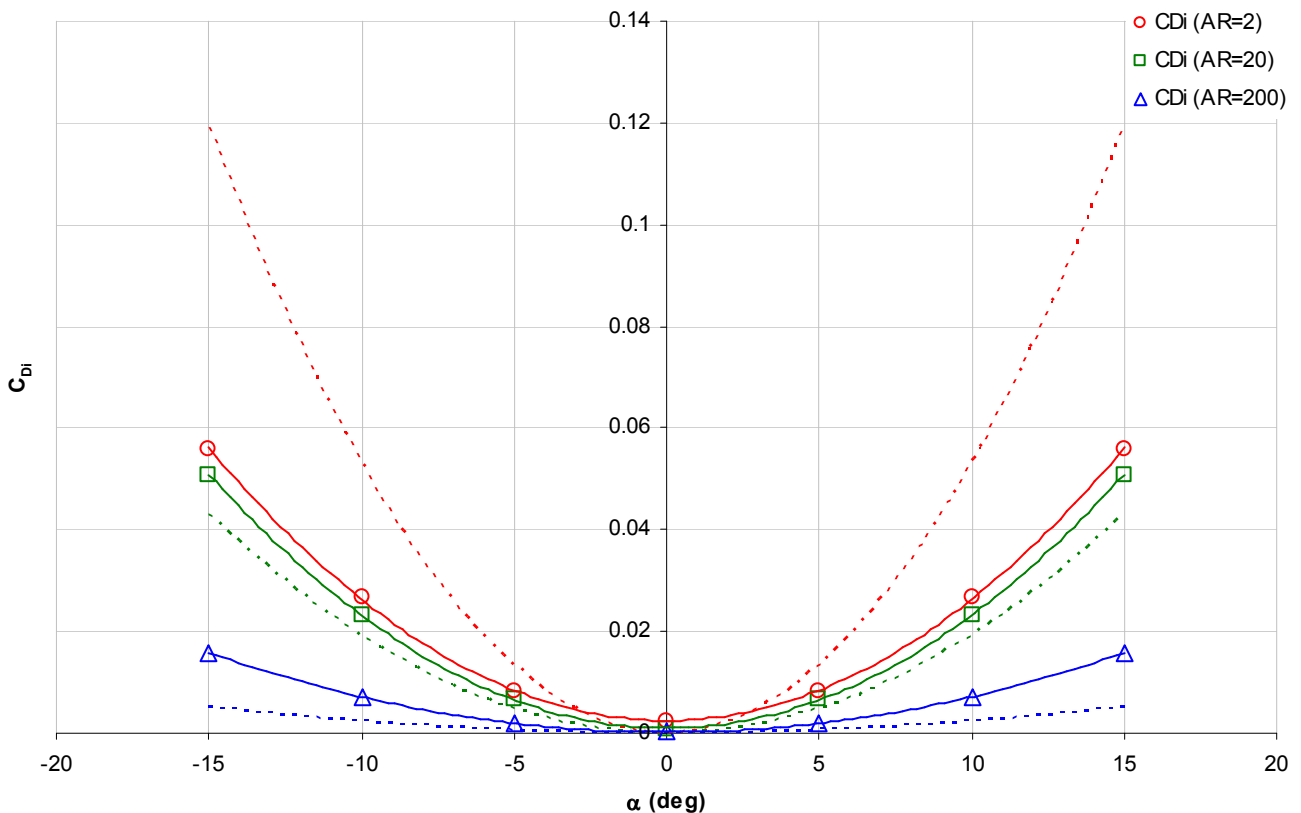


Figure 24: Steady-state induced drag coefficient as a function of angle of attack

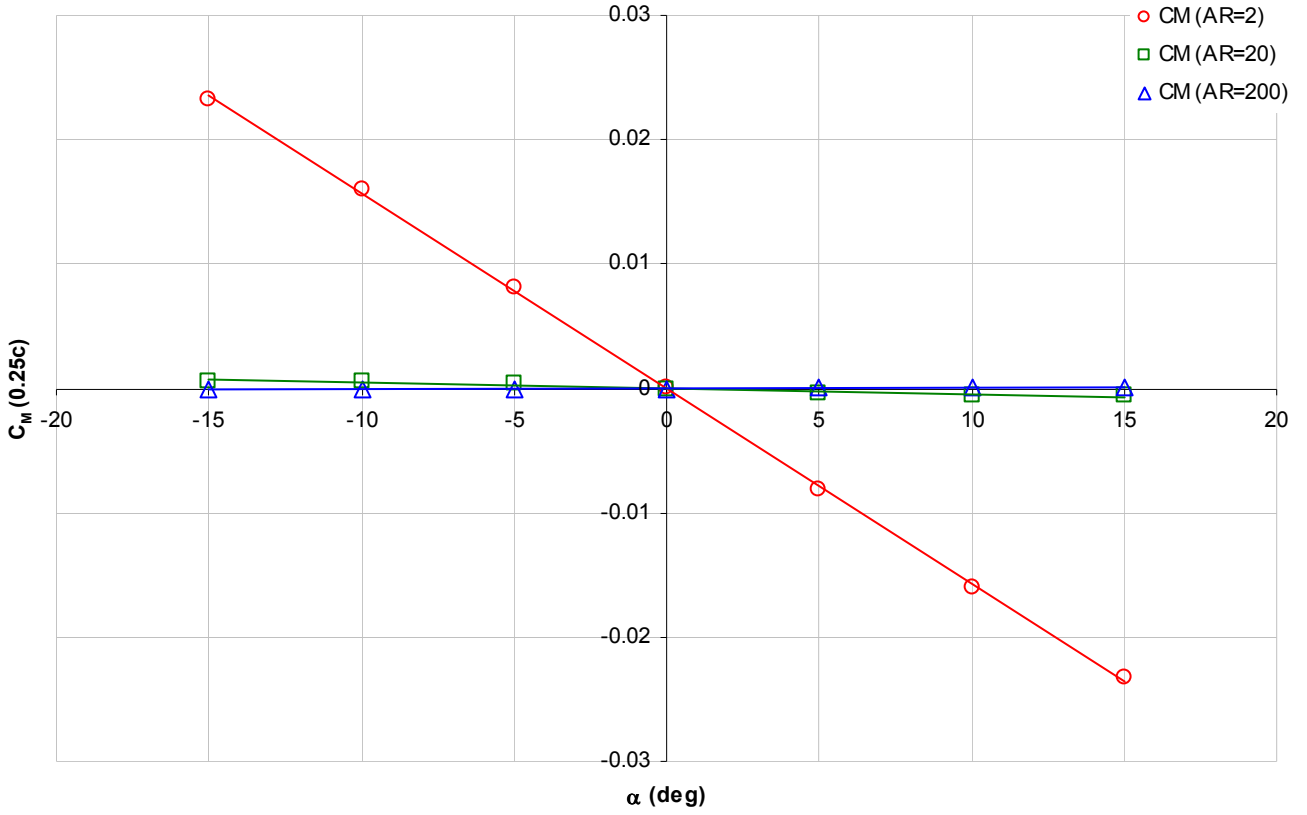


Figure 25: Steady-state quarter-chord moment coefficient as a function of angle of attack

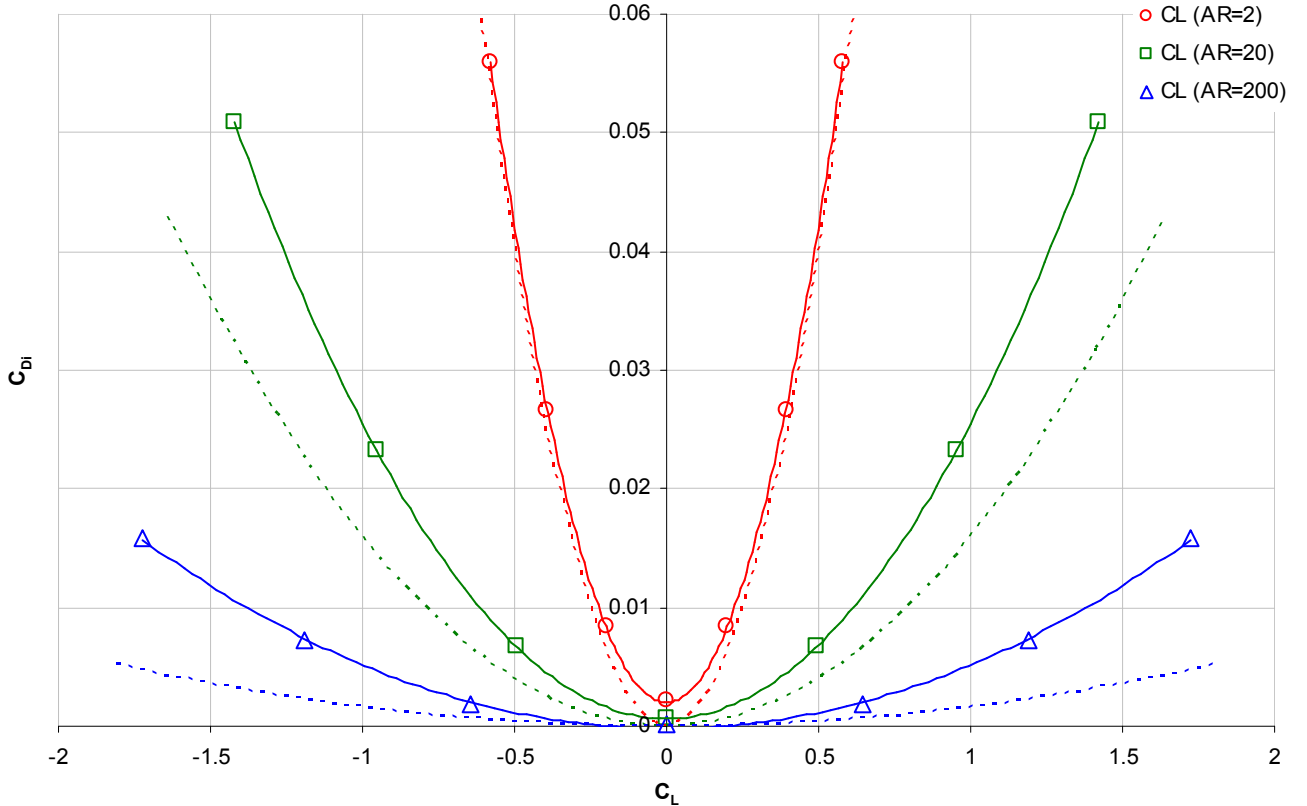


Figure 26: Steady-state lift/drag polar

The linear nature of the lift coefficient variation and the moment coefficient variation, and the quadratic variation of the induced drag coefficient variation indicate that the fundamental physics inferred from the code and post-processing is correct. In fact it is arguably more important that the trends are correct over the absolute values themselves (although ideally the latter would be correct as well). The lift curve slopes are consistently over-predicted by the computational results for all aspect ratios, however the error

decreases with increasing aspect ratio and, importantly, the highest aspect ratio case remains bounded by the infinite aspect ratio theoretical result. The induced drag is substantially under-predicted for the lowest aspect ratio case and then over-predicted for the higher aspect ratios. One significant issue that is unphysical is the prediction of a non-zero drag at zero incidence (or zero lift). Such a drag can only arise due to viscous effects (profile drag) from the boundary layer skin friction which is not modelled here. This error appears to decrease with increasing aspect ratio. Without further investigation one can only speculate that this may be an issue caused by the resolution of the wing surface panelling, the resolution of the wake panels and the time step. Lastly, the fact that the quarter-chord moment coefficient tends to zero with increasing aspect ratio regardless of angle of attack is in agreement with the theoretical results from thin aerofoil theory.

The disagreement with the theoretical results is not sufficient to lead to a conclusion that the computation is in error, since the assumptions behind the thin finite wing theory (Prandtl's lifting line theory of 1918) may break down for very small aspect ratios and large angles of attack. For example the wing is represented by a succession of infinitesimal horseshoe vortices with a specified circulation distribution, and these horseshoe vortices extend to infinity downstream (i.e. they are semi-infinite horseshoe vortices). This means that the wake is always aligned with the wing and does not undergo self-advection as the present computational model allows. Therefore for large incidences and small aspect ratios – where the effects of wake roll-up are significant – the wake model of the lifting line theory is likely not force-free and quite inaccurate. Thus one would expect the agreement to improve as the aspect ratio increases and the angle of incidence decreases. Furthermore, the lifting line theory supposes the wing is effectively represented by a single line of varying spanwise circulation and the effect of thickness is not considered. There is also the issue of the small-angle approximation. Thus the theoretical predictions should only be used to establish general trends (i.e. basic physical principles) than to measure errors based on absolute values.

In order to check for self-consistency of the induced drag calculations, a comparison between the induced drag inferred from surface force calculations and from the wake survey method was also carried out. Since the wake survey equation (35) was based on steady-state values, there exists the issue of what distance downstream of the wing trailing edge to place the survey plane. Too far downstream and the steady-state assumption becomes invalid as the wake is still evolving (and the potential jump across the wake sheet would be changing in time). This would suggest placing the plane close to the wing trailing edge; however the singular nature of the vortex filaments creates numerical issues should one of the nodes of the survey plane lie very close to a filament. Indeed a special treatment for evaluating the induced velocities very near a filament can be implemented such as ignoring the contribution entirely or supposing a vortex core diameter that undergoes solid body rotation, however this was not done here. In order to demonstrate this issue, with the $AR = 2$ wing set to $\alpha = 15^\circ$ the wake survey plane was started at the trailing edge and moved downstream in steps of $0.01c$ until it was clear of the wake altogether. The drag integral was computed using the double trapezium rule. The plane itself was extended $1.5c$ either side of the wing tips and $2.25c$ and $2.75c$ above and below the leading edge (with the wing being rotated about the leading edge). This resulted in a square grid which was discretised into 200×200 elements (giving a resolution of $0.025c$)

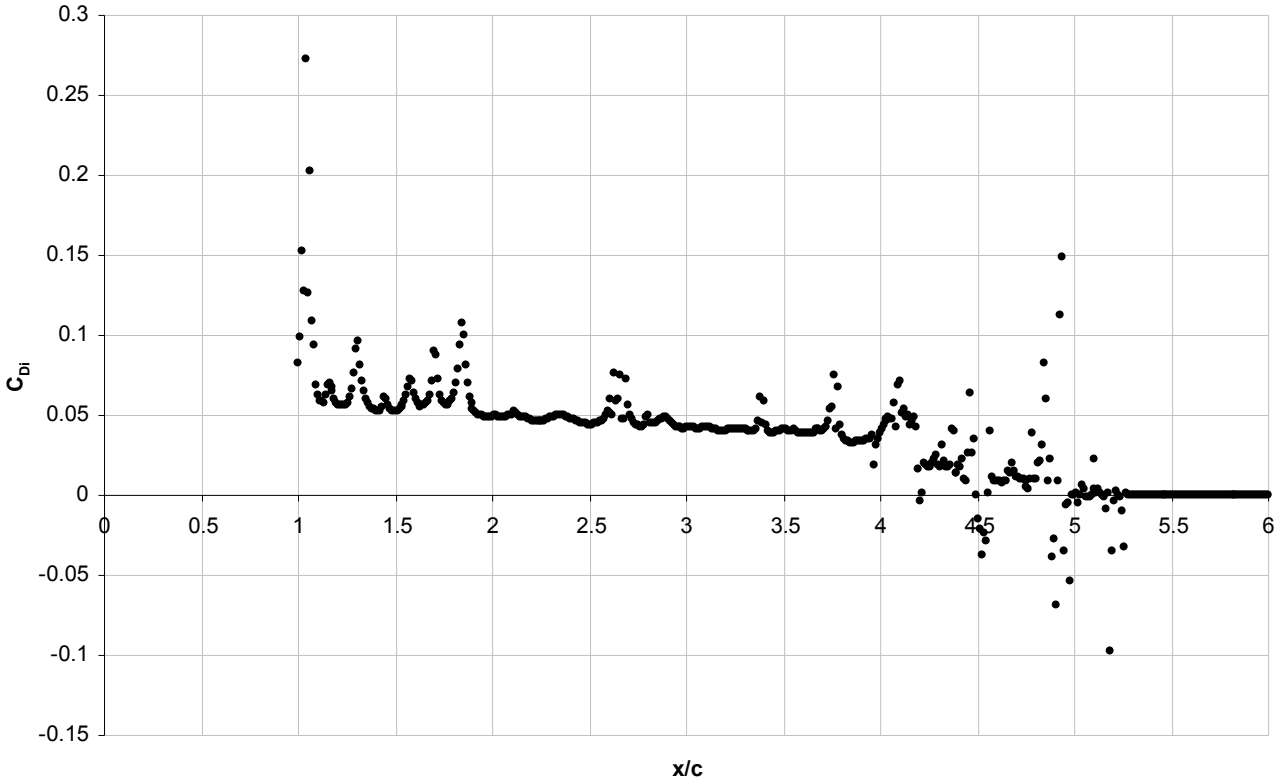


Figure 27: Induced drag coefficient computed from a wake survey at various downstream positions

There appears to be a steady region between $x/c = 1.95\dots 2.4$. Further downstream a negative trend sets in due to the unsteadiness in the developing wake, with some spurious negative drag values in the vicinity of the starting vortex. Further upstream the drag value is very sensitive to the plane location, although the local minima fall close to the values in the steady region. It is expected that the steady region grows larger with time as the wake is further established and the starting vortex becomes relatively further away. Indeed this issue of “noisy” drag calculations due to the singular nature of the vortex filaments making up the wake sheet renders the wake survey method somewhat unattractive compared to the more direct method of surface force computation. Based on the above graph the wake survey for each angle of attack was stationed at $x/c = 2$ and the images below show the result for each angle of attack. The data are coloured by the integrand of the integral equation (35) expressed in coefficient form, with blue denoting zero and red anything greater than or equal to 0.02. Note the artefacts that appear in close proximity to the filaments. This is a similar phenomenon to the wiggles observed in the velocity profile near the body surface panels and is due to the low order nature of the vortex filament (i.e. constant strength doublet) panelling.

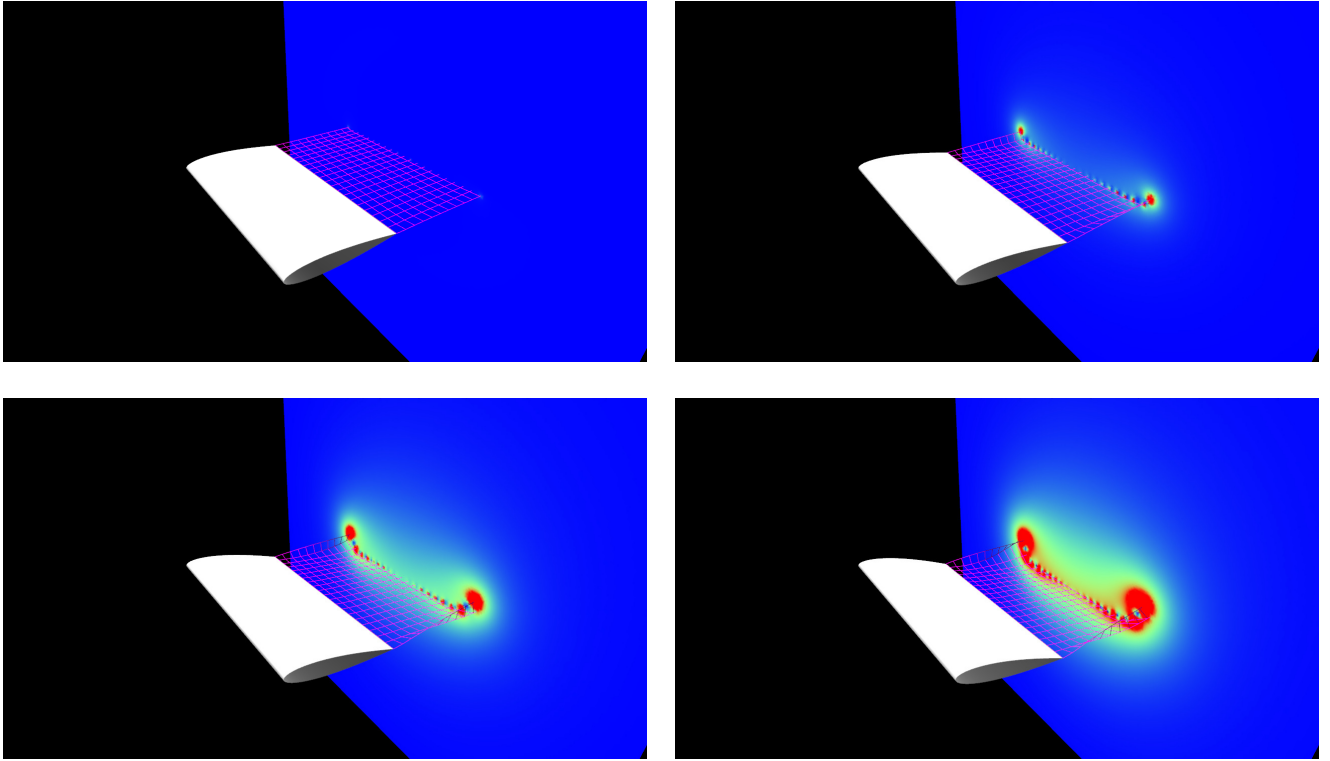


Figure 28: Wave survey revealing contributions to induced drag for $\alpha = 0, 5, 10, 15^\circ$ respectively

One interesting feature of the wake survey is that it provides information regarding what flow features are responsible for contributing the largest amount towards the induced drag. The results clearly indicate that the tip vortices are the largest contributor, followed more generally by the region of fluid in proximity to the wake sheet (which extends beyond the extent of the wing itself), with a greater emphasis on the suction side of the wing. This can be explained by the fact that the tip vortex is primarily an in-plane swirl flow and therefore has a deficit of streamwise momentum. In addition, the fast swirling flow nearer the core has reduced pressure which further contributes to the drag (c.f. the sign of the second (pressure) term in the integrand of equation (35)). The induced downwash caused by the wake sheet rotates the flow away from the streamwise direction, thereby creating streamwise momentum deficit.

The graph below presents the results of the wake survey alongside those of the surface force computations for induced drag. This time the theoretical ideal induced drag coefficient (equation (37)) is evaluated using the actual computed lift coefficient rather than the theoretical lift coefficient. Additional angles of attack were evaluated to ascertain the results of the wake survey for small angles of attack

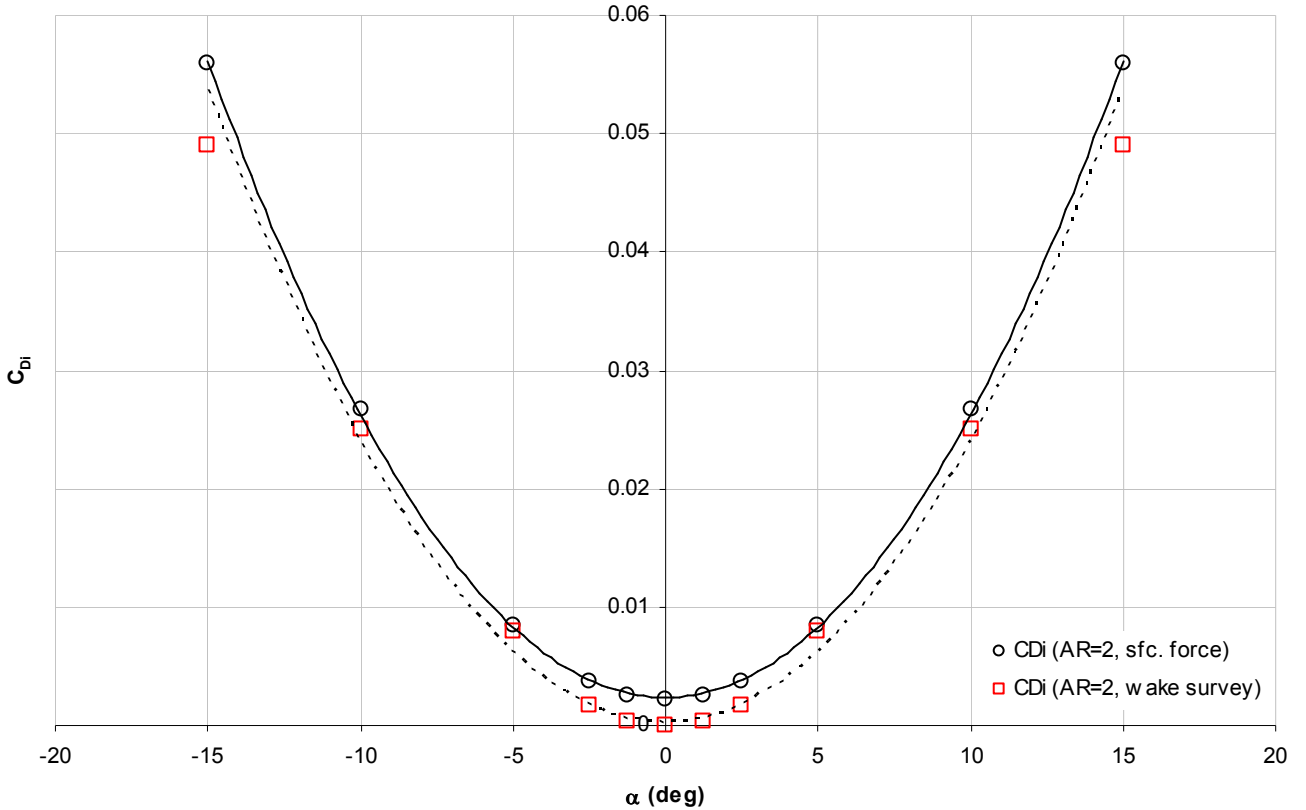


Figure 29: Comparison of induced drag obtained from surface forces, wake survey and theoretical result

The wake survey results compare well with the results obtained from the surface forces, except perhaps the largest angle where there is about 12% discrepancy. However for the smaller angles the wake survey actually gives results that lie almost exactly on the theoretical line and, importantly, correctly predict zero drag at zero incidence (unlike the surface force computation). Thus one may conclude that the wake survey is best used for small angles of attack such as $|\alpha| < 3^\circ$. It is also worth pointing out the good agreement of the results with the theory when the actual lift coefficient is used in the induced drag equation (37) rather than the theoretical result.

The theoretical results supposed a unity spanwise (Oswald) efficiency factor. This applies only to the case of an elliptic circulation distribution in the lifting line theory. For the computational wing, the circulation is distributed over all the panels rather than on a single line. It is possible to examine the circulation distribution on the wing at some fixed chordwise distance from the leading edge. Alternatively one may sample the maximum and minimum circulation values at each spanwise station. The latter results are shown below for each of the aspect ratios with the wing set at $\alpha = 10^\circ$

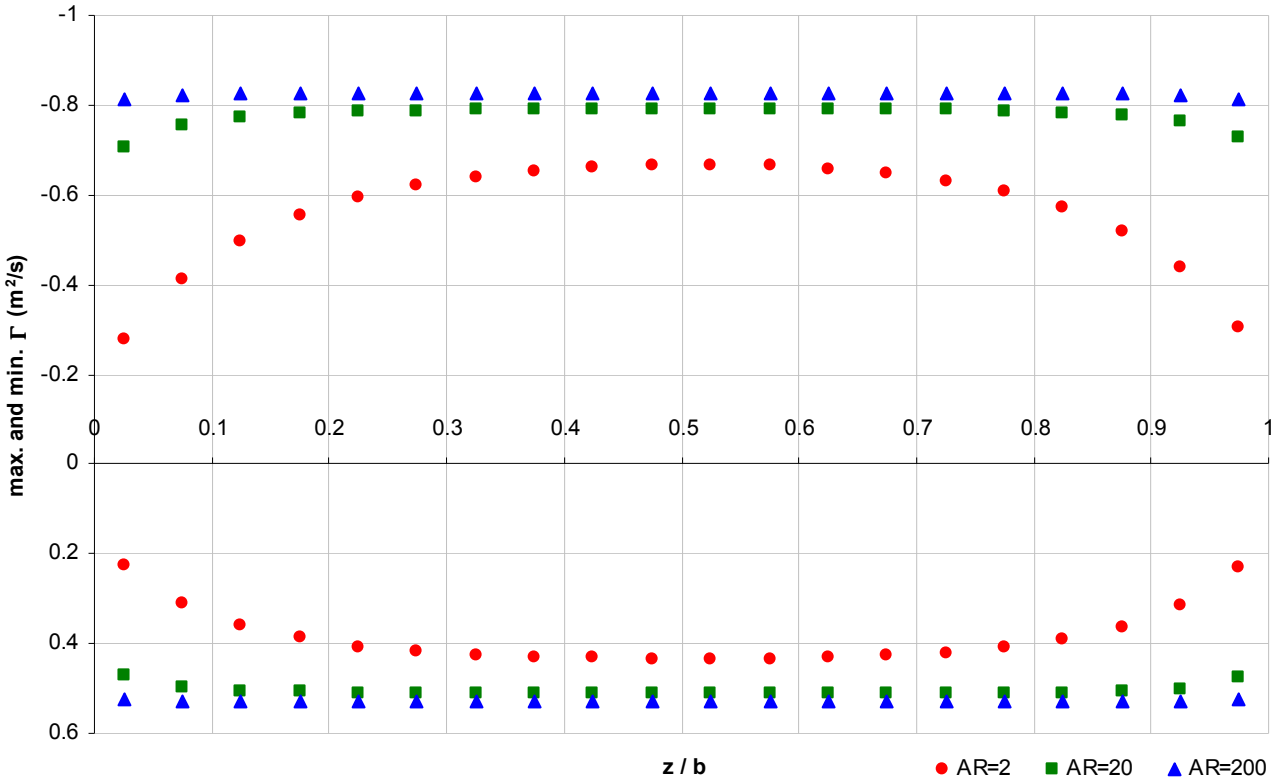


Figure 30: Spanwise variation of peak circulation showing the effect of aspect ratio. Wing fixed at $\alpha = 10^\circ$

As the aspect ratio is increased, the peak spanwise circulation distribution asymptotically tends to a linear shape as well as a higher magnitude. Interestingly the smallest aspect ratio case has a distribution that is closer to the ideal elliptic shape than the higher aspect ratio wings. Thus the Oswald efficiency factor is actually closer to unity for smaller aspect ratio wings, despite their poorer performance with respect to both lift and induced drag. In fact for the $AR = 2$ wing the Oswald efficiency factor was also a function of the angle of attack, with the distribution becoming more linear as the angle of attack decreased. Once again this reveals a deficiency in the linearised theory since for large angles of attack there is a non-linear feedback from the wake onto the body that alters the spanwise circulation distribution. The non-linear phenomenon of wake rollup and self-advection is therefore an essential feature to model when dealing with large angles of attack. For the data presented above, an estimate of the efficiency factor found by solving the induced drag equation (37) for e was 0.925.

Test case 3: Uniformly Translating Wing with Superimposed Oscillations

The sub-cases in this section highlight some results for basic unsteady motions involving separate heave, roll, and surge oscillations superimposed on a wing with $AR = 2$ uniformly translating in the x -direction (the streamwise direction) with unity non-dimensional velocity.

Heave Oscillations

The heave velocity amplitude was selected such that the largest absolute instantaneous angle of attack did not ever exceed 15° . A non-dimensional period of 0.5 was selected such that sufficient wake panels represent each period of motion. The resulting wake after six periods is shown below

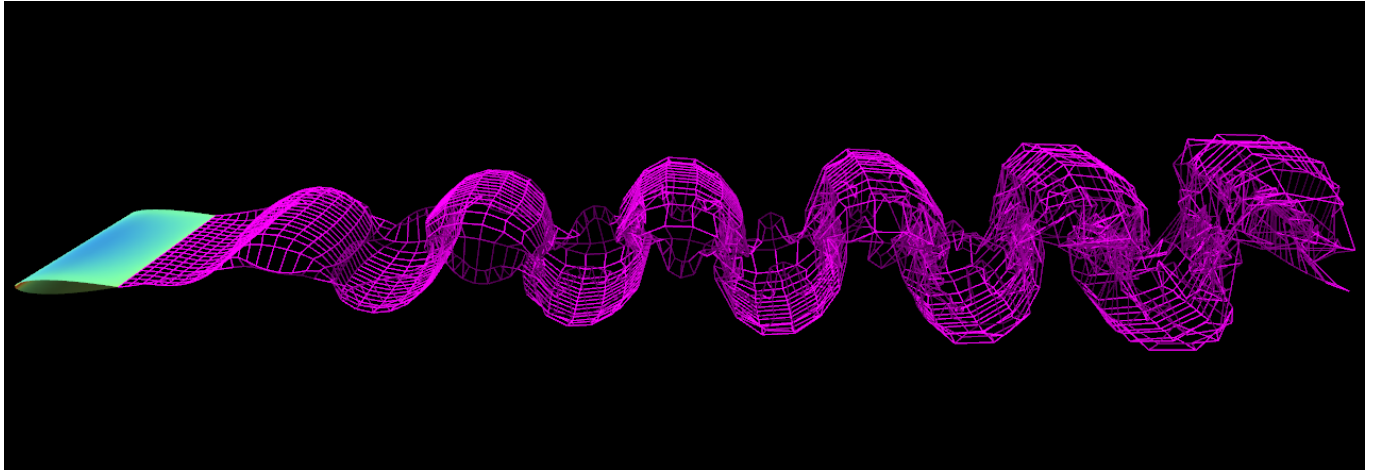


Figure 31: Wake shed by a wing undergoing symmetric heave oscillations

The result is similar to the 2D case (c.f. Nathan 2011) but now with the additional 3D effect of rollup occurring along the wake free edges from the wing tips. The time history of force coefficients in Cartesian components is shown below. It is more informative to consider the forces aligned with the fixed reference system of the world than the usual lift and drag coefficients whose direction changes as the incident flow angle changes with the wing motion. Thus lift and drag are here taken to mean perpendicular and parallel to the negated translation direction vector of the wing.

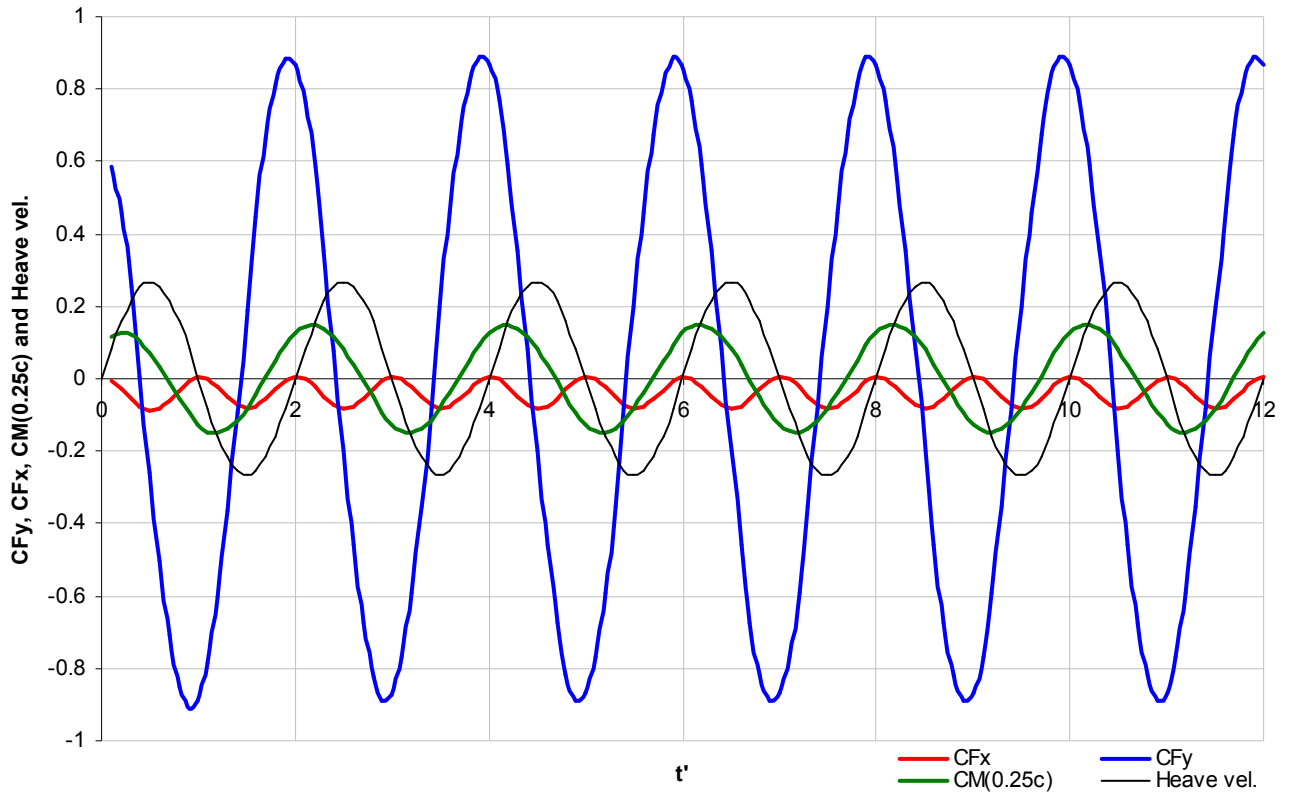


Figure 32: Time history of force coefficients for a uniformly translating wing undergoing symmetric heave oscillations

The force in the streamwise direction is always negative indicating that symmetric heave oscillations in combination with uniform streamwise translation can be used to generate thrust. The peak thrust is in phase with the negated heave oscillations while the lift force lags the negated heave oscillations by 75° and the moment coefficient lags the negated heave oscillations by 120° . On average there is no net lift force. It should also be noted how the forces almost completely establish their steady limit-cycle within the first period.

Roll Oscillations

A motion only possible in 3D, this sub-case involves periodically rolling the wing about its centre station using the same driving velocity as the previous case of symmetric heave oscillations (the current geometry means that the wing tips will attain the maximum absolute angle of attack of 15°). The resulting wake after six periods is shown below

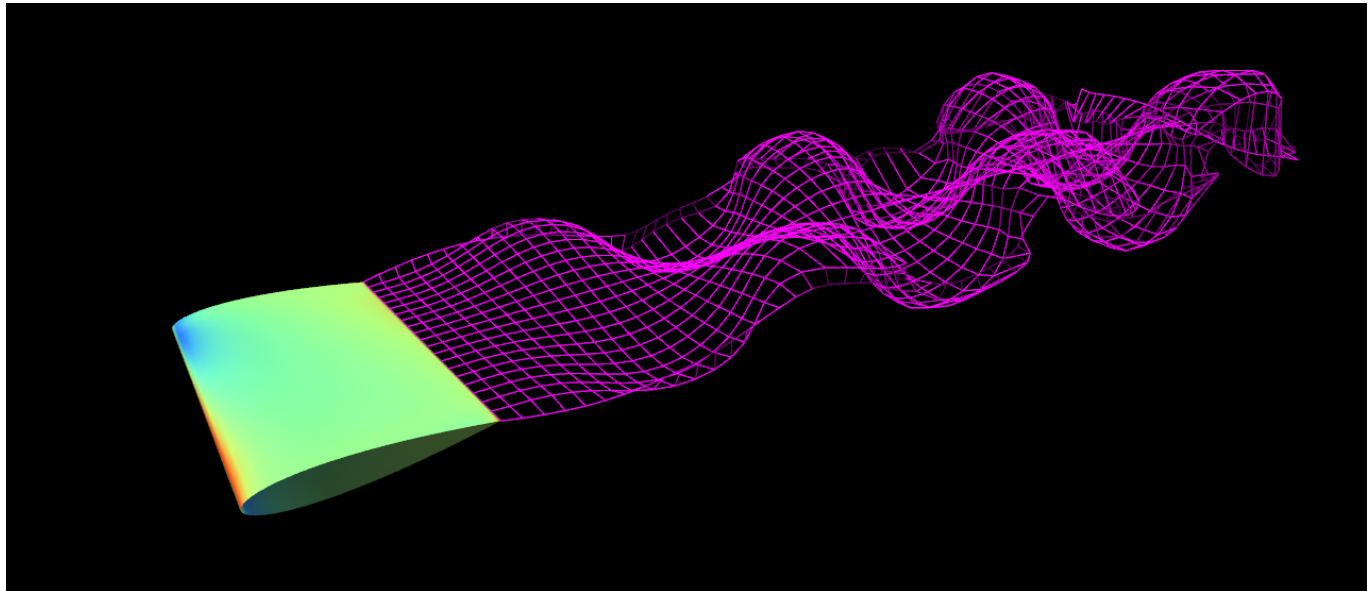


Figure 33: Wake shed by a wing undergoing symmetric roll oscillations

The result bears a resemblance to the heave motions in the sense that the wake could be seen to comprise the wake of the heave motion either side of the centre station, with one side shifted out of spatial phase relative to the other. Observe also the asymmetry of the pressure distribution at the instant this image was taken while the wing was rolling clockwise looking into the direction of motion. The far side is generating lift while the nearside is generating downforce. The time history of the forces is shown below

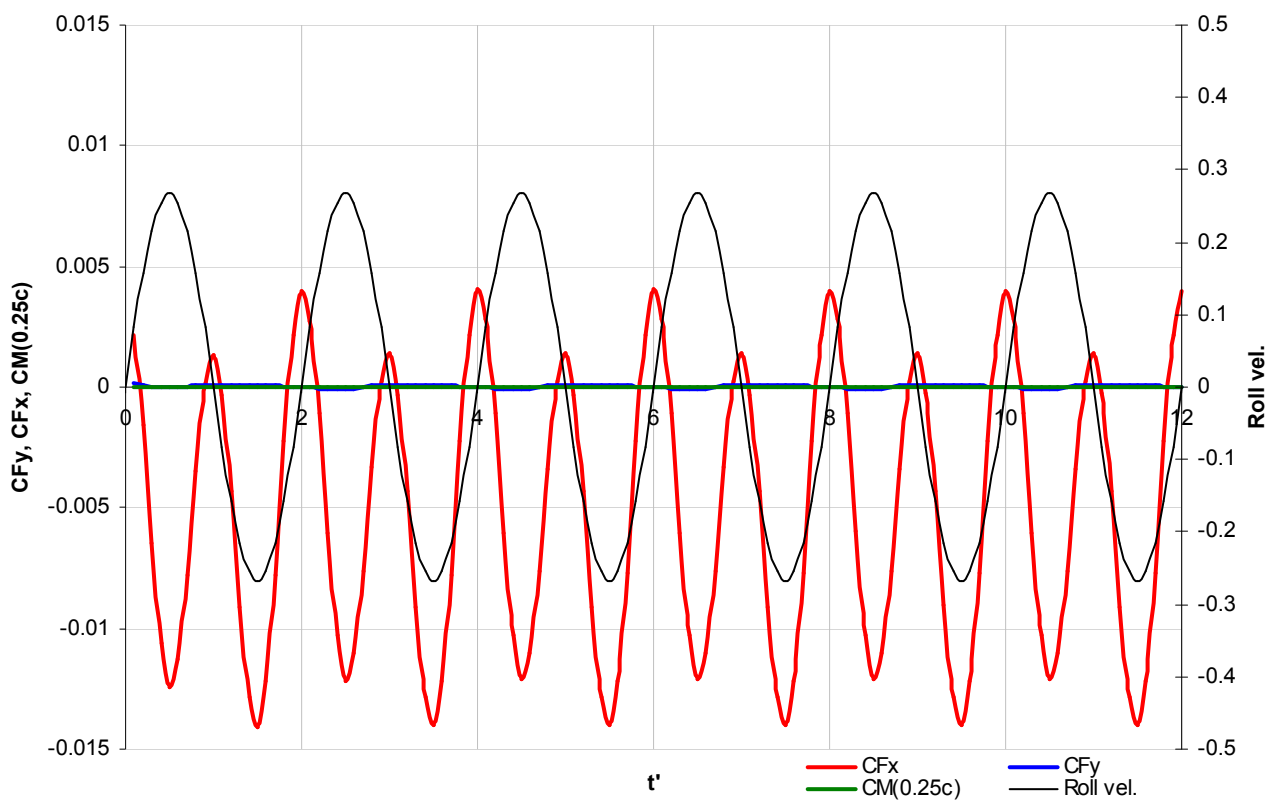


Figure 34: Time history of force coefficients for a uniformly translating wing undergoing symmetric roll oscillations

Symmetric roll oscillations in combination with uniform streamwise translation can also be used to generate thrust, but now without any oscillations in lift force. Although advantageous from a structural and/or ride comfort point of view, the thrust generated in this case is about 6.3x less than that generated by the symmetric heave oscillations. The comparison is fair since both oscillations had the same driver function. This case opens up some interesting possibilities regarding wings given a roll oscillation while translating. A system can be envisioned whereby the wing may be twisted in time such that the angle of incidence is set to the optimum value along the entire span for a given roll angle. Of course, this is essentially what an optimised propeller does, but rather than having time-varying twist, the twist is fixed and the blades undergo continuous rotation rather than oscillation. One could also go on to consider flapping wings and the optimisation of the driving cycle for the combination of roll, pitch and yaw cycles.

Surge Oscillations

This motion involves oscillations in the streamwise translation of the $AR = 2$ wing. The driving function was set such that the wing undergoes repeated start-stop motions. The wing was set at $\alpha = 15^\circ$. The resulting wake after six periods is shown below

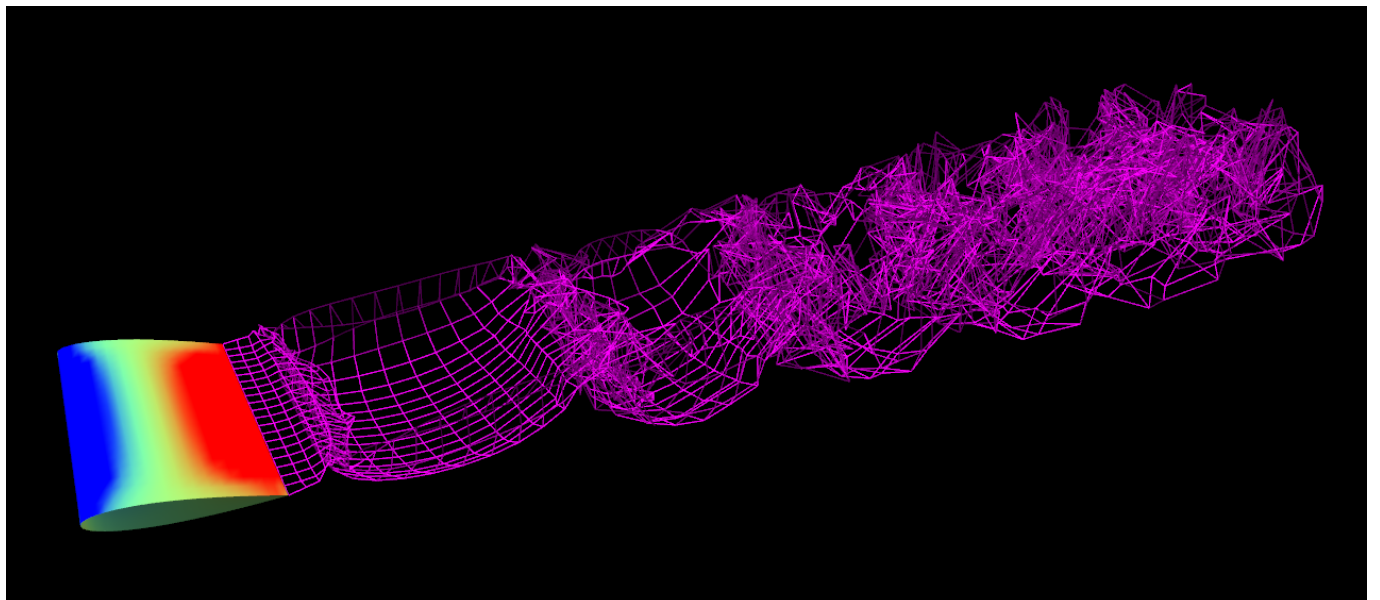


Figure 35: Wake shed by a wing undergoing repeated start-stop motions

A large region of stagnation can be seen at the trailing edge during the forward acceleration stage of the motion. The unsteady term in the pressure coefficient equation is a significant contributor in this kind of motion. The time history of the forces is shown below

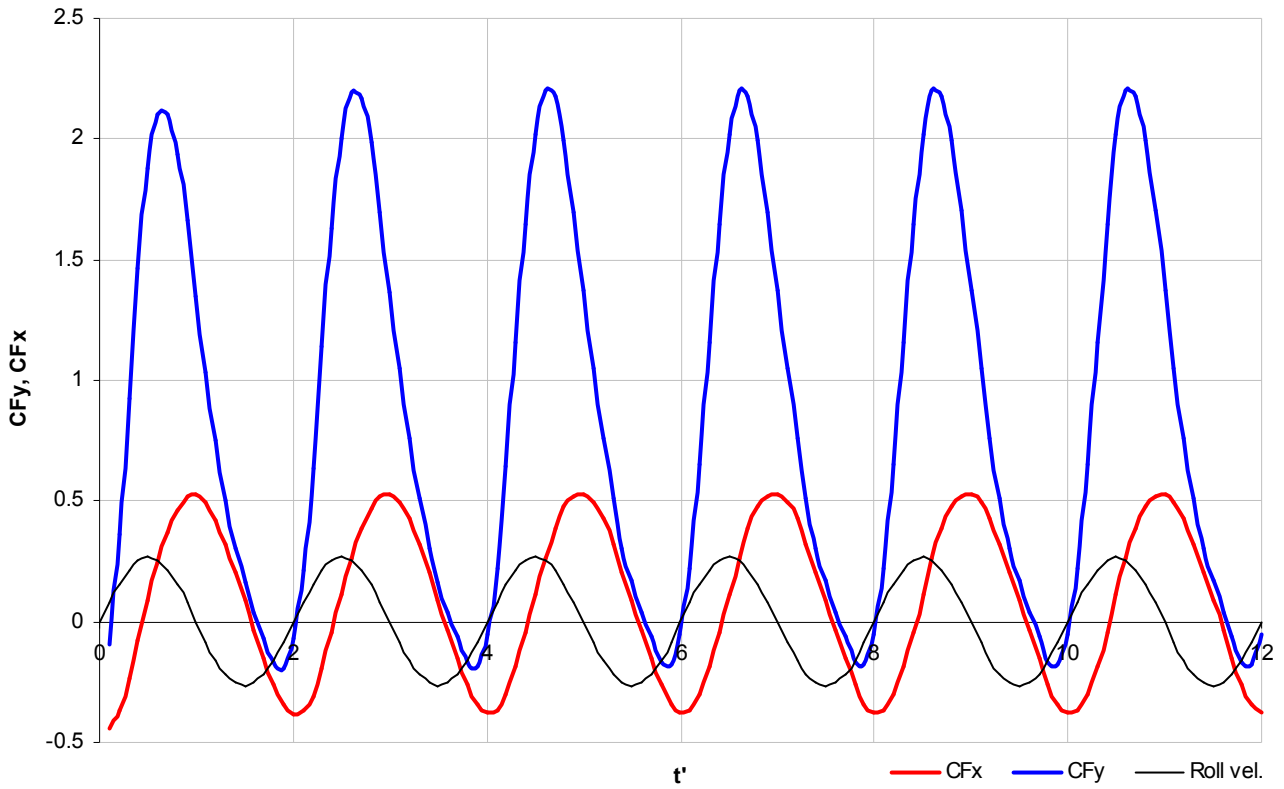


Figure 36: Time history of force coefficients for a uniformly translating wing undergoing repeated start-stop motions with $\alpha = 15^\circ$

On average the start-stop motions produce relatively large amounts of net lift as well as a positive drag. The best L/D ratio at any instant is about 17, and at peak lift it is 8.33. Compared to the case of simple uniform translation with $\alpha = 15^\circ$ this motion produces, on average, 1.5x the drag and also 1.5x the lift. Thus, at least for low aspect ratio wings, the same L/D ratio is achieved either by uniform translation at fixed angle or start-stop motions at fixed angle. However the start-stop motion has the potential advantage of generating 1.5x the lift.

The other motions involving yaw and pitch can be summarised by thought experiment. Yaw oscillations during uniform translation would result in the creation of a roll moment (except at zero-lift angle of incidence). This is due to the spanwise gradient of the lift force caused by the change in incident flow speed along the span. Any spanwise gradient of force (taken with respect to the centre of gravity for a free body) will produce a force couple about the axis perpendicular to the direction of the force gradient – in this case the streamwise axis, thereby leading to a roll torque. This is why some model aircraft do not have ailerons for roll, since rolling motion can be attained as a secondary effect of yaw. Oscillations in pitch would give *qualitatively* similar results to heave oscillations as the action of pitch is to change the angle of incidence, in the same manner as a heave velocity changes the angle of incidence of the oncoming flow.

Test case 4: Simulation of a Propeller

This test case is in fact the reason for the creation of this code, the objective being to validate the author's proprietary design algorithm for propellers of constant spanwise circulation (as opposed to the Goldstein circulation distribution, or Prandtl's more practically applicable approximation to it). The constant spanwise circulation propeller was proposed by Struve (1943). Comparison of the predicted geometry of the propeller using constant spanwise circulation with that using the Prandtl circulation function revealed that the chord and twist distributions were very similar for low advance ratios, with the most difference being near the root of the blade. However since the root does little in terms of thrust generation, the predicted thrust was also very similar for both methods. The Prandtl circulation function propeller gave a slightly higher thrust, and this is to be expected since it is a well known classical result by calculus of variations that the optimum propeller is one which generates a helicoidal vortex wake sheet of constant pitch. The design algorithm is based on a combination of blade element theory with an axial momentum balance. It does not consider the effects of wake edge rollup (highly non-linear), wake contraction or wake rotation. Since the use of the momentum theorem implies a steady state, the design algorithm is effectively treating the propeller as an actuator disc across which there is a jump in total energy. This is similar to supposing an infinite number of infinitesimal blades that do not interfere with each other. By simulating the propeller in the present flow code where the wake is allowed to develop naturally, the errors incurred by these simplifying approximations can be quantified and used as correction factors in the thrust and torque predicted by the design algorithm. If the errors are severe, then a better algorithm is required altogether!

A two-bladed, low advance ratio ($J = 0.15$) propeller of tip-radius 0.13m was designed to match the shaft power output and rpm of a direct-drive 8200rpm 80W brushless DC electric motor used in model aircraft. This test case uses all features of the code by mixing two lifting bodies (the two propeller blades) with a non-lifting body (the spinner). The following images show the propeller wake after about 15 rotations. It should be noted that the simulation time for only 15 rotations was just under 19hrs on a single-core AMD Phenom X2 running at 3.5GHz. The time step was chosen such that there were 50 time steps per revolution, as this was deemed sufficient to give a decent spatial resolution of the wake sheet.

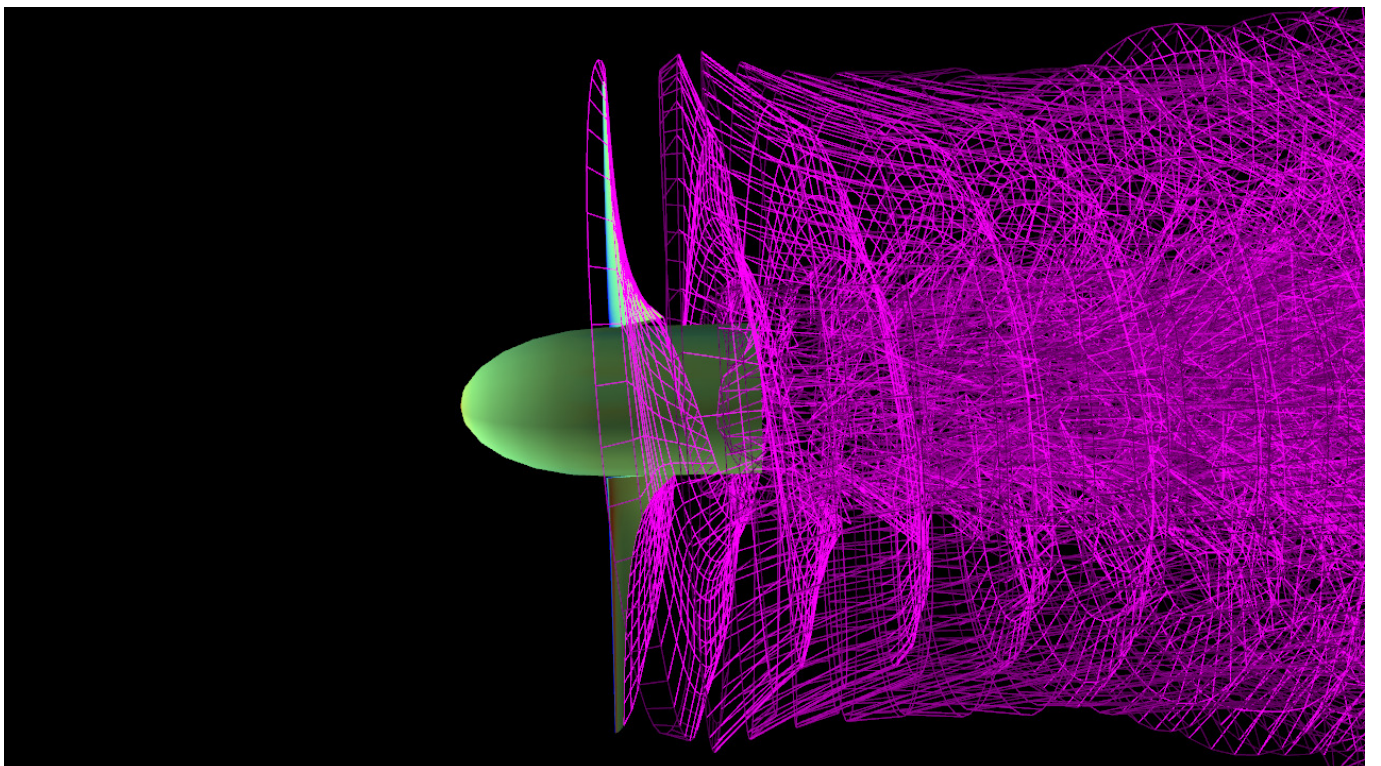


Figure 37: Side view of the propeller and wake

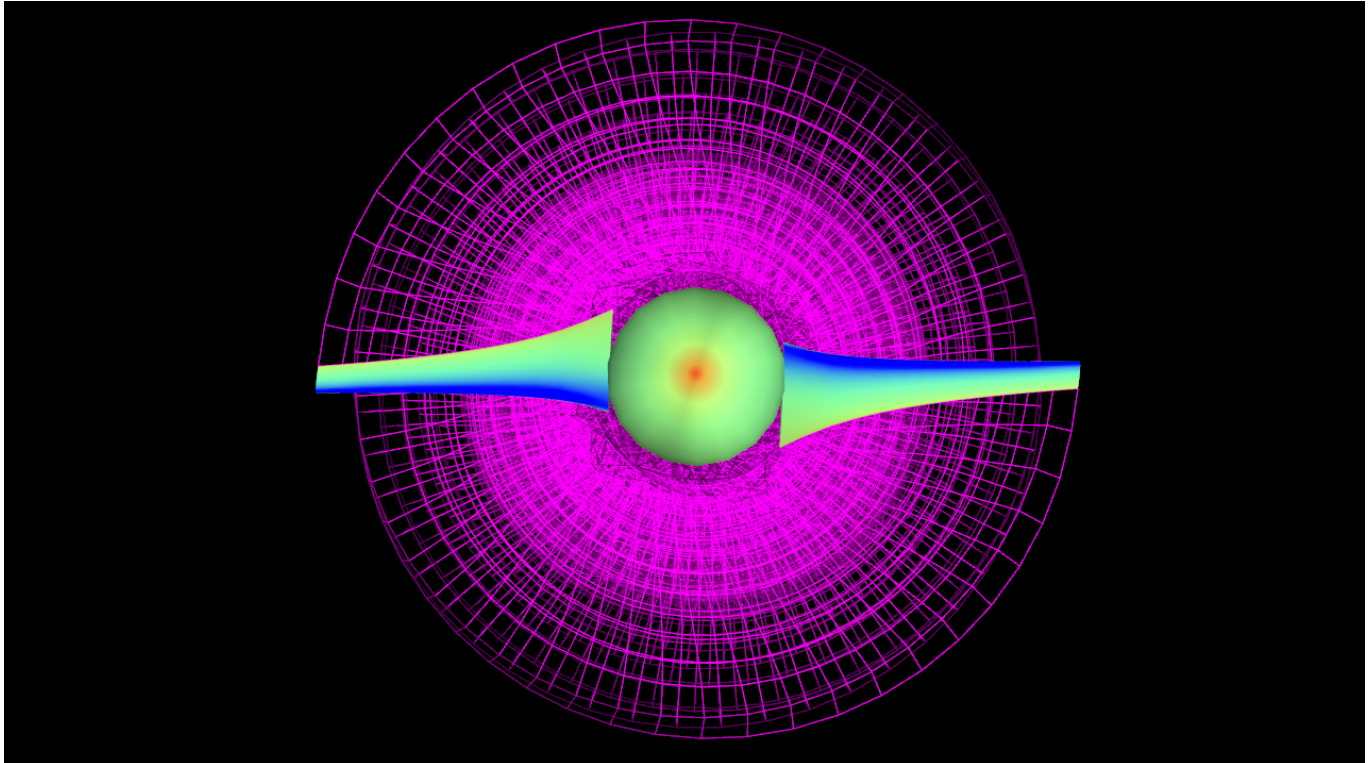


Figure 38: Front view of the propeller and wake

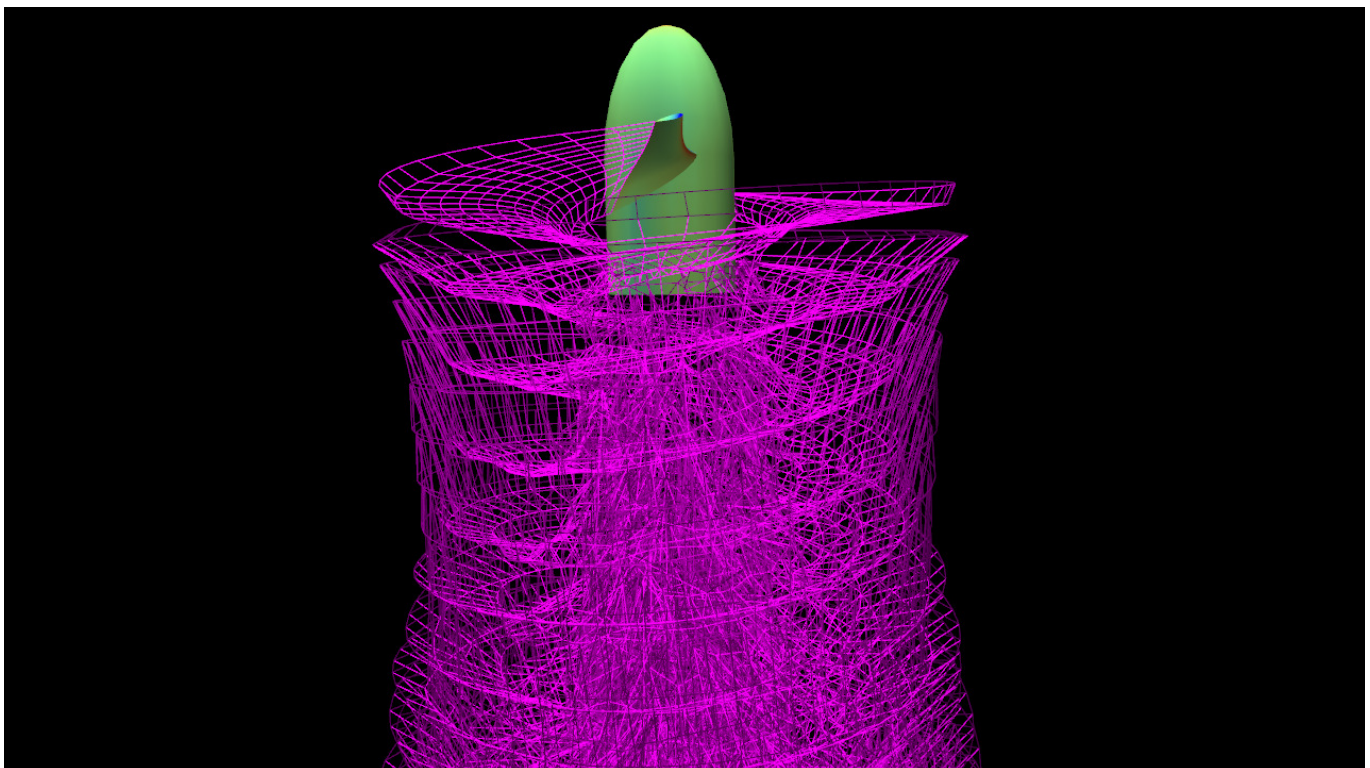


Figure 39: Another side view of the propeller and wake

The helicoidal wake sheet is clearly visible. It is also evident that wake rollup and distortion at the blade tips and root is quite a significant feature of the solution. The surface forces acting on the blades are shown below

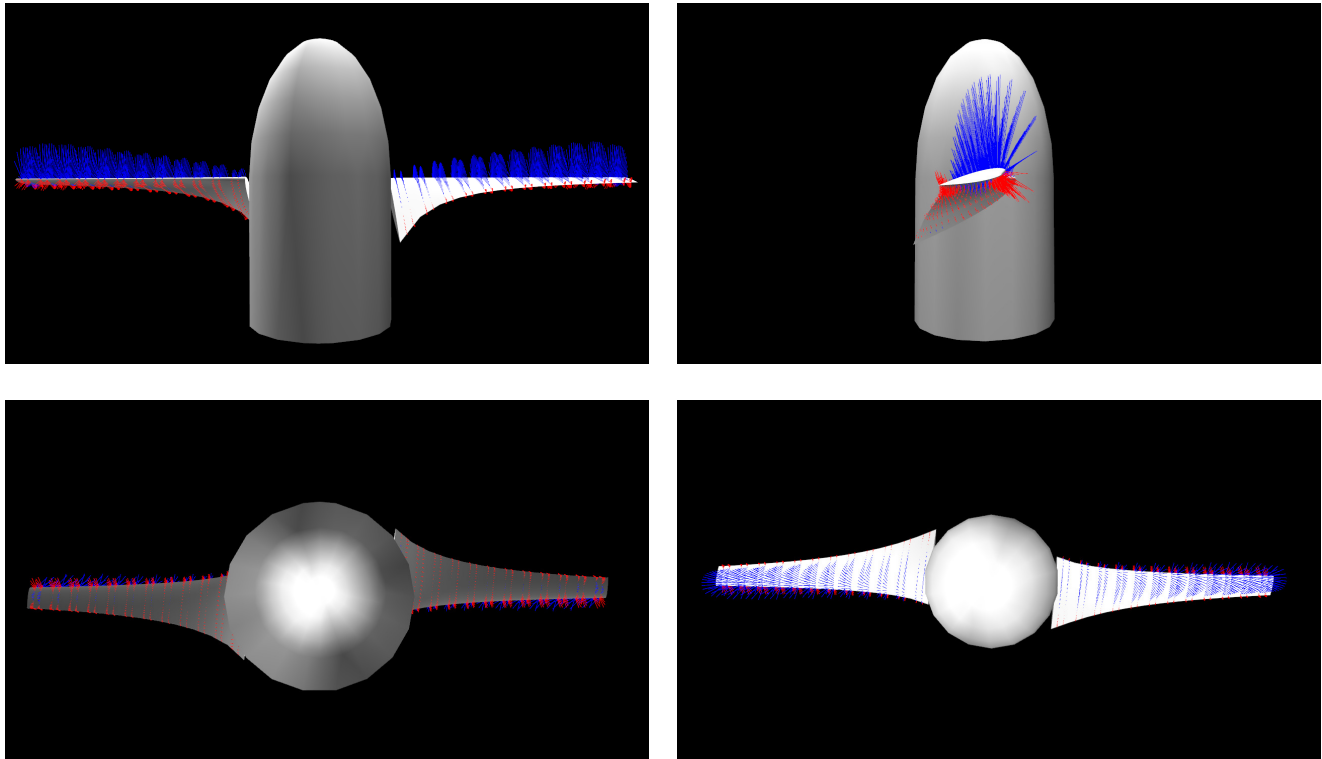


Figure 40: Forces acting on the propeller blades. Top row – two side views; bottom row – underside and topside view

As expected for a propeller generating thrust, there is suction on the upstream-facing side and overpressure on the downstream-facing side. The comparison between the thrust and shaft torque predicted by the design algorithm and that obtained from this simulation is shown below

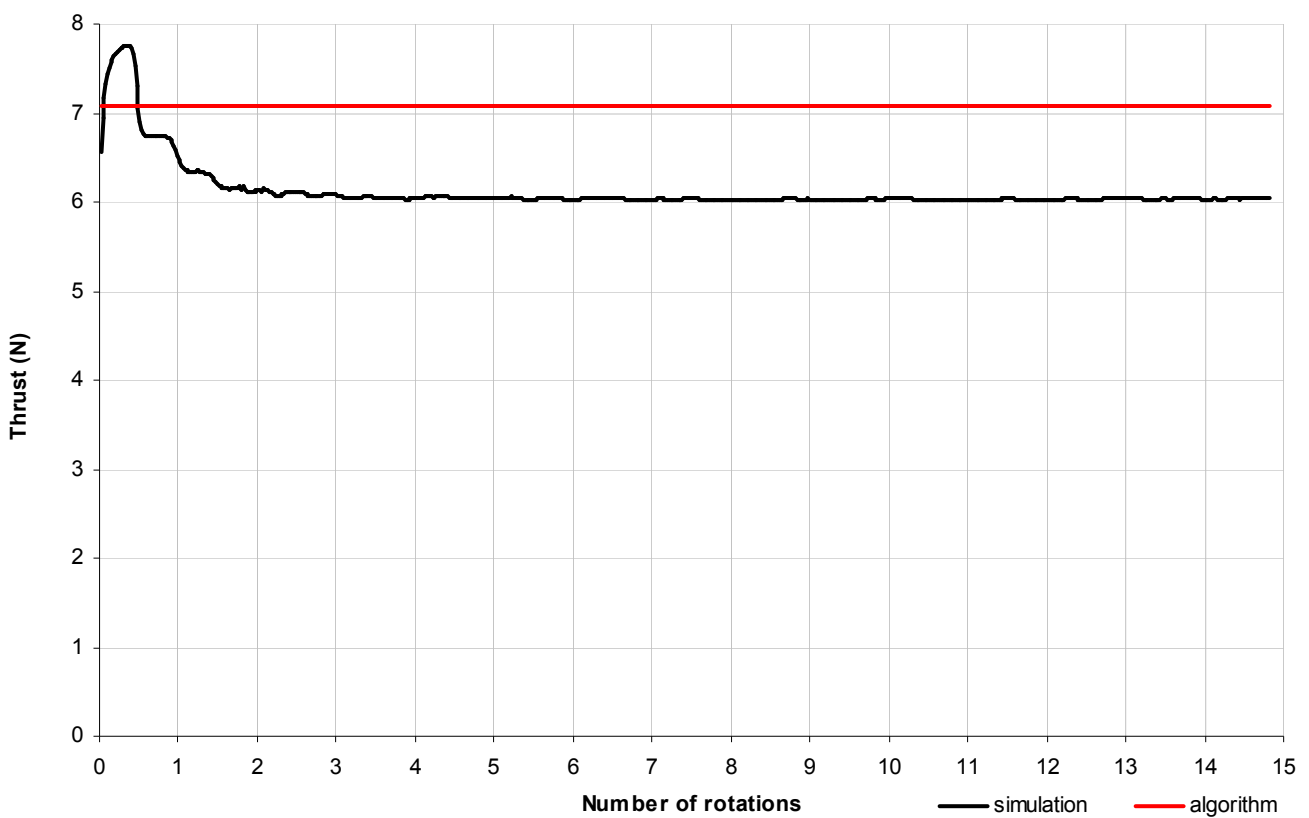


Figure 41: Comparison between thrust from design algorithm and simulation

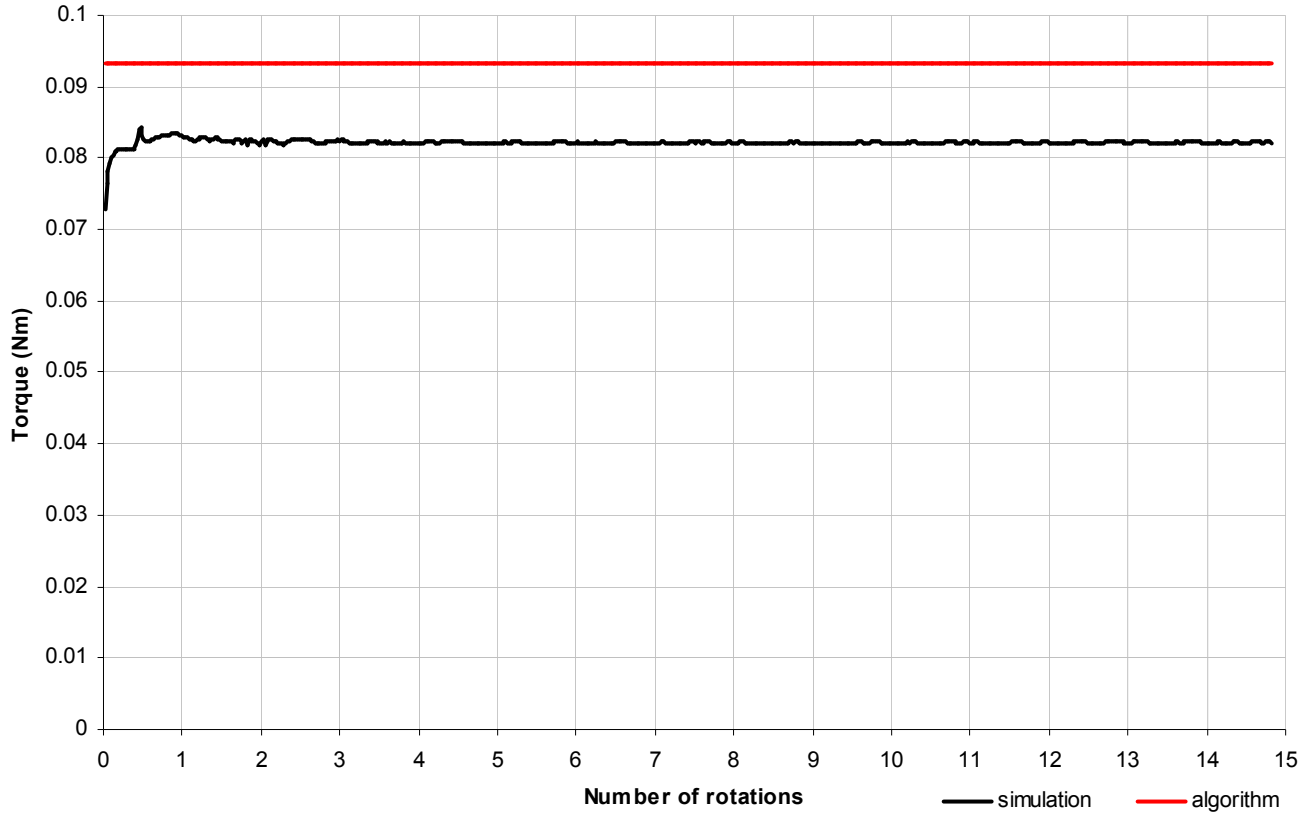


Figure 42: Comparison between shaft torque from design algorithm and simulation

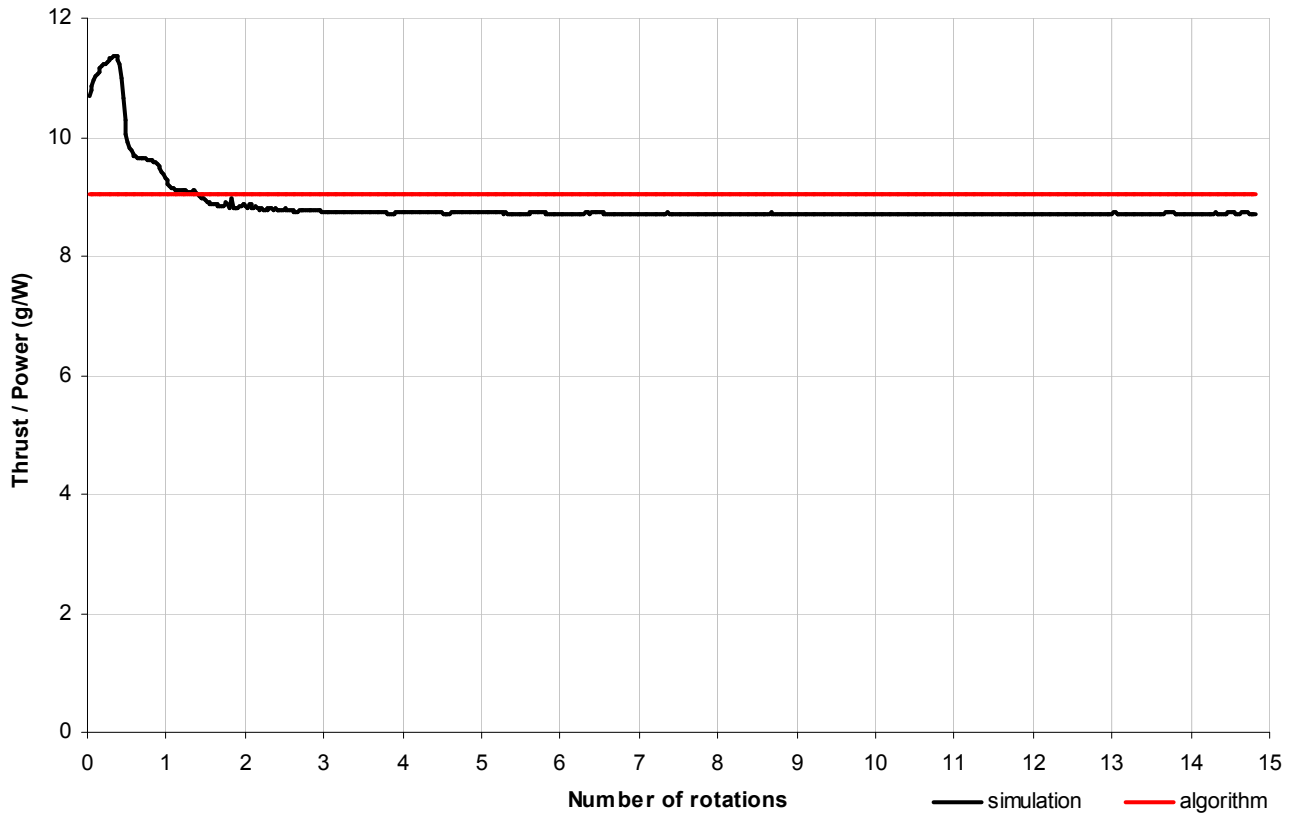


Figure 43: Comparison between thrust/power ratio from design algorithm and simulation

Steady-state values are established within just four rotations of the propeller, and it is interesting to observe the discrete nature in which the thrust steps down to its steady value. The steps occur every half revolution and are caused by the propeller blade interacting with the starting vortex of the other propeller blade. Once the starting vortices are washed downstream, this effect disappears. The exceptional gain in

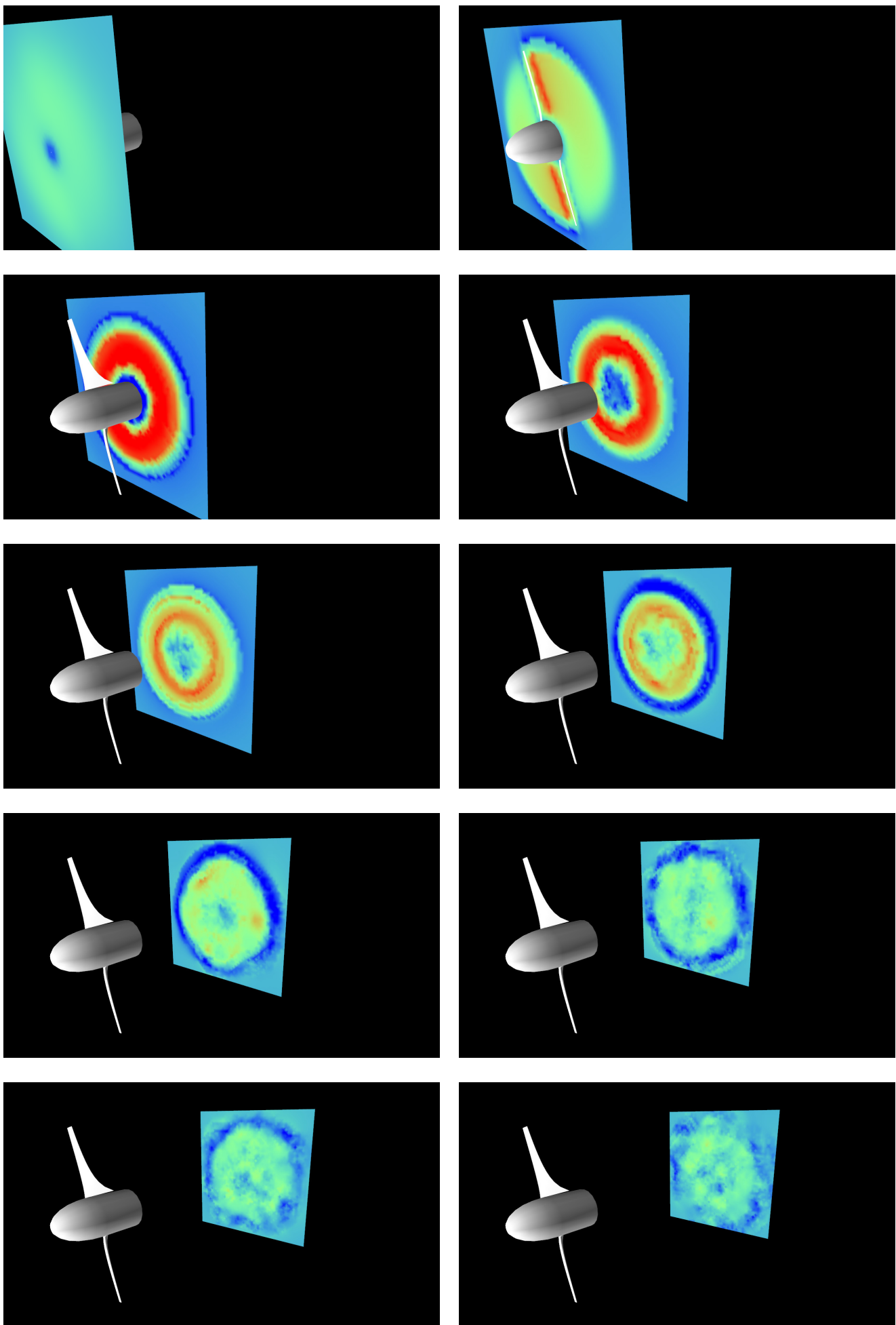
thrust caused by this phenomenon (notably without gain in shaft torque) is food for thought as to whether this could be reproduced for all time using some kind of flow control.

The relative errors in the algorithm are somewhat disappointing and can be summarised as follows:

- Thrust 17.4%
- Torque 13.4%
- Thrust/Power 3.6%

It should be noted that a separate simulation to test the effect of the presence of the spinner (which is not modelled in the design algorithm) revealed that it does not alter the thrust but causes a few percent increase in the shaft torque. This is due to the way the spinner modifies the root vortex flow and its induced velocity on the blade roots.

The question regarding the sources of these errors must now be asked. It is informative to inspect the axial velocity development throughout the entire solution, starting upstream and finishing past the wake. This is done using measurement planes in the same manner as the wake survey drag calculation, only this time the planes are coloured by the axial component of the velocity vector. Here, red denotes $U \geq 9.5 \text{ m/s}$ and blue denotes $U \leq -2.5 \text{ m/s}$. The measurement plane begins at the spinner tip and advances in steps of 60mm in the downstream direction. The plane contains 50x50 elements giving 6.24mm spatial resolution. The plane extends 20% beyond the diameter of the propeller disc.



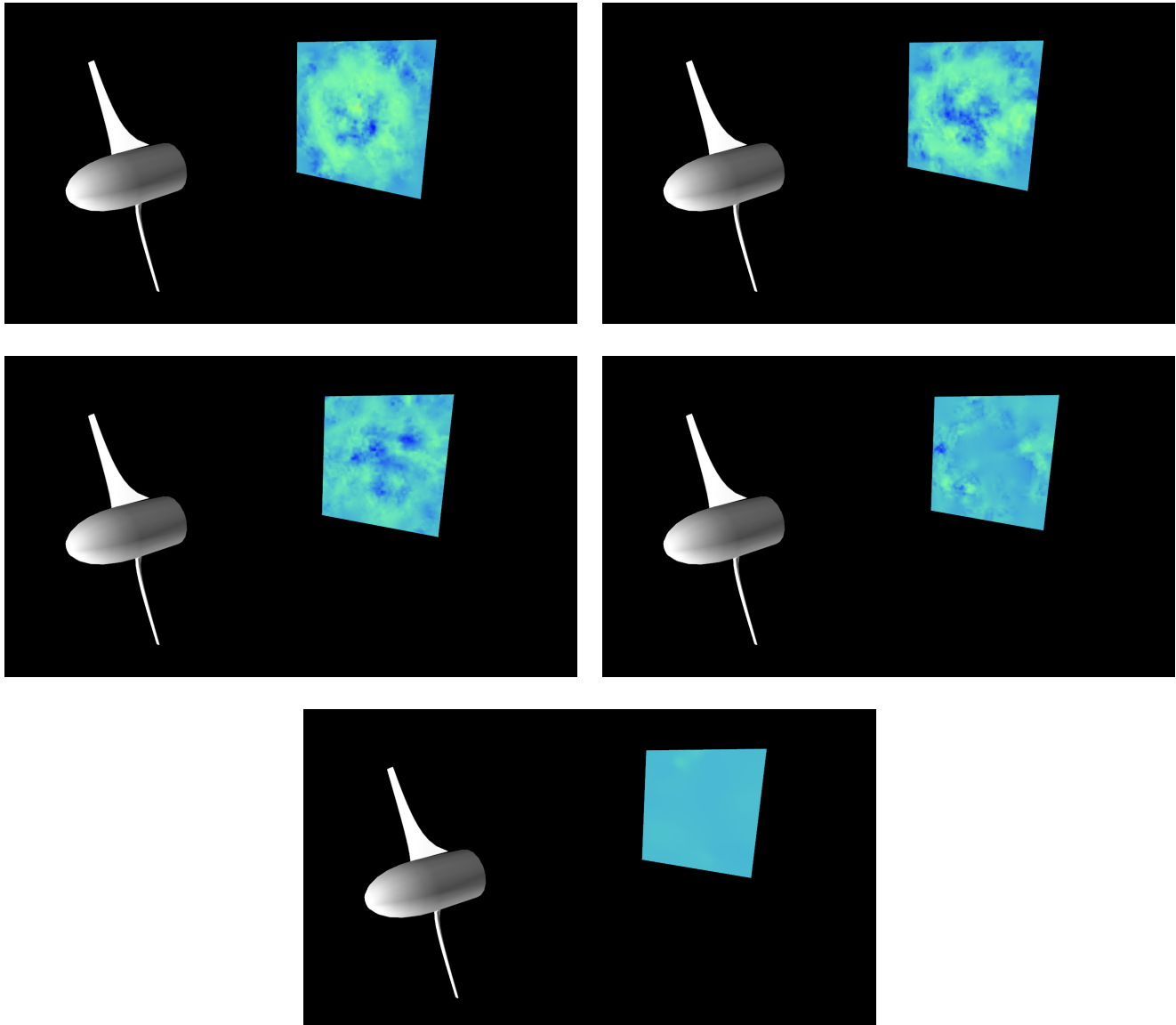


Figure 44: Axial velocity component measured in successive cross-stream planes in steps of 60mm

The very first image reveals how the helicoidal wake sheet already induces an axial flow upstream of the propeller station. This naturally affects the incident flow on the propeller blades and is taken into account in the blade element theory (known as the axial interference velocity). The second image shows the flow around the propeller blades, highlighting the speed (and therefore, after Bernoulli, the pressure) differential between the upper and lower surfaces. As the planes continue to move downstream, the axial flow field evolves into a core of weakly reversed flow surrounded by a torus of strongly positive flow itself surrounded by a thin sheath of weakly reversed flow. The inner core and outer sheath then “diffuse” into the torus of positive flow. This process continues until the torus of positive flow weakens to the point of being indistinguishable. The outer sheath of reversed flow also reappears for a while. The wake sheet becomes highly entangled towards the starting location eventually losing its coherency.

The axial velocity field immediately behind the propeller is quite different from that predicted by the algorithm. The graph below shows what was expected from the algorithm

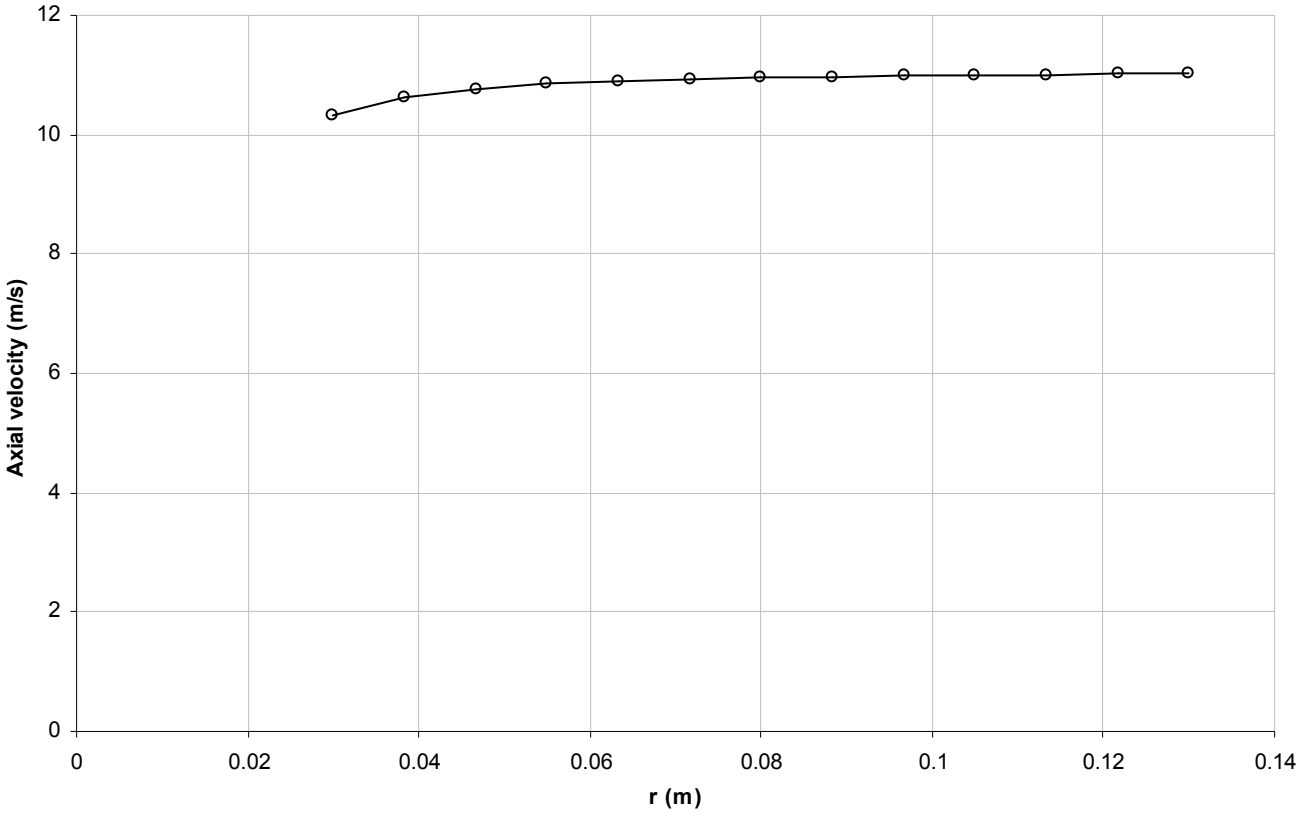


Figure 45: Axial velocity profile at propeller station predicted by the design algorithm

There is no indication of a reversed flow towards the root, although the velocity does begin to fall off. Importantly, there is no indication of speed decay towards the tip. Thus it is now clear that blade tip effects, which were not modelled at all in the design algorithm, are actually very important. This is perhaps obvious given the results of the previous sections for finite wings. In order to test this hypothesis that blade tip effects are a key reason for the discrepancies in thrust and torque, a cylindrical shroud can be constructed and placed around the propeller, extending some distance upstream and downstream. By continuity this would also have the effect of preventing wake contraction. For the present case a duct with 5% tip clearance was placed around the propeller, extending 60mm upstream of the propeller station and 500mm downstream. In order to speed up the computation, a higher advance ratio propeller ($J = 2$) of smaller tip radius 62mm was designed for this test. The same propeller was also simulated in isolated conditions to enable meaningful comparison and conclusions to be drawn. Snapshots from the simulations are presented below

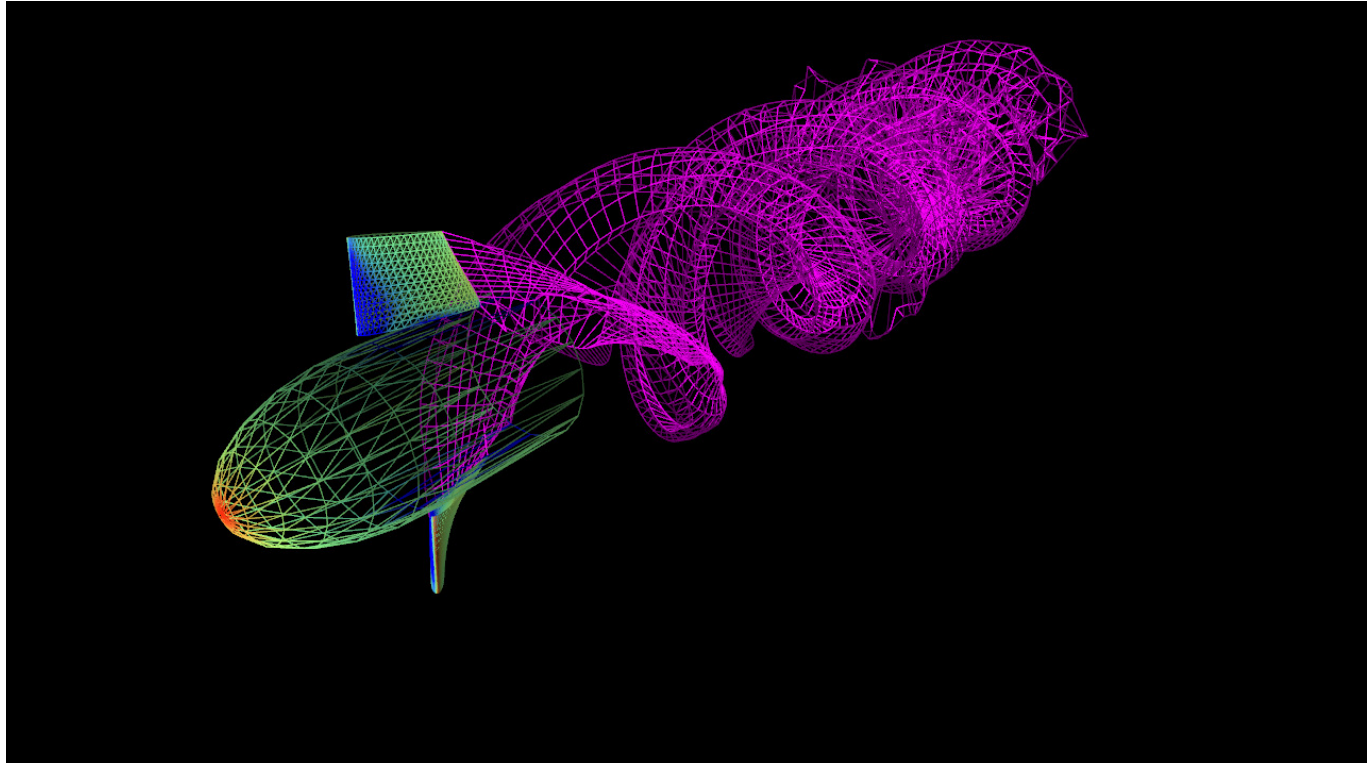


Figure 46: Second test propeller in isolation

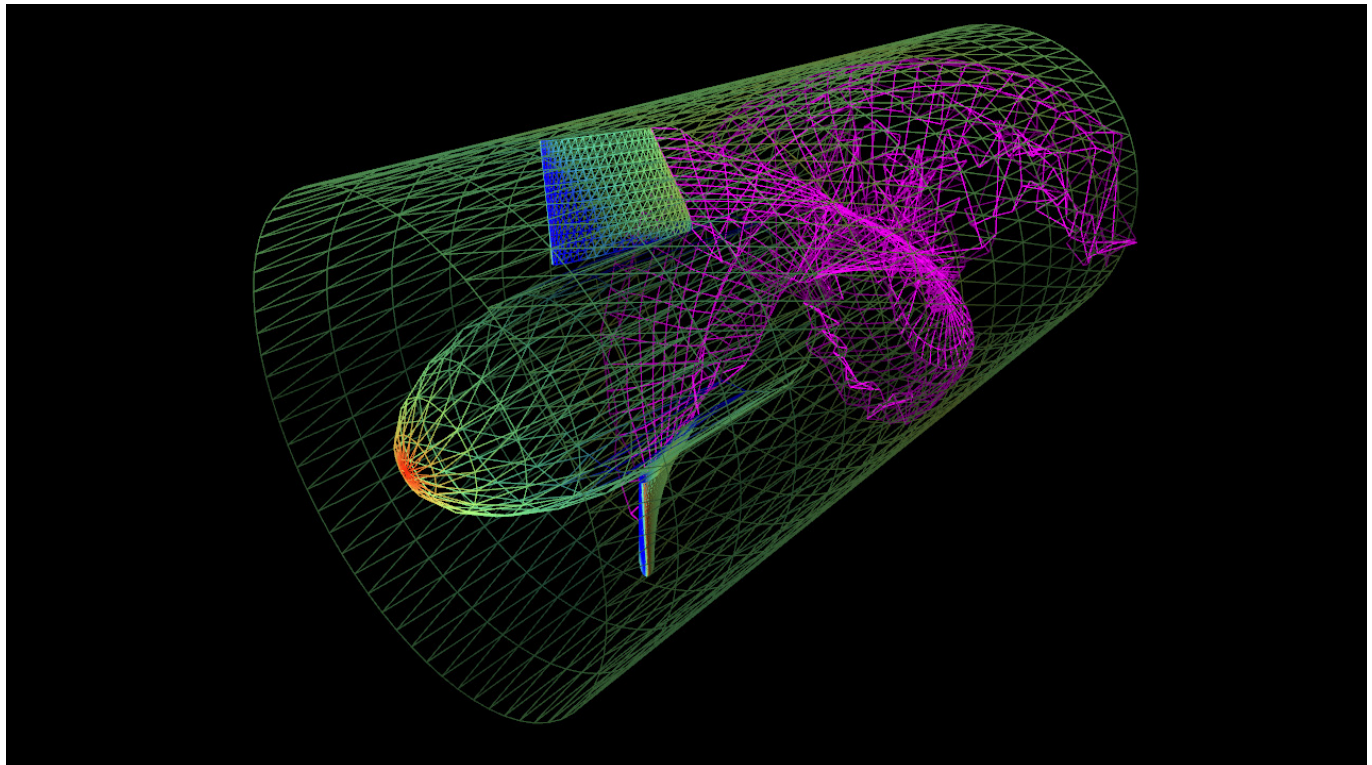


Figure 47: Second test propeller placed inside a cylindrical duct

The higher advance ratio creates a helicoidal wake sheet with larger pitch. Furthermore this test ought to highlight the tip effects even more than the previous propeller due to the very low aspect ratio of these blades. Using the mean aerodynamic chord and tip radius, the aspect ratio of the previous open propeller blade was 4.4 while the current ducted propeller blade has an aspect ratio of just 0.92. The results for the force and torque from both simulations are given below.

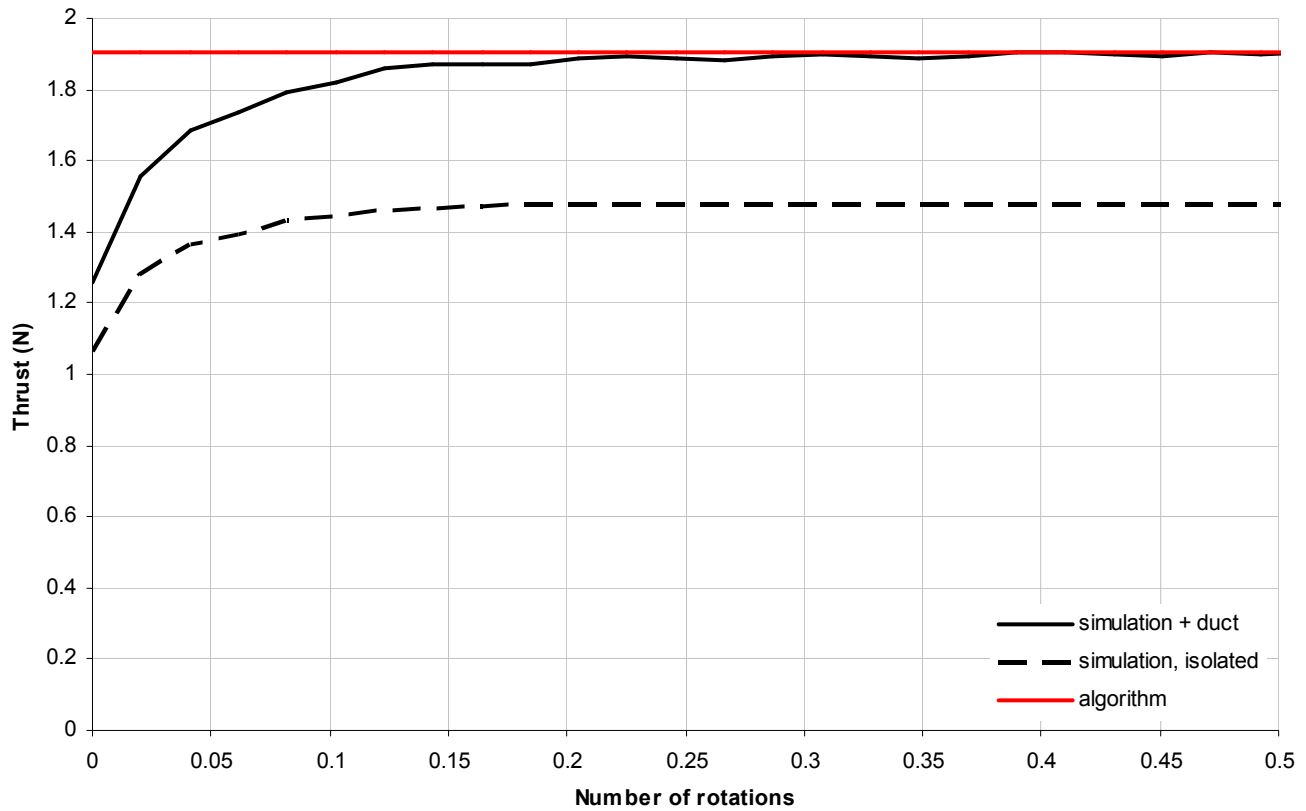


Figure 48: Comparison between thrust from design algorithm and simulation with ducted and isolated propeller

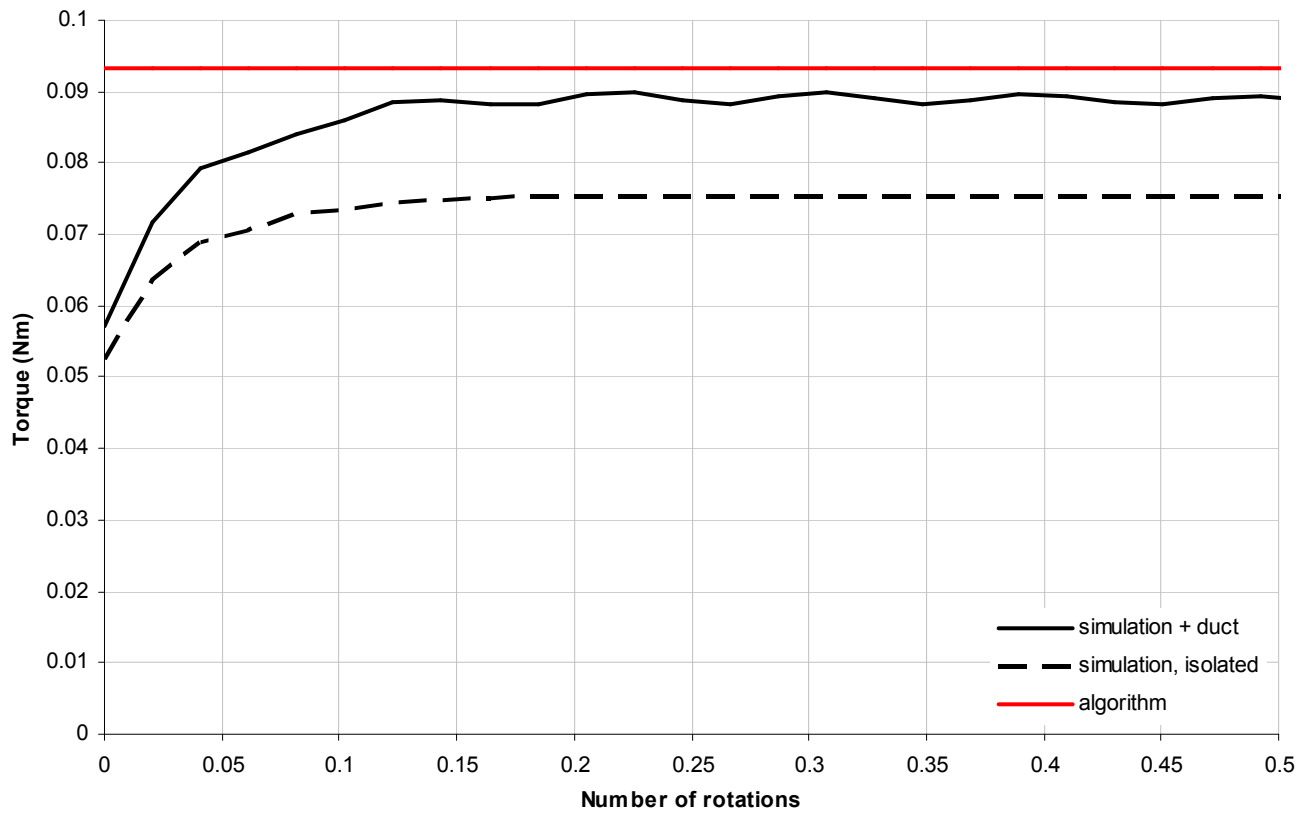


Figure 49: Comparison between shaft torque from design algorithm and simulation with ducted and isolated propeller

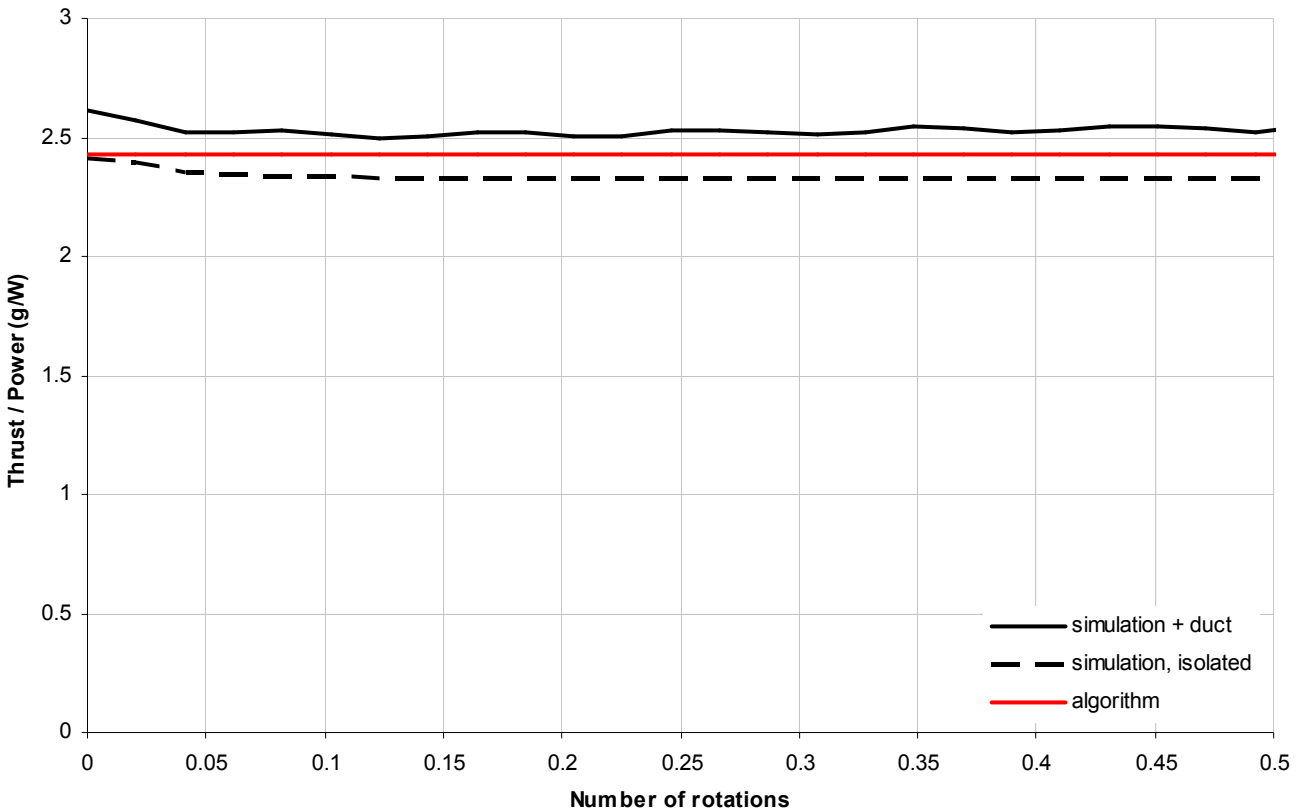


Figure 50: Comparison between thrust/power ratio from design algorithm and simulation with ducted and isolated propeller

With the cylindrical duct in place, the steady thrust almost exactly agrees with the result from the design algorithm and the torque is also much closer to the design algorithm result. The errors in the design algorithm for the isolated propeller in this case were 28.7% in thrust and 23.8% in torque. With the cylindrical duct these errors are reduced to -0.11% and 5.97% respectively. It should be noted that the excellent agreement in thrust may be somewhat coincidental considering that the duct had a 5% blade tip clearance. Some quick tests were done to assess the effect of this clearance on the thrust and it was found that a decreased tip clearance caused further increase in thrust. However with reduced tip clearance came the need for a much finer mesh for the cylinder to prevent the wake sheet from leaking out through the panels. Furthermore, the very large velocity gradients that would exist between the propeller tip and duct wall in a real system with no-slip walls would mean that viscous effects would be very significant in that region and cannot really be ignored.

One can conclude from these brief tests that a combination of blade tip effects (wake sheet edge rollup) and wake contraction are significant non-linear features that can result in errors reaching the order of 30% in thrust and 20% in shaft torque if they are neglected in the design algorithm, particularly for low aspect ratio blades. One way to get around the effects of blade tip losses in practice would be to design long propeller blades of high aspect ratio with relatively very small tip chords – rather like those seen on wind turbines. Whether this is possible depends on the stiffness of the available materials to prevent substantial blade flexing and untwisting and also on structural considerations (i.e. hub mounting point centrifugal force limitations). It is possible to pre-twist and bend the blades to allow for such flexing during operation at the design point.

This last test case shows how a 3D potential flow code such as the one developed in this report can be used to gain insight into fundamental flow physics and to draw useful conclusions during the design and testing stage of real-world geometries. Of course the user must not forget the limitations of the potential flow model, and any situation where viscous dissipative effects or turbulent flow dynamics become important will render the results inaccurate, possibly to a large extent.

Conclusion & Future Possibilities

A vortex lattice panel method code for multi-body, three-dimensional, unsteady potential flow problems was developed using the equations and solution procedures derived in this report. Validation was achieved through a series of basic test cases where analytical solutions were available as well as through self-consistency checks. Finally the practical applicability of such a code was demonstrated in the case of assessing a propeller design algorithm and ascertaining the causes of the discrepancies in thrust and torque through computer experiments.

Regarding future possibilities, the existing code could be linked with an optimisation algorithm which could then be used to aid in the design of optimum propellers as well as in discovering the optimal driver functions for a flapping wing system. Of course all investigations using this code are limited to high Reynolds number flows where the boundary layer remains attached and of negligibly small displacement thickness.

With respect to coding, the system of equations for the panel method is amenable to parallelisation. Since the influence coefficients are evaluated independently for each panel, the array of panels can be split into chunks and processed in parallel on separate CPU cores.

References

- Katz J. & Plotkin A. (2001):** Low-Speed Aerodynamics, 2nd Ed. *Cambridge University Press*
- Kuethe A. M. & Chow C-Y (1998):** Foundations of Aerodynamics – Bases of Aerodynamic Design, 5th Ed. *John Wiley & Sons Inc.*
- Nathan P. (2011):** The Linear Vortex Panel Method. A Complete Derivation Including Extension to Multi-body Problems and Unsteady Flows. *University of Surrey Fluids Research Centre internal report FRC/TG/11.03*
- Spiegel M. R. (1959):** Vector Analysis and an Introduction to Tensor Analysis. *McGraw-Hill (Schaum's Outline Series)*
- Srivastava A. (1991):** Quadrilateral Vortex Panel Code – Theory Document. *National Aeronautical Laboratory of India, Computational & Theoretical Fluid Dynamics Division, Project Document CF 9199*
- Srivastava A. (1994):** Redundancy in the Discrete-Vortex Method for Closed Bodies. *J. Aircraft, Vol. 31 No. 6: Engineering Notes*
- Struve E. (1943):** Theoretical Determination of Axial Fan Performance. *NACA TM 1042*